Final Technical Report

AFOSR·TR· ч() ()δ4()

AD-A225 098

INVESTIGATION OF THE PROPAGATION OF INTENSE CHARGED PARTICLE BEAMS INTO VACUUM

Grant No. AFOSR 84-0091

For the Period

May 1, 1987 to April 30, 1990

Submitted to

Air Force Office of Scientific Research

July, 1990

DTIC
ELECTE
JUL 3 0 1990
S E D

Submitted by

Electrical Engineering Department

and

Laboratory for Plasma Research

University of Maryland

College Park, Maryland 20742

90 0 004

REPORT DOCUMENTATION PAGE

1. AGENCY USE ONLY (Leave blank)	2. REPORT DATE July 1990	3. REPORT TYPE AND DATES COVERED Final Report/1 Apr 84-30 Apr 90

4. TITLE AND SUBTITLE

Investigation of the Propagation of Intense
Charged Particle Beams Into Vacuum

5. FUNDING NUMBERS

61102F/2301/A7

6. AUTHOR(S)

William W. Destler

7. PERFORMING ORGANIZATION NAME(S) AND ADDRESS(ES)

University of Maryland
Electrical Engineering Department and
Laboratory for Plasma Research
College Park, MD 20743

AFOSR-TR·

8. PERFORMING ORGANIZATION REPORT NUMBER

9. SPONSORING/MONITORING AGENCY NAME(S) AND ADDRESS(ES)

AFOSR/NP
Bolling AFB DC   332-6448

10. SPONSORING/MONITORING AGENCY REPORT NUMBER

AFOSR-84-0091

11. SUPPLEMENTARY NOTES

12a. DISTRIBUTION/AVAILABILITY STATEMENT

Approved for public release; distribution is unlimited.

12b. DISTRIBUTION CODE

13. ABSTRACT (Maximum 200 words)

Laser-controlled beamfront accelerator experiments achieved gradients of up to
40 MV/m and proton acceleration to 18 MeV over 40 cm with a beam energy of
900 keV. Beamfront electric field degradiation requires beam energy to be
increased as the gradient is increased. An experiment with a beam energy of
1.5 MeV achieved a 60 MV/m gradient in a 100 cm distance, matching theoretical
models. Experiments with psuedospark discharges achieved electron beams of
25 kV, 100 A/cm^2, 10 ns with 10^{11} A/(m-rad)^2 brightness. Theory
indicates densities greater than 10^3 A/cm^2 and brightness greater than
10^{11} A/(m-rad)^2 are achievable.

14. SUBJECT TERMS

charge-neutral, current-neutral charged particle beams,
plasmoids

15. NUMBER OF PAGES
129

16. PRICE CODE

17. SECURITY CLASSIFICATION OF REPORT UNCLASSIFIED	18. SECURITY CLASSIFICATION OF THIS PAGE UNCLASSIFIED	19. SECURITY CLASSIFICATION OF ABSTRACT UNCLASSIFIED	20. LIMITATION OF ABSTRACT UL SAR

TABLE OF CONTENTS

Accession For

NTIS GRA&I		X
DTIC TAB		
Unannounced		☐
Justification		

By

Distribution/

Availability Codes

Dist	Avail and/or Special
A-1	

Abstract

This is the third and final annual technical report of a three year research program to study both experimentally and theoretically the propagation of intense charged particle beams into vacuum. This program was initially funded by the Air Force Office of Scientific Research for the period April 1, 1985 to April 30, 1987 under Grant No. AFOSR-84-0091. The new three year program is a continuation of that research under the same Grant Number. The goal of this research is the generation of nearly charge-neutral, current-neutral charged particle beams (plasmoids) which are capable of propagating beam energy in vacuum at a significant fraction of the velocity of light.

1   Introduction and Synopsis

Studies of the propagation of intense charged particle beams into vacuum have been pursued at the University of Maryland under AFOSR sponsorship since 1984. The principal goal of this program has been to investigate under what conditions intense charged particle beam energy may be propagated into free space without the benefit of confining magnetic fields or conducting boundaries. Initial experimental and theoretical work has centered around the propagation of intense electron beams into vacuum after passage through an ion source localized to the injection point. In such systems propagation can occur when ions are accelerated from the source region into vacuum by the space charge fields of an electron beam injected at a current level above the space charge limit. The resultant neutralization of the electron beam by the accelerated ions can allow effective propagation in the vacuum region.

The research progress during this final year is contained in Section 2. Studies on beam propagation with no applied fields have involved our Laser Controlled Beamfront Accelerator concept. Both experimental and theoretical results are summarized. A second experimental effort on the production of high quality electron beams via a "pseudospark" device has been initiated in addition to general studies of pulsed power systems and associated diagnostics. The major achievements are as follows:

A. In the laser-controlled beamfront accelerator experiments, an ionization channel is generated by time-sequenced formation of plasma along the drift tube wall that contributes to effective beam propagation into vacuum. This is accomplished by sequential, time-delayed interaction of laser beams with targets on the drift-tube wall. The intense electron beam injected into this system will propagate with a beamfront velocity $v_f(t)$ that is determined by the timing of the ionization channel in the drift tube. Ions are pulled in from the plasma near the wall to essentially space charge neutralize the electron beam. Some ions trapped in the space-charge well, also known as the "virtual cathode," of the electron beamfront, will be accelerated to a velocity $v_f(t)$. These trapped ions are collectively accelerated to high energies and aid in the formation of a charge and current neutralized beam system for propagation into free space. The key requirement is that the ions remain trapped in the well or, alternately, that the

1

laser-controlled beamfront velocity is synchronized with the changing accelerating gradient associated with the well. Our first experiment with a 900 keV, 20 kA, 30 ns electron beam was based on a gradient of 40 MV/m and achieved successful proton acceleration to about 18 MeV in a distance of 40 cm. Attempts to increase this energy by increasing the laser-controlled beamfront velocity, consistent with an accelerating gradient of 90 MV/m, were unsuccessful. This result is explained by numerical studies that showed the degradation of the beamfront electric field. Higher ion energies can only be achieved by increasing the electron beam energy, say from 900 keV to about 1.5 MeV. A second-generation experiment based on these theoretical results has been designed and built. It uses a gradient of 60 MV/m and a distance of 100 cm. Control of the beamfront over the 100 cm distance has proved successful, achieving a 0.3 c beamfront velocity.

B. Theoretical research has been concerned with four problems: the initial phase of ion production and acceleration, the simulation of our laser controlled beamfront acceleration experiment, the propagation of a partially neutralized electron beam across a transverse magnetic field, and the ion hose instability of a partially neutralized beam with Bennett profile. Each of these four activities produced excellent results that have been, or will be, published. Particularly noteworthy is the good agreement with the laser controlled beamfront acceleration experiments, as already mentioned in A above. The successful modeling of the rather complicated physics including the ionization by the electron beam is very helpful not only in the design of new experiments, but also in the overall evaluation of this type of accelerator.

C. During this contract year we started a new experiment called the "pseudospark discharge." A novel device, invented in Germany, the pseudospark has many interesting applications such as pulsed-power switching and electron beam generation. We are particularly interested in the latter application. Our first experiments have demonstrated that the pseudospark discharge with suitable electrode configuration produces an electron beam of extremely high quality. Measurements showed a beam of 25 kV, 100 A, 10 ns with a normalized brightness of 10^{11} A/(m-rad)^2. This is considerably bet-

2

ter than the quality of beams from thermionic cathodes and makes the pseudospark source very attractive for advanced accelerator applications (linear colliders, FELs, etc.). The physics of the pseudospark device is not yet well understood, and we believe that we can make an important contribution in this area. From preliminary scaling considerations, we expect even higher current densities [$> 10^3$ A/cm^2] and brightness values [$> 10^{11}$ A/(m-rad)^2] at increased voltages.

A complete list of papers and presentations that have resulted from our research during the past several years is given in Appendix A, with copies of more recent publications included in Appendix B.

2 Research Progress

2.1 Experimental Research

2.1.1 Experiments on the DRAGON Pulse Line Accelerator

A systematic experimental measurement of currents in a low pressure, gas filled drift tube, into which a high-current electron beam is injected, was carried out. In order to produce high-current electron beams of good reproducibility, we developed a new diode system in which an anode with a specially designed foil changer is employed. A paper detailing this diode with foil changer is published in the *Rev. Sci. Instrum.* 60, 3556 (1989), and enclosed in Appendix B. We observed that as gas pressure in the drift chamber is increased, the magnitude of the net current increases up to a peak value, and then decreases. The pressure at which this peak value is achieved was interpreted as the critical pressure required for full charge neutralization of the beam. Above this critical gas pressure, the waveform of the current decays nearly exponentially with a slow decay time constant. The decay time constant was attributed to L/R of the drift tube and plasma column, and the resistivity of the plasma can be inferred from the time constant. A paper detailing this study is published in the Proc. 1989 IEEE Particle Accelerator Conference, p. 1052 (1989).

2.1.2 Laser Controlled Beamfront Experiments

The basic concept behind the Laser Controlled Beamfront Experiment is shown in Fig. 1. An intense relativistic electron beam is injected into an evacuated drift tube at a current level several times the vacuum space charge limit, given approximately by

$$I_\ell = \frac{17,000(\gamma_o^{2/3} - 1)^{3/2}}{(1 + 2\ell nb/a)(1 - f)} \tag{1}$$

where b is the drift tube radius, a is the beam radius, γ_o is the relativistic mass ratio for the electrons at injection, and $f = n_i/n_e$ represents any charge neutralization provided by positive ions. As indicated in Fig. 1a, a virtual cathode forms at the injection point with a depth approximately equal to the anode-cathode potential difference. The axial position of the virtual cathode downstream of the anode plane is usually on the order of the anode

4

cathode gap, so that megavolt potentials at the virtual cathode are formed only millimeters away from the grounded anode. It is this very high electric field on the upstream side of the virtual cathode that collective accelerators usually seek to exploit for ion trapping and acceleration.

If the beam is injected into a localized gas cloud (Fig. 1b), ionization processes can quickly build up sufficient ion density to neutralize the electron beam space charge and the virtual cathode can move downstream to the edge of the gas cloud. This motion can result in the acceleration of a few ions to energies considerably higher than the depth of the potential well at the virtual cathode.

In order to control the motion of the virtual cathode over distances greater than a few centimeters, however, a means of providing an ionization channel whose axial extent can be controlled as a function of time is required (Fig. 1c). In the present experiments, shown schematically in Fig. 2, the ionization channel is generated by time-sequenced laser-target interactions. A laser pulse is separated into many approximately equal energy beams which are then optically delayed over different path lengths. The laser light then vaporizes and ionizes a target material on the drift tube wall, and ions drawn into the beam by the electron space charge at the beamfront provide the required time-sequenced channel of ionization to control beamfront motion.

During the last year, a complete 1 meter Laser Controlled Beamfront Experiment has been designed, constructed, and tested (see Figs. 2 and 3). This new experiment is a significant upgrade of the previous 50 cm experiment, in which controlled beamfront motion was first demonstrated. Injected electron beam characteristics were 1 MeV, 27 kA, 30 ns. Tests of the optical system, detailed in Table 1, indicate that optical system losses can be kept to acceptable levels even in a 40 mirror system if sufficient care in system alignment is taken.

In order to measure the propagation of the beamfront down the drift tube, a series of current collection probes were installed in the wall of the drift tube. As the beamfront approaches these probes, the current measured should rise gradually until the beamfront passes by the probe location, at which beam current at the wall should fall rapidly (see Fig. 1c). Sample oscilloscope waveforms from the current collecting probes at the drift tube wall are shown in Fig. 4, and show these expected characteristics clearly.
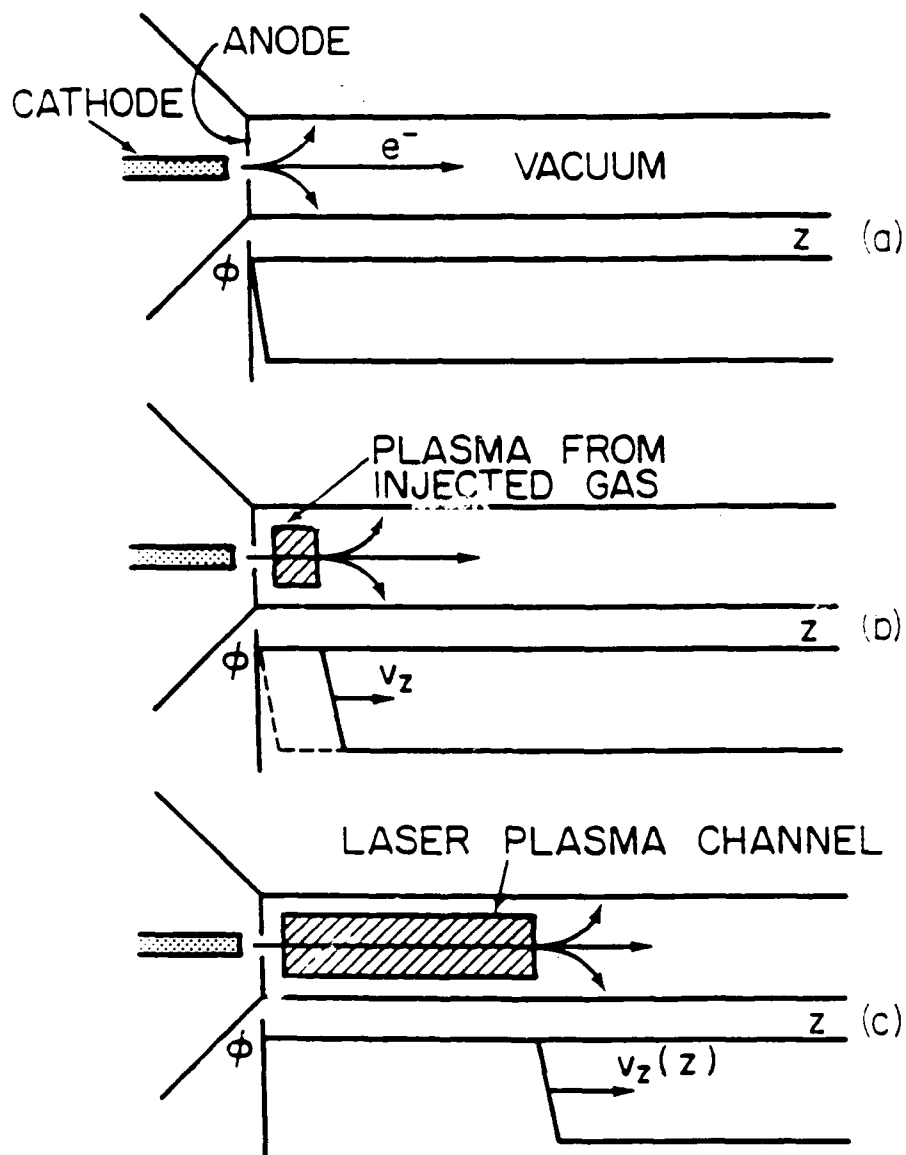
5

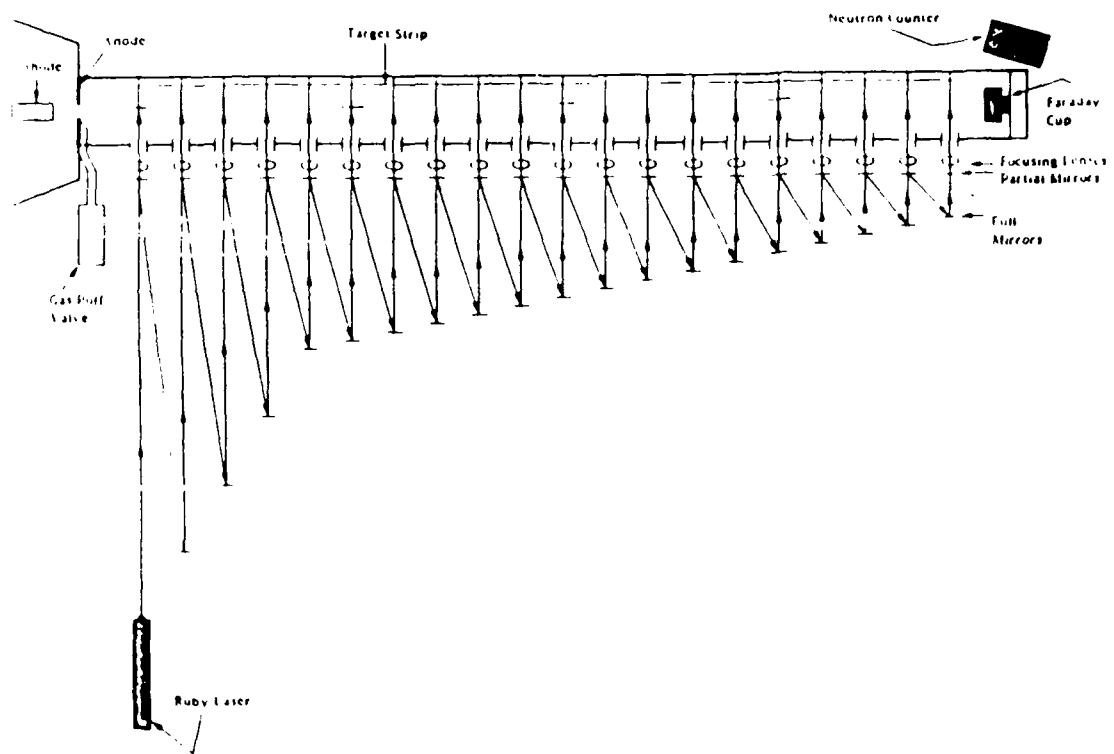Figure 1: Conceptual view of the laser controlled beamfront accelerator.

6

Figure 2: Experimental configuration for the beamfront propagation study on the laser-controlled collective ion accelerator.
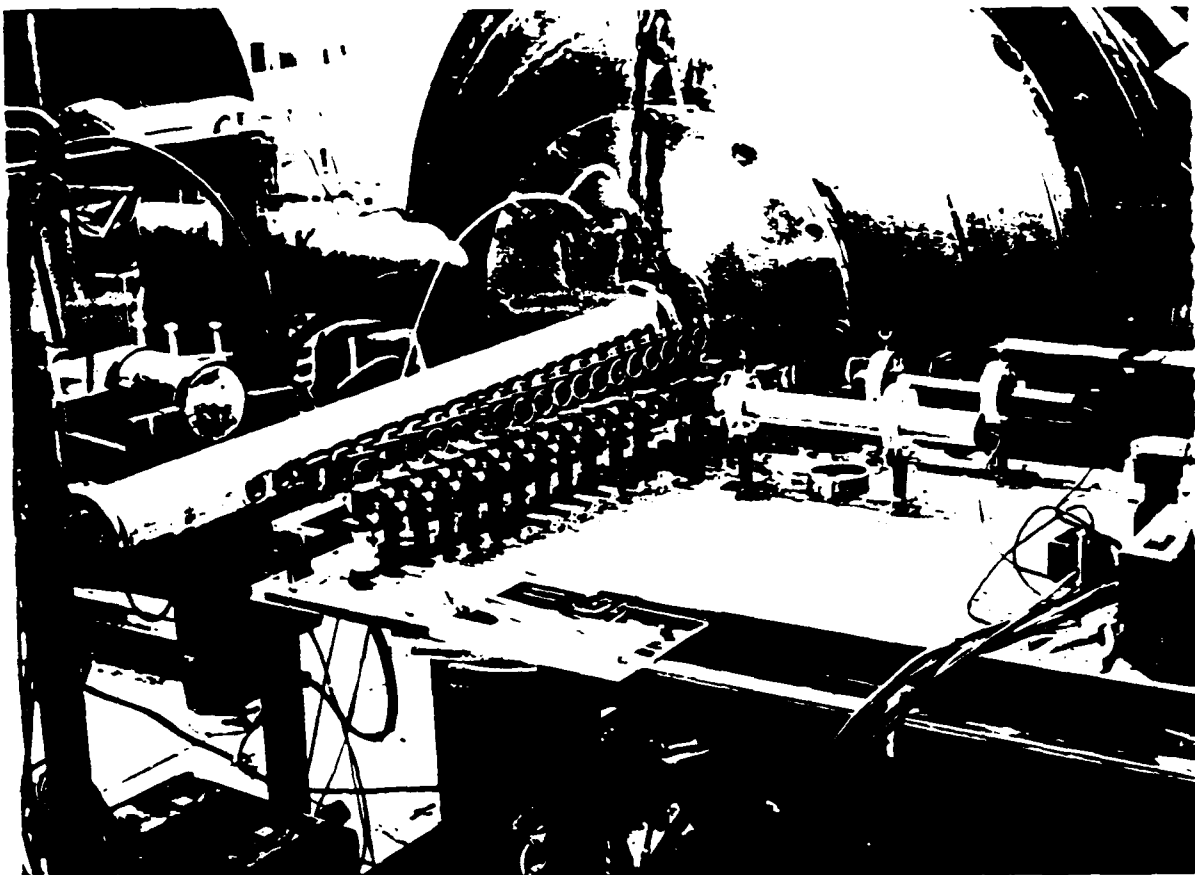
Figure 3: Photograph of the laser-controlled collective ion accelerator with the 100 cm drift tube.

Table 1: Summary of optical system tests

Channel	Axial Position (cm)	Partial Mirror Reflectivity	Theoretical Laser Energy (Joules)	Experimental Laser Energy (Joules)
1	5	0.95	0.300	0.30
2	10	0.95	0.285	0.28
3	15	0.95	0.270	0.265
4	20	0.95	0.257	0.25
5	25	0.95	0.244	0.23
6	30	0.925	0.348	0.315
7	35	0.925	0.322	0.292
8	40	0.925	0.298	0.275
9	45	0.925	0.276	0.255
10	50	0.90	0.339	0.30
11	55	0.90	0.306	0.25
12	60	0.89	0.303	0.24
13	65	0.88	0.294	0.24
14	70	0.86	0.301	0.23
15	75	0.83	0.315	0.225
16	80	0.80	0.307	0.22
17	85	0.75	0.307	0.21
18	90	0.67	0.304	0.195
19	95	0.50	0.309	0.20
20	100	—	0.309	0.19

Probe #1: 11.5 cm
2 volts/div
10 ns/div

Probe #2: 36.5 cm
1 volt/div
10 ns/div

Probe #3: 61.5 cm
500 mV/div
10 ns/div

Probe #4: 86.5 cm
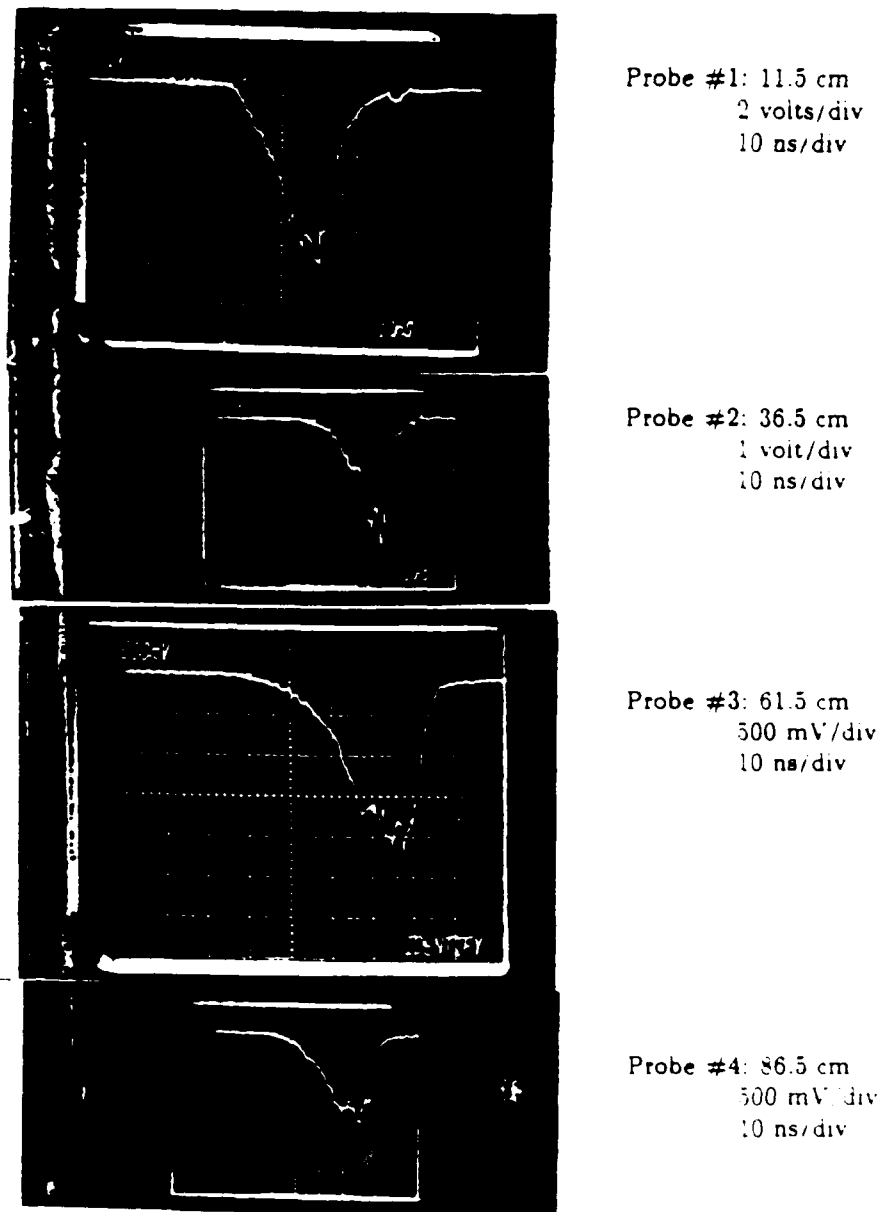500 mV/div
10 ns/div

Figure 4: Typical traces of the charge/current probe used to measure the beamfront propagation.

10

A series of studies were made of the beamfront propagation velocity down the drift tube for various delays between the firing of the laser and the injection of the electron beam. Studies were made for two acceleration gradients. Data for the first gradient, a two part gradient designed to take the beamfront velocity smoothly from 0.05c to about 0.3c in a distance of 100 cm, are shown in Figs. 5–7. Good agreement is seen between the beamfront velocity and that associated with the laser timing only, as expected, when the laser is fired just before the beam is injected. If the laser is fired much earlier, the drift tube becomes filled with plasma and the beam propagates unencumbered by space charge effects. Data for a second gradient, a slower gradient with a final velocity of only about 0.2c is shown in Figs. 8–10.

2.1.3   Pseudospark Discharge Experiment

We have continued a new experimental program, Pseudospark discharge. Although, the pseudospark discharge has interesting switching characteristics which are being studied by other laboratories, our current interest is centered around the study of electron beams. A simple discharge chamber of modular type was constructed to investigate this new electron beam source. The chamber was operated at low voltage $\sim$ 25 kV, producing $\sim$10 Hz, electron-beam pulses of $\sim$100 A, $\sim$10 ns. The rms emittance of the beam was measured and found to be $\sim$50 mm-mrad, which corresponds to the normalized brightness of the beam of $\sim 10^{11}$ A/(m^{2}rad^2). Papers detailing this study are published in Proc. 1989 IEEE Particle Accelerator Conference, p. 316, and AIP Conference Proceedings 195, Dense Z-Pinches, p. 418 (1989), *Appl. Phys. Lett.* 56, 1746 (1990), and to appear in *Phys. Fluids B* 2, (10) (1990) and Proc. of Beams '90; copies are enclosed in Appendix B.

2.2   Theoretical Research on Beam Propagation Systems

We will discuss the progress made during the past year in four separate but related topics that were under investigation. The four topics are: "Initial Ion Production and Acceleration Phase," "Laser Controlled Beamfront Accelerator," "Intense Beam Propagation Across a Magnetic Field," and "Ion Hose Instability of the Bennett Profile Beam."

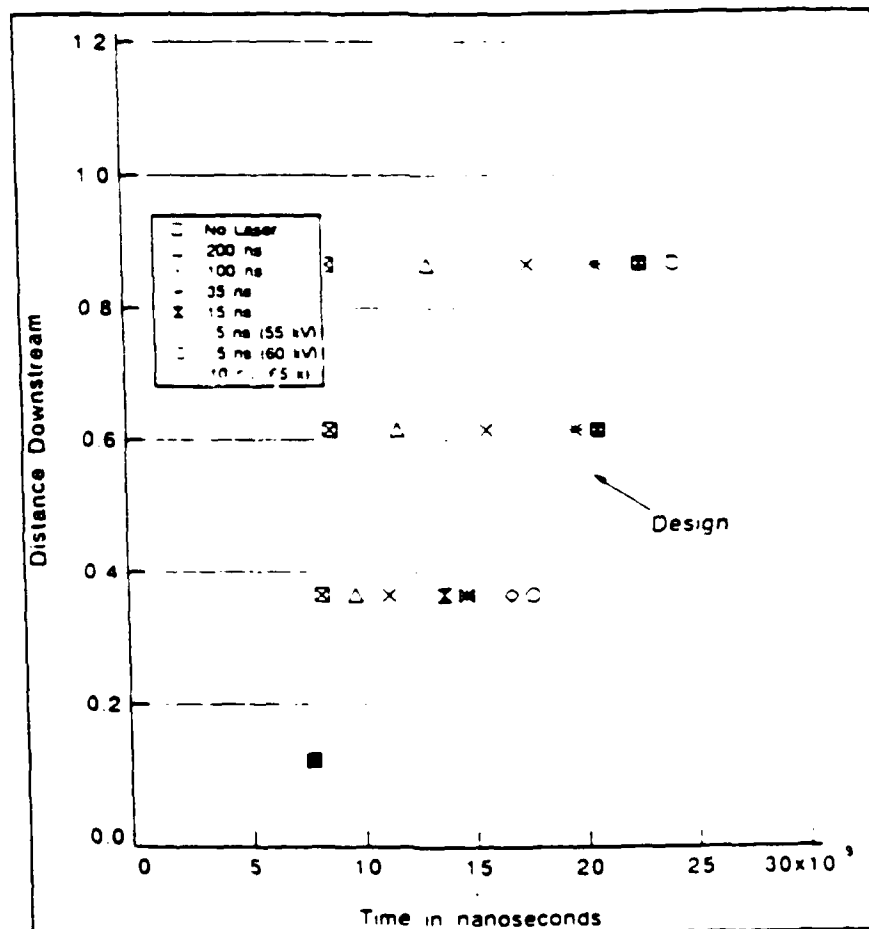Figure 5: Wall probe measurements of beamfront propagation versus time for different laser firing delay times and without the laser ("two-part" gradient).

Figure 6: Voltage observed at the wall probes for the different delay times ("two-part" gradient).

Figure 7: Average velocity versus distance downstream for different laser firing delay times and without the laser ("two-part" gradient).

14

Figure 8: Wall probe measurements of beamfront propagation versus time for different laser firing delay times and without the laser ("slower" gradient).
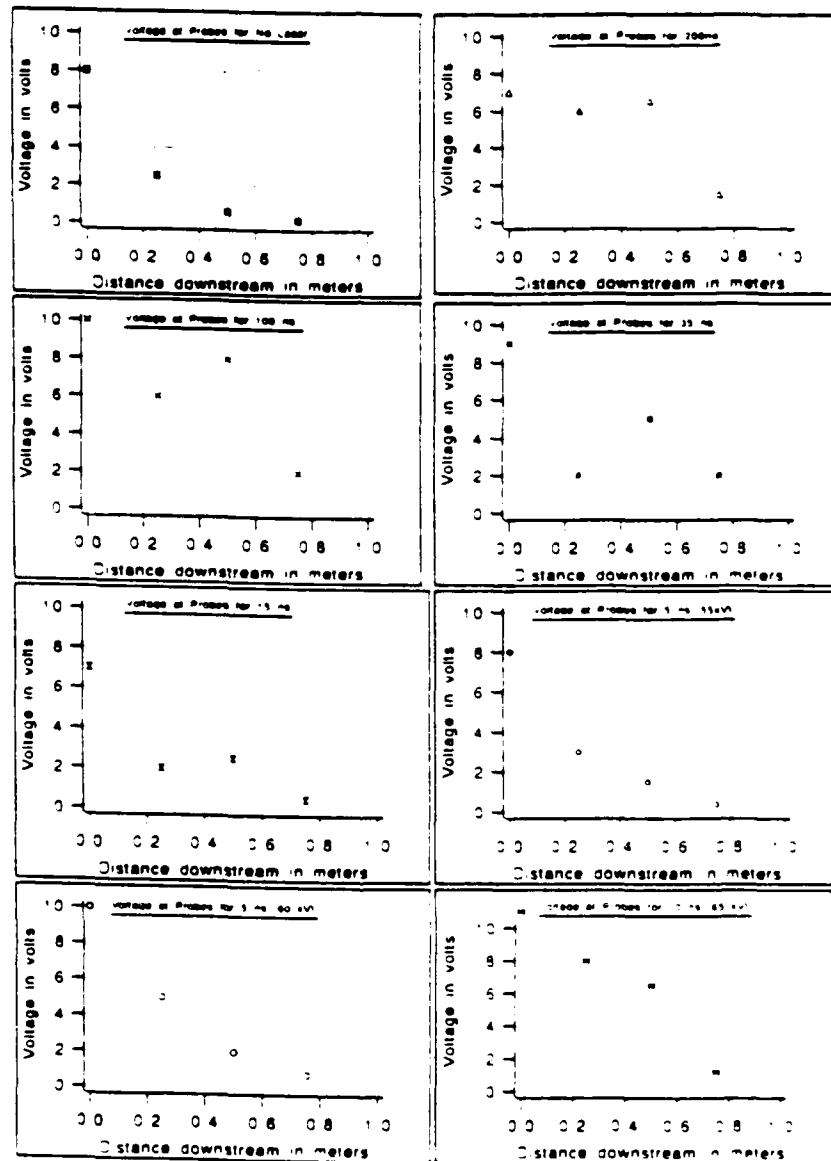
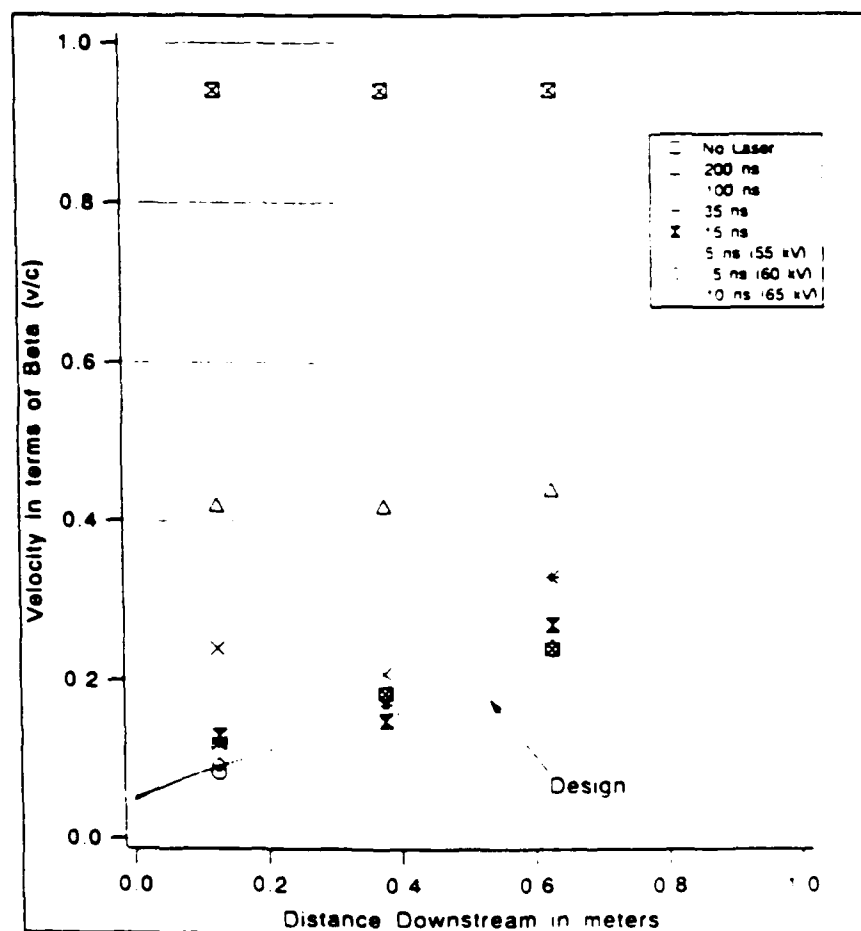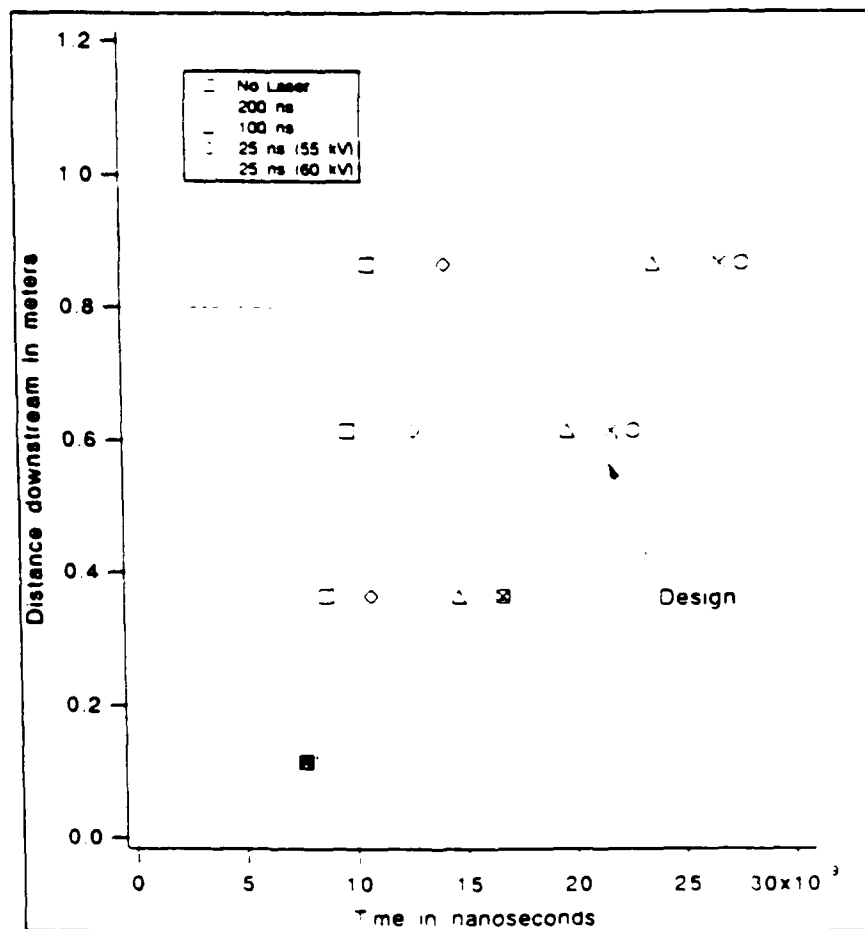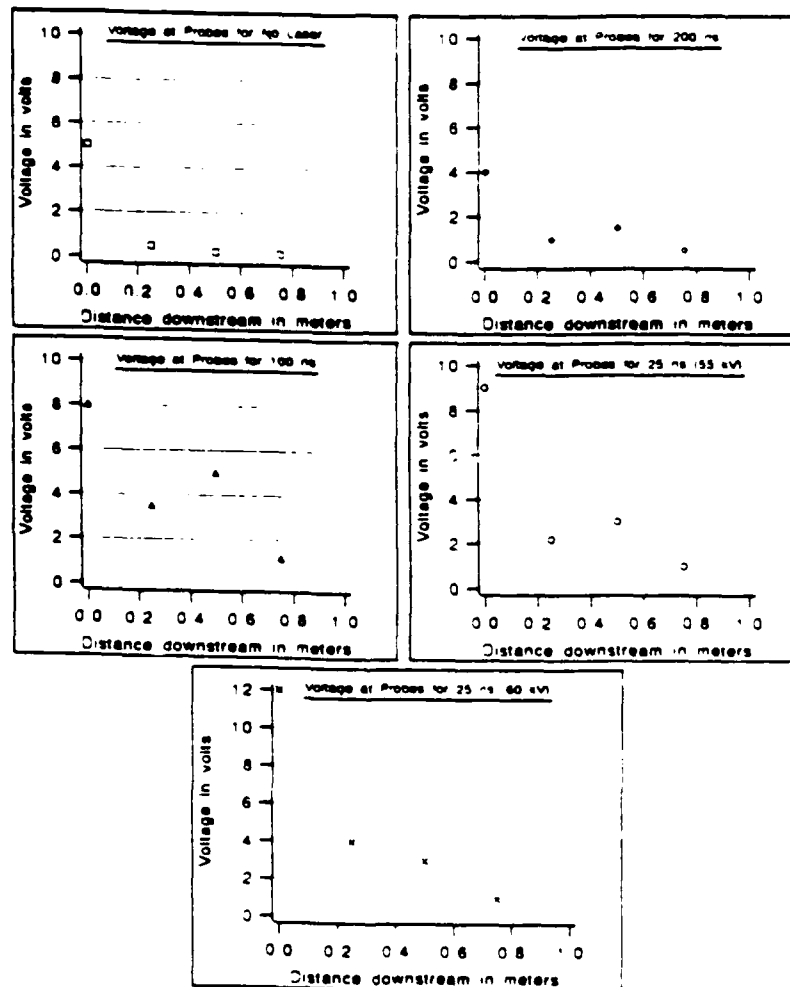Figure 9: Voltage observed at the wall probes for the different delay times ("slower" gradient).
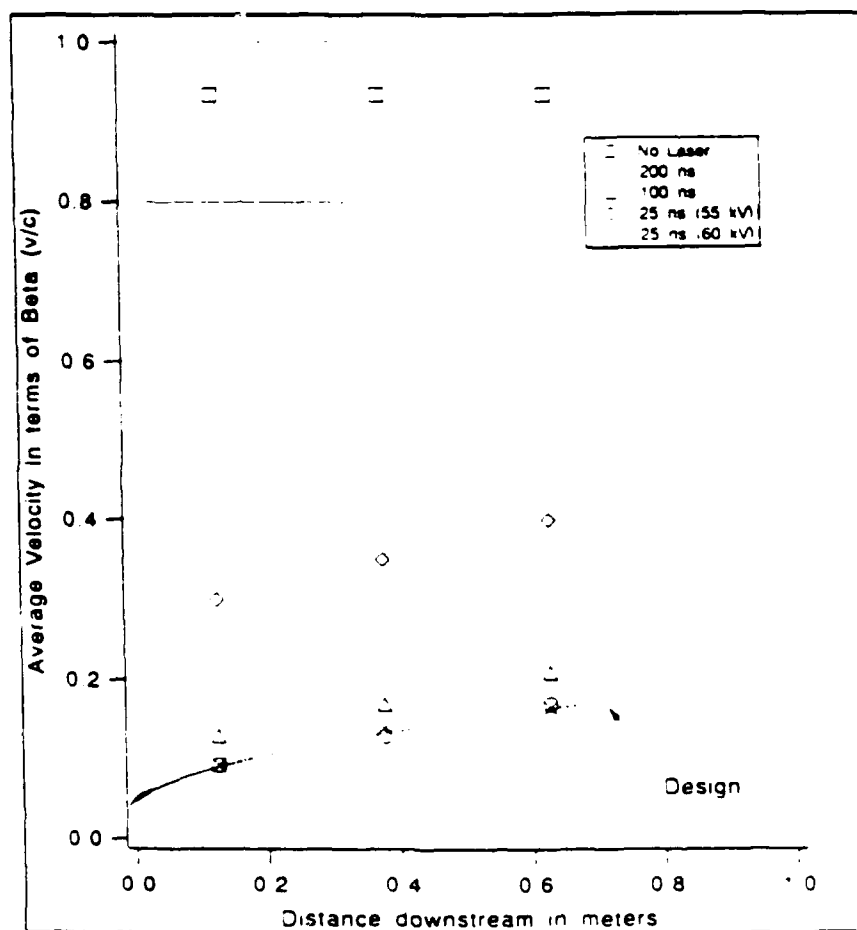
Figure 10: Average velocity versus distance downstream for different laser firing delay times and without the laser ("slower" gradient).

17

2.2.1 Initial Ion Production and Acceleration Phase

During the past year, we have completed numerical studies related to the initial phase of the ion production and acceleration process in a localized gas cloud system. These results are published in the *Journal of Applied Physics*, February 1990 issue and a copy is included in Appendix B.

In experiments in which an intense relativistic electron beam is injected into an evacuated drift tube with a localized gas cloud located near the anode, that serves as the source of ions for effective beam propagation, a large fraction of the injected electron current is observed downstream. These experiments have been simulated using a particle-in-cell code which realistically models ionization of the gas. It was found that when the injected electron beam current exceeds the space-charge limiting current, the majority of the ions produced achieve energies of the order of the beam energy and provide for an effective channel to space charge neutralize the electron beam. There are a few ions that are accelerated to energies several times the electron beam energy by the coherent motion of the ions and the intense virtual cathode electric fields. The majority of the ions allow for the total beam current to propagate to the downstream surface once the ion channel has also propagated to this location. The dependence of the peak ion energy on the system parameters as observed in the simulations was also examined. For the parameter regimes investigated with beam energies up to 3 MV, beam currents up to 35 kA, gas pressures up to 600 mTorr, and gas cloud widths up to 6 cm, peak ion energies of 5-6 times the electron beam energy have been observed in the numerous simulations.

2.2.2 Laser Controlled Beamfront Accelerator–Simulation

We have written an electrostatic particle-in-cell code called LCA to simulate the laser-controlled acceleration experiments. A copy of the paper describing this code is included in Appendix B. In the simulations, an electron beam of voltage V_0, current I_0, and radius R_b is injected into a grounded cylindrical drift tube of length d and radius R_w along the axis of the drift tube. The region of the drift tube extending from the anode to a distance z_0 downstream is filled by hydrogen gas at a constant pressure p_0 [see Fig. 11]. The electron beam is assumed to be focussed by an infinitely strong guide magnetic field, so that particles
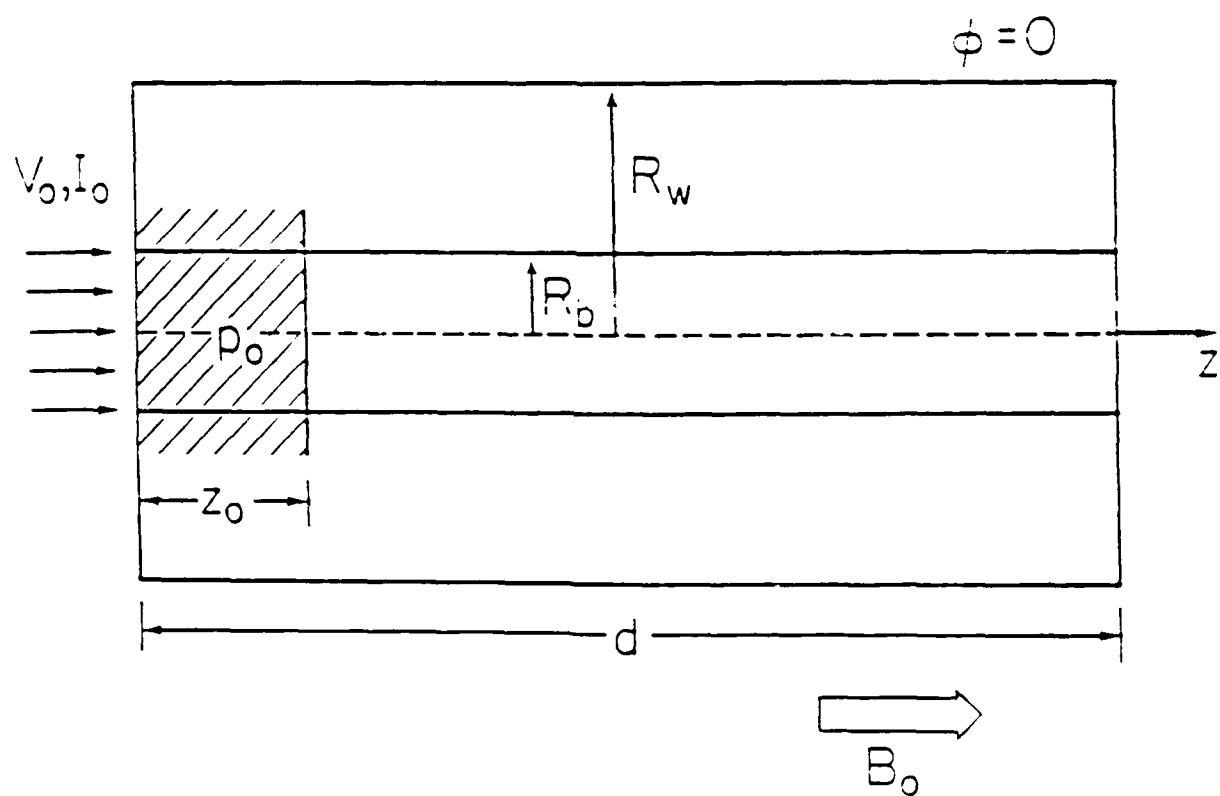
18

Figure 11: Simulation model.

in the simulation move only along the axis of the drift tube. The beam radius is also assumed to be much smaller than the wall radius so that the charge and current density and the axial electric field are approximately uniform across the beam cross-section.

The macroparticles in the simulation obey the relativistic equations of motion. the electric field E_z on axis is computed by first computing the potential ϕ at equally spaced grid points on the axis, numerically computing the derivative at points lying halfway between successive grid points, and linearly interpolating to obtain the value of E_z at other points. Ionization of the neutral gas is modeled by dividing the gas region into grid cells and monitoring the amount of ionization in each grid cell which is produced by impact ionization. When the total number of ions produced in a grid cell exceeds the number of ions in an ion macroparticle, an ion macroparticle and an electron macroparticle are created at the center of the grid. The actual details have been explained elsewhere.

The time required for the laser beam to create plasma after striking the target and the time required for the plasma once it is created to travel from the wall to the center of the drift tube are assumed to be constant quantities which are left unspecified. The front of the laser-produced plasma is assumed to sweep smoothly from one end of the drift tube to the other and the only effect of the plasma in the simulation is to completely neutralize any space-charge in the drift tube behind the plasma front.

The first set of results was obtained for a 900 keV, 20 kA, 1 cm-radius electron beam which is injected into a 5 cm-radius, 50 cm-long drift tube with a 2 cm-wide. 100 mTorr cloud of hydrogen gas located next to the injection plane. The front of the laser-produced plasma is assumed to travel down the drift tube at a velocity which increases linearly from 0.04c to 0.2c over a distance of 45 cm. These parameters are the same as those in the experiment described above. Figure 12 shows the peak proton energy measured 45 cm downstream from the injection plane as a function of the time delay between the start of the beam pulse and the start of the laser pulse. For these runs it was assumed that the laser-produced plasma was created 10 ns after the laser beam struck the target and that the time required for the plasma to travel from the wall to the center of the drift tube was equal to the time required for a proton to travel from the wall to the surface of the electron beam. assuming that the potential depression produced by the beam was equal to the beam energy V_0. The figure
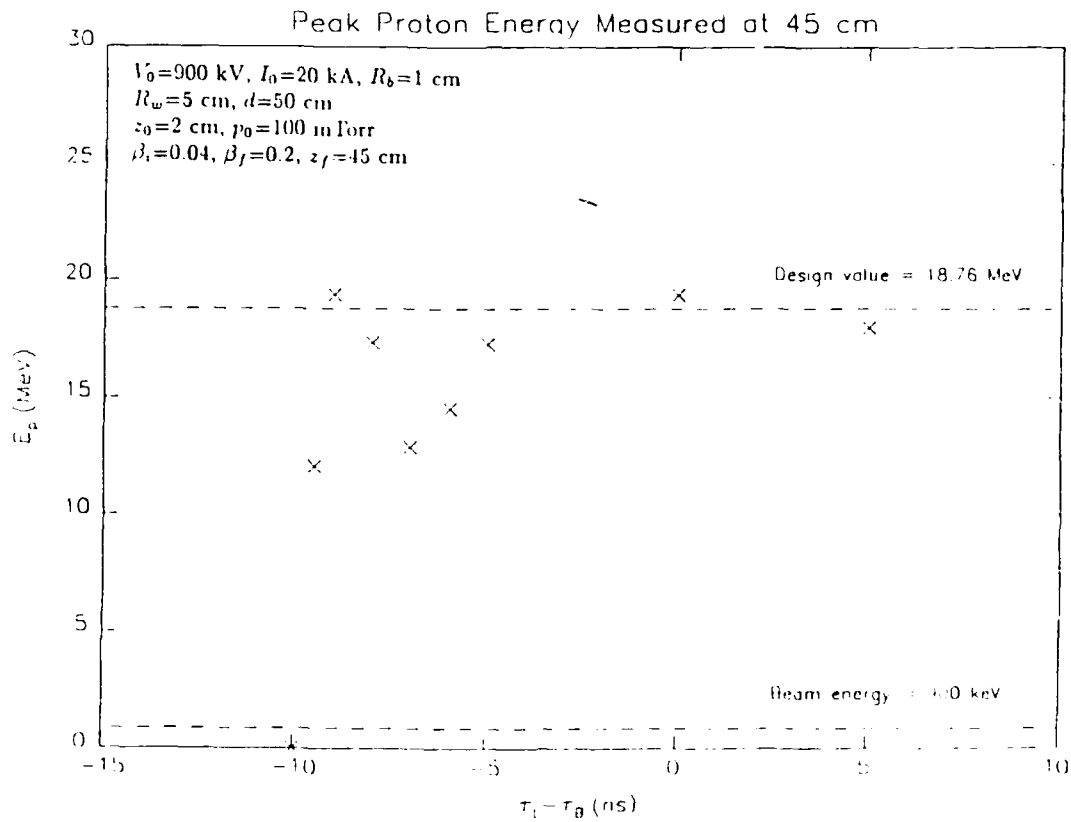
Figure 12: Peak proton energy measured at 45 cm versus time delay between start of laser pulse and start of beam pulse for linear velocity gradient.

shows that the design energy of 18.8 MeV is attained over a broad range of time delays. If one compares the phase-space trajectory of the peak-energy proton macroparticle and the phase-space trajectory of the laser-produced plasma front, we find for this design that the accelerated proton tracks the laser beam trajectory closely.

When the length of the drift tube is doubled from 50 cm to 100 cm (with all other system parameters the same) and the same velocity gradient is used, the peak proton energy measured at the end of the drift tube falls short of the design value, i.e.. the original velocity gradient cannot be extended to longer distances. The reason the original velocity gradient cannot be scaled to longer distances can be seen as follows. The equation of motion of a proton which is being accelerated by an electric field E_z is $dv/dt = (e/m)E_z$, which can be rewritten as $E_z = (mc^2/e)v dv/dz$. If the velocity gradient dv/dz used in the above runs is substituted into the preceding expression, we find that the electric field needed to accelerate the proton at the desired velocity gradient is approximately $E_z = 334\beta$ MV/m, where $\beta = v/c$, e.g., for $\beta = 0.3$, an electric field of more than 100 MV/m is needed. In Fig. 13, we have plotted the magnitude versus the location of the peak electric field for the run with a 100 cm-long drift tube in which the greatest peak proton energy was measured. Notice that as the beam front moves downstream, the peak electric field tends to fall until it is no longer large enough to continue accelerating the proton at a constant velocity gradient.

The tendency of the peak electric field to fall as the beam front moves downstream suggests that it may be better to accelerate the protons with a steep velocity gradient at the start and then taper the gradient as the beam front moves downstream. In the second series of runs, we therefore chose to do a set of runs in which the beam front velocity increases linearly with distance (i.e., dv/dz = constant) until it reaches a transition point, after which the beam front velocity increases linearly with time (i.e., dv/dt = constant).

The plasma front velocity at the anode plane was chosen to be 0.04c, the plasma front velocity at the downstream end of the drift tube was chosen to be 0.4c, and the velocity $\beta_t c$ at the transition point z_t was varied. Figure 14 shows the peak proton energy measured at 90 cm as a function of β_t for three different values of z_t. Note that $V_0 = 1.5$ MV in this run. The figure shows that by adjusting β_t, energies in excess of the design energy of 60.7 MeV can be achieved.

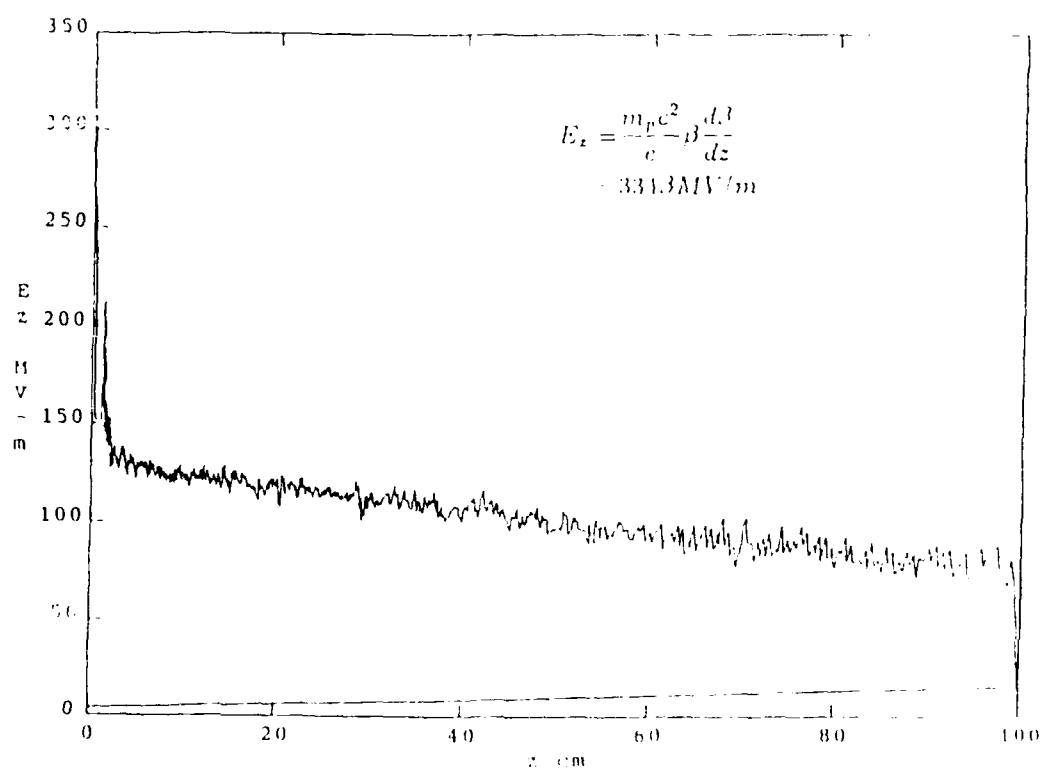$$E_z = \frac{m_p c^2}{e} \beta \frac{d\beta}{dz}$$

$$\approx 331.3 MV/m$$

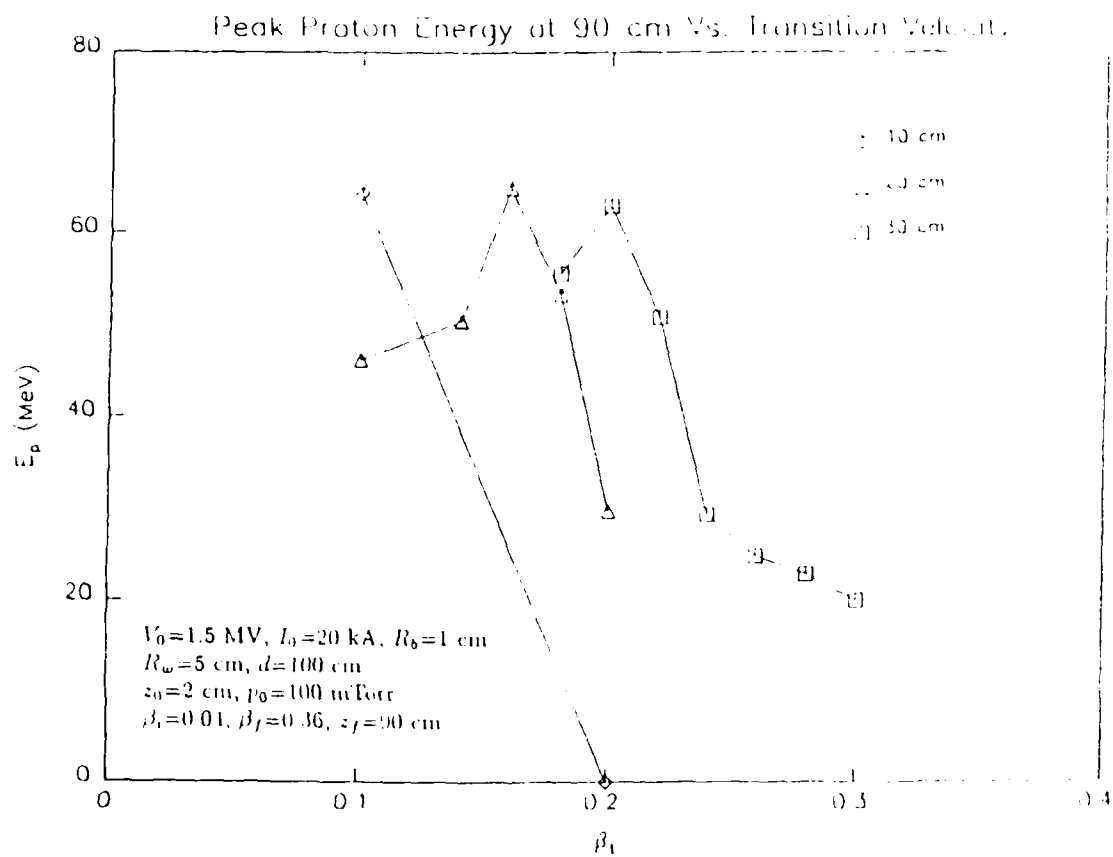Figure 13: Magnitude versus location of peak electric field.

Figure 14: Peak proton energy measured at 90 cm versus transition velocity β.

It should be noted that, as might be expected, the peak proton energy depends strongly on the beam energy, since the peak electric field increases with increasing beam energy. In Fig. 15, we plot the peak proton energy measured at the downstream end of a 50 cm-long drift tube as a function of the electron beam energy. In each case the same velocity profile is used. For beam energies greater than 1.4 MeV, peak proton energies exceed the design value. As the beam energy decreases, the peak proton energy decreases sharply, e.g., at 1 MeV, the peak proton energy is already less than 20 MeV.

Optimal Acceleration–New Design. The largest proton energies achievable in any given system can be calculated by integrating the peak electric fields obtained from the simulations as a function of distance (assuming that the magnitude of the peak electric field depends only on the position of the plasma beam front and not on its velocity). The required variation of the plasma front position with time can be obtained by integrating the equations $vdv/dz = eE_{z,max}(z)$ and $dz/dt = v(z)$, where $E_{z,max}(z)$ is the peak electric field at z. Figure 16 shows β vs. z and t vs. z for a 1.2 MeV, 20 kA electron beam which is injected into a 50 cm-long drift tube.

We have developed the electrostatic PIC code LCA to simulate beam propagation and collective ion acceleration in a laser-controlled accelerator. Although the code only crudely models the experiment, it has been able to reproduce some of the experimental results and may be useful as a design tool for future laser-controlled acceleration experiments.

2.2.3 Intense Beam Propagation Across a Magnetic Field

We completed the studies on an initial model of the propagation of an intense electron-ion beam across a transverse magnetic field. The results are published in the 1989 Particle Accelerator Conference Proceedings, and a copy of the work is included in Appendix B.

Previous theoretical studies have shown the existence of a self-consistent downstream Bennett equilibrium for the electrons and ions when no applied magnetic field is present [C.D. Striffler, R.L. Yao, X. Zhang, Proc. of the 1987 IEEE PAC, page 975]. We have related these downstream properties to the diode voltage, the transmitted electron beam current, and the ion properties in the localized gas cloud region. For our experimental parameters,
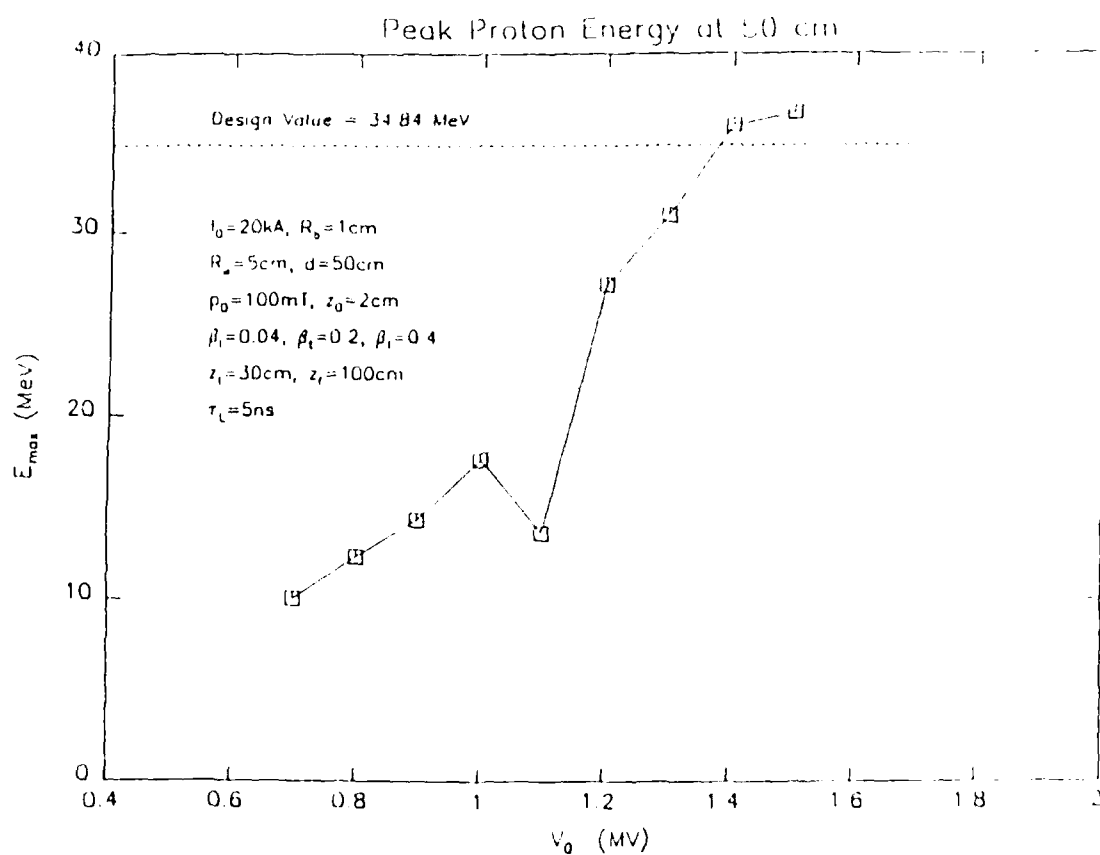
25

Figure 15: Peak proton energy measured at 50 cm versus electron beam energy.
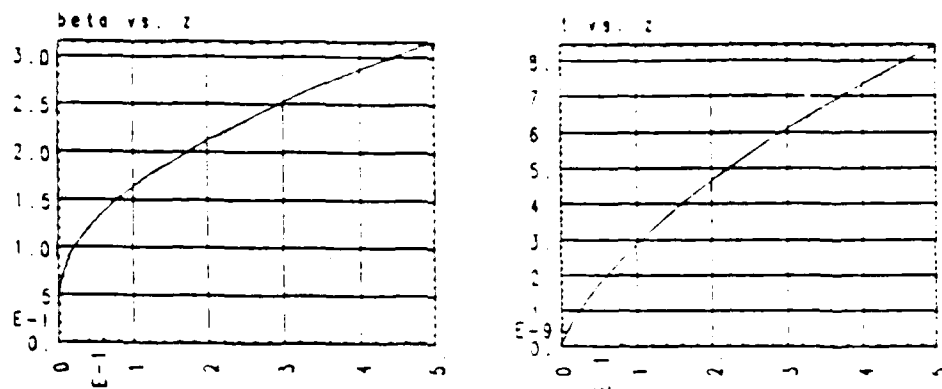
Figure 16: Optimal acceleration profile.

$V_0 = 1$ MV, $I = 5$ kA, the downstream self-pinched equilibrium state is composed of cold ions with low axial speed (< 0.05 c), and electrons with a temperature of about 60 keV and an axial speed of about 0.84 c. The nearly charge-neutral beam system has been shown to effectively propagate up to the diode current of 20 kA where the electron temperature is predicted to be about 200 keV. The 5 kA case was chosen for examining the effects of a transverse magnetic field on the electron-ion beam system, mainly because of experimental reproducibility. We considered the propagation of this intense electron-ion beam across an applied magnetic field. We find that in the intense beam regime, the propagation is limited due to space-charge depression caused by the deflection of the electron beam by the transverse field. This critical field is of the order of the peak self-magnetic field of the electron beam which is substantially higher than the single particle cutoff field.

2.2.4 Ion Hose Instability of the Bennett Profile Beam

The self-consistent Vlasov equilibrium that leads to the Bennett radial density profile for the downstream electron-ion beam system has been analyzed relative to the ion hose instability. Specifically, we consider the limiting case where the ion beam species is cold, stationary, and provides charge neutralization. The most simple model assumes that each beam is rigid. We then investigate the effects due to the anharmonic nature of the potential well using a ''-pread

27

density" model and the effects due to an axial thermal velocity spread of the electron beam. In addition, nonlinear effects due to large beam displacements are numerically investigated.

For the rigid beam model, the linearized equations for transverse motion of the beams are

$$\ddot{x}_e = \frac{\omega_e^2}{6}(x_i - x_e)$$

$$\ddot{x}_i = \frac{\omega_i^2}{6}(x_i - x_e)$$

and $\dot{z}_e = v_0$, $\dot{z}_i = 0$. We have defined $\omega_e = \sqrt{e^2 n_{i0}/\epsilon_0 \gamma m_e}$, $\omega_i = \sqrt{e^2 n_{e0}/\epsilon_0 m_i}$, $n_{i0} = n_{e0} = n_0$, and the displacements x are assumed to be much less than the beam cross-sectional dimensions a. For harmonic displacements, we find that resonant growth occurs for wavelengths

$$kv_0 = \frac{2\pi}{\lambda}v_0 = \frac{\omega_e}{\sqrt{6}} = \frac{2\pi}{\lambda_{\beta e}}v_0$$

with a complex frequency

$$\omega = \left(\frac{1}{2} + i\frac{\sqrt{3}}{2}\right)\left(\frac{\omega_i^2 \omega_e}{12\sqrt{6}}\right)^{1/3}.$$

where the growth rate is $Im\omega$. The spectrum of growth rates is shown in Fig. 17 by the solid line (R.B.), where the strong resonant growth is clearly seen. The system parameters for this case are $V_0 = 1$ MV, $I_0 = 20$ kA, $\beta_0 = v_0/c = 0.65$, $a = 1$ cm, and $R_w/a = 10$.

The effects due to the Bennett profile which results in particles oscillating at different transverse frequencies are modelled by annular layers with different densities. After weighting by density and averaging to obtain the net beam displacement, we obtain a dispersion relation

$$1 - \left[1 + \frac{\omega}{\sqrt{2}\omega_i}\ell n\frac{\omega - \omega_i/\sqrt{2}}{\omega + \omega_i/\sqrt{2}}\right]\left[1 + \frac{\omega - kv_0}{\sqrt{2}\omega_e}\ell n\frac{\omega - kv_0 - \omega_e/\sqrt{2}}{\omega - kv_0 + \omega_e/\sqrt{2}}\right] = 0.$$

These results are displayed in Fig. 17 by the dashed curve labelled S.D. We see that the spread in transverse oscillation frequency (weighted by density) results in an unstable spectrum up to the peak on axis-value of $\omega_e/\sqrt{2}$, versus up to the average value of $\omega_e/\sqrt{6}$ for the rigid beam (R.B.) model.

The effects due to an axial thermal velocity spread of the electron beam species is modelled by the one-dimensional relativistic Maxwellian distribution. The beam is assumed to be composed of many rigid disks having the same density profile but different axial velocities. These results are shown by the dashed curve in Fig. 17 labeled T.V.
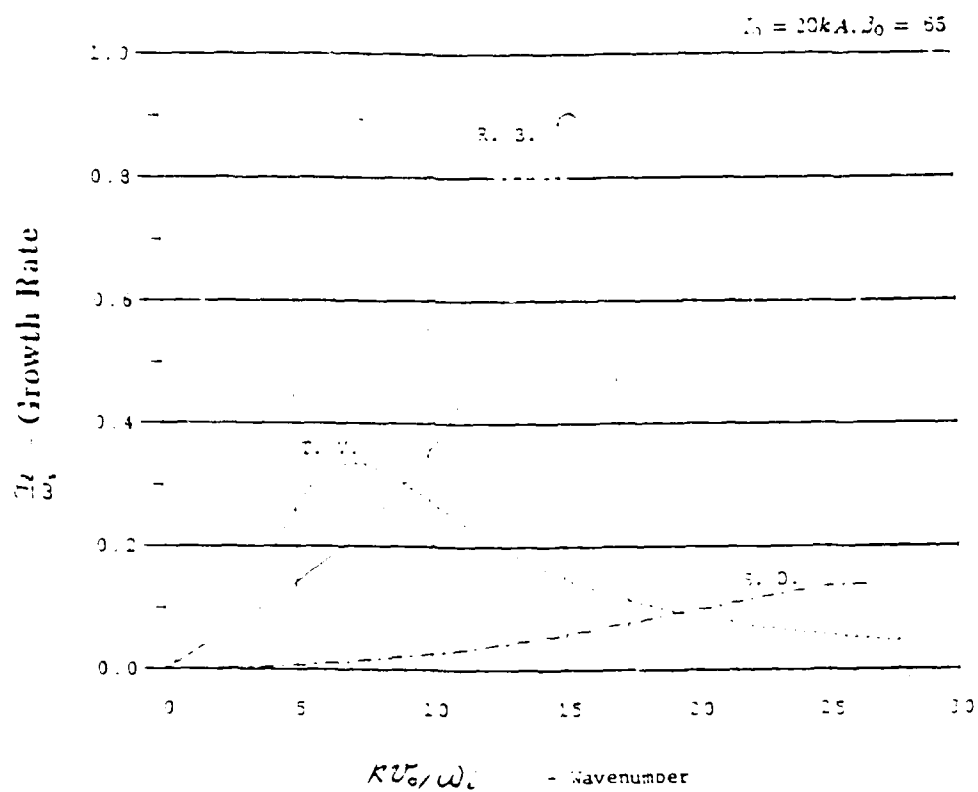
28

Figure 17: Ion hose instability growth rates versus wavenumber. System parameters are: $V_0 = 1$ MV. $I_0 = 20$ kA. R.B. - Rigid beam model; S.D.- Spread density model (anharmonic potential well); T.V. - Thermal velocity spread model.

In summary, our studies of the ion hose instability of a Bennett profile beam indicate:

- From the rigid beam model, the instability exists in the long wavelength region and is weakly absolute. The resonant growth occurs at $\lambda = \lambda_{\beta e}$.

- Due to the anharmonic potential as well as axial velocity spread, the maximum growth is reduced, the unstable region is broadened, and the instability becomes convective.

- For the case of large beam displacements, the nonlinear equations of motion for the ion hose oscillations have been derived for the Bennett profile. As the beam separation becomes of the order of the beam radius, the instability growth decreases and saturates.

2.3 Studies of Pulsed Power Systems and Diagnostics

2.3.1 Circuit Analysis of Pulsed Power Systems

We have carried out a comprehensive circuit analysis of basic pulsed power systems. The electrical pulsed power circuits are classified into two main categories, capacitive- and inductive-energy storage systems. Four basic circuits are found in each category, and they are further classified into lumped- and distributed-circuits. It is noted that the inductive energy systems are the duals of the capacitive energy systems, and vice versa. We proposed two new inductive energy pulsed power systems, which are the duals of LC generator and Blumlein line. Two papers detailing this study are published in Proc. 1989 IEEE Particle Accelerator Conference, p. 1954 (1989), and *Journal of Applied Physics* 67, 4333 (1990); copies are enclosed in Appendix B.

2.3.2 Beam Emittance in a Linear System and a Nonlinear Lens

In this study, we have shown that for a beam of arbitrary distribution function, the rms emittance is invariant under any linear transformation if the determinant of the transfer matrix is unity, and the normalized rms emittance is invariant with a nonunity determinant, which is associated with an axial acceleration of the beam. An exact rms-emittance increase when the beam passes through a nonlinear lens with a spherical aberration is derived. Two

30

papers detailing this study are published in the *Physics of Fluids* 29, 3495 (1986), and *Physics of Fluids B* 2, 452 (1990); copies are enclosed in Appendix B.

APPENDIX A

List of Pa ers and Presentations Resulting from this Grant

1. M. Reiser and W.W. Destler, "Generation of Charge-Neutral, Current-Neutral, Charge Particle Beams," Bull. Am. Phys. Soc. 28, 1038 (1983).

2. D. Welsh, C.D. Striffler, P.G. O'Shea, and W.W. Destler, " Limiting Current of a Solid Relativistic Electron Beam," Bull. Am. Phys. Soc. 28, 1039 (1983).

3. W.W. Destler, P.G. O'Shea, and M. Reiser, "Propagation in Vacuum of an Intense Electron Beam Injected Through a Localized Plasma," Phys. Rev. Lett. 52, 1978 (1984).

4. W.W. Destler, P.G. O'Shea, and M. Reiser, "Propagation of and Intense Relativistic Electron Beam through a Plasma Region into Vacuum," Phys. Fluids 27, 1879 (1984).

5. P.G. O'Shea, D. Welsh, W.W. Destler, and C.D. Striffler, "Intense Relativistic Electron Beam Propagation in Evacuated Drift Tubes," J. Appl. Phys. 55, 3934 (1984).

6. J.T. Cremer, P.G. O'Shea, and W.W. Destler, "Intense Electron Beam Propagation in Vacuum after Injection through a Localized Plasma," Bull. Am. Phys. Soc. (Nov. 1984).

7. C.R. Chang and M. Reiser, "A Theoretical Model of Electron Beam Propagation and Collective Ion Acceleration from Plasma into Vacuum, Bull. Am. Phys. Soc. (Nov. 1984).

8. P.G. O'Shea and W.W. Destler, "Propagation in Vacuum of a Magnetically Confined Intense Electron Beam," Bull. Am. Phys. Soc. (Nov. 1984).

9. H. Dantsker, L.E. Floyd, and C.D. Striffler, "Recent Numerical Simulations of Collective Ion Acceleration in Linear Beam-Localized Plasma Systems," Bull. Am. Phys. Soc. (Nov. 1984).

10. W.W. Destler, P.G. O'Shea, and M. Reiser, "Electron Beam Propagation through a localized Plasma into Vacuum," Phys. Rev. Lett. 52, 1978 (1984).

11. P.G. O'Shea, D. Welsh, W.W. Destler, and C.D. Striffler, "Intense Relativistic Electron Beam Propagation in Evacuated Drift Tubes," J. Appl. Phys. 55, 3934 (1984).

12. W.W. Destler, P.G. O'Shea, and M. Reiser, "Experimental Study of Electron Beam Propagation through a Localized Plasma into Vacuum," Phys. Fluids 27, 1897 (1984).

13. L.E. Floyd and W.W. Destler, "Experimental Study of the Collective Acceleration of Deuterons," submitted to J. Appl. Phys., September 1984.

14. M.J. Rhee, "Compact Thomson Spectrometer," Rev. Sci. Instrum. 55, 1229 (1984).

15. R.F. Schneider and M.J. Rhee, "Resolution Analysis of the Thomson Spectrometer," J. Appl. Phys. 56 (December 1984).

16. R.F. Schneider, C.M. Luo, and M.J. Rhee, "Thomson Spectrometer Revolution Analysis," IEEE Conf. Record-Abstracts, 1984 Int. Conf. on Plasma Science, p. 71, St. Louis, MO (1984).

17. M.J. Rhee, R.F. Schneider, and J.R. Smith, " Constant Energy Per Charge of Ions Produced in Plasma Focus and Collective Ion Acceleration Experiments," IEEE Conf. record-Abstracts, 1984 IEEE Int. Conf. on Plasma Science, p. 86, St. Louis, Mo (1984).

18. R.F. Schneider and M.J. Rhee, "A Stereoscopic Pinhole Camera Study of a Plasma Focus Produced Ion Beam," 1985 IEEE Int. Conf. on Plasma Science, Pittsburgh, PA, February 1985.

19. W.W. Destler, P.G. O'Shea, and Z. Segalov, "Collective Acceleration and the Propagation of Intense Beams into Vacuum," IEEE Trans. Nucl. Sci. NS-32, 2201 (1985), invited paper.

20. M. Reiser, "Transport of High-Intensity Beams" IEEE Trans. Nucl. Sci. NS-32, 2201 (1985), invited paper.

21. M.J. Rhee and R.F. Schneider, "Root-Mean-Square Emittance of Axisymmetric Beam with Maxwellian Velocity Distribution," Part Acc. 20, 133-141 (1985).

22. M. Reiser, "High-Current Beam Transport and Charge-Neutralization Effects," presented at Ion Injection Workshop, San Diego, CA, May 1985.

23. Z. Segalov, W.W. Destler, P.G. O'Shea, C.D. Striffler, X. Zhang, and R.J. Faehl, "Propagation of an Intense Relativistic Electron Beam through a Plasma Region into Vacuum," Bull. Am. Phys. Soc. <u>21</u> (5), 1505 (1985).

24. M.J. Rhee and R.F. Schneider, "Root-Mean-Square Emittance Analysis of Axisymmetric Beam with Maxwellian Velocity Distribution," Bull. Am. Phys. Soc. <u>21</u> (5), 1420 (1985).

25. M.J. Rhee, "Inductively Insulated Marx Generator," Rev. Sci. Instrum. <u>57</u> (2), 170 (February 1985).

26. M. Reiser, "High-Current Beam Dynamics and Transport, Theory and Experiment," Linear Accelerator Conference, Stanford, CA, June 1986.

27. D.J. Weidman, M.J. Rhee, and R.F. Schneider, "Time-Resolved Thomson Spectrometer Study of Plasma Focus Produced Ions," 1986 IEEE International Conference on Plasma Science, Saskatoon, Canada, May 19-21, 1986.

28. M.J. Rhee, "Electromagnetic Fields Radiated by an Intense Relativistic Charged Particle Beam Injected into an Open Space," submitted to Am. J. Phys., July 1986.

29. M.J. Rhee, "Invariance Properties of the Root-Mean-Square Emittance in a Linear System," Phys. Fluids <u>29</u>, 3495 (1986).

30. W.W. Destler, R.J. Faehl, P.G. O'Shea, M. Reiser, Z. Segalov, C.D. Striffler, and X. Zhang, "Intense Beam Propagation Properties in Magnetized and Localized Ion Source Configurations," Beams '86, Sixth Int. Conf. on High Power Particle Beams, Kobe, Japan, June 9-12, 1986.

31. W.W. Destler, P.G. O'Shea, J. Rodgers, Z. Segalov, and J. Sutter "Laser Controlled Collective Ion Accelerator," Twenty-Eighth Annual Meeting, Division of Plasma Physics, Baltimore, November 3-7, 1986.

32. D.J. Weidman and M.J. Rhee, "Design and Operation of a Time-Resolving Thomson Spectrometer," Twenty-Eighth Annual Meeting, Division of Plasma Physics, Baltimore, November 3-7, 1986.

33. X. Zhang and C.D. Striffler, "Analytic Model of Intense Beam Propagation through a Localized Source of Ions into Vacuum," Twenty-Eighth Annual Meeting, Division of Plasma Physics, Baltimore, November, 3-7, 1986.

34. M. Reiser and C.R. Chang, "Computer Simulation Studies of Electron Beam Propagation through Plasma into Vacuum, J. Appl. Phys. 61, 899 (1987).

35. M.J. Rhee, R.F. Schneider, and D.J. Weidman, "Simple Time-Resolving Thomson Spectrometer," Rev. Sci. Instrum. 58, 240 (1987).

36. P.G. O'Shea, W.W. Destler, J. Rodgers, and Z. Segalov, "Laser Controlled Collective Ion Accelerator," Appl. Phys. Lett. 49, 1696 (1986).

37. C.R. Chang and M. Reiser, "Computer Simulation Studies of Electron Beam Propagation and Collective Ion Acceleration in Vacuum," 1987 Particle Accelerator Conference, Washington, DC, March 1987.

38. X. Zhang and C.D. Striffler, "Intense Beam Propagation with No Applied Magnetic Field," 1987 Particle Accelerator Conference, Washington, DC, March 1987.

39. W.W. Destler, P.G. O'Shea, J. Rodgers, Z. Segalov, and J. Sutter, "Collective Ion Acceleration Via Laser Controlled Ionization Channel," 1987 Particle Accelerator Conference, Washington, DC, March 1987.

40. W.W. Destler, P.G. O'Shea, and Z. Segalov, "Experimental Study of Propagation of Intense Relativistic Electron Beams in Nonconducting Vacuum Drift Tubes after Passage through a Localized Plasma Source," J. Appl. Phys. 61, 2458 (1987).

41. X. Zhang, R.L. Yao, and C.D. Striffler, "Equilibrium and Stabil; " of an Intense Beam System with No Applied Magnetic Field," Bull. Am. Phys. Soc. 32, 1719 (1987).

42. R.L. Yao, C.D. Striffler, and J.G. Guillory, "Collective Ion Acceleration, Intense Beam Propagation, and Plasmoid Emission in a Localized Plasma Source-Vacuum System," Bull. Am. Phys. Soc. 32, 1719 (1987).

43. X. Zhang, R.L. Yao, and C.D. Striffler, "An Intense Beam System with No Applied Magnetic Field," 1987 IEEE Int. Conf. on Plasma Sci., June 1-3, 1987, Arlington, VA, p. 97.

44. R.L. Yao, C.D. Striffler, and J. Guillory, "Intense Beam Propagation and Collective Ion Acceleration in a Localized Plasma Source-Vacuum System," 1987 IEEE Int. Conf. on Plasma Sci., June 1-3, 1987, Arlington, VA, p. 97.

45. W.W. Destler, C.D. Striffler, Z. Segalov, R.L. Yao, Z. Zhang, and J. Rodgers, "Intense Charged Particle Beam Propagation into Vacuum," Proceedings of O-E/LASE '88, Symposium on Innovative Science and Technology, paper 873-33; January 10-15, 1988.

46. R.L. Yao and C.D. Striffler, "Numerical Simulation of Collective Ion Acceleration in a Localized Plasma Source-Vacuum System," Spring 1988 APS Meeting, Bull. Am. Phys. Soc. 33, 1082 (1988).

47. X. Zhang, C.D. Striffler, and R. Yao, "Equilibria of an Intense Beam System with no Applied Magnetic Field," Spring 1988 APS Meeting, Bull. Am. Phys. Soc. 33, 986 (1988).

48. R.L. Yao and C.D. Striffler, "Numerical Simulation of Collective Ion Acceleration in a Localized Plasma Source-Vacuum System," 1988 IEEE International Conference on Plasma Science, June 6-8, 1988, paper 6PS2, pg. 145.

49. R.L. Yao, J. Guillory, and C.D. Striffler, "Numerical Simulation of Intense Beam Propagation and Plasmoid Formation in a Localized Plasma Source-Vacuum System," 1988 IEEE International Conference on Plasma Science, June 6-8, 1988, paper 5P8, pg. 123.

50. X. Zhang, C.D. Striffler, and R. Yao, "Stability of an Intense Beam System with no Applied Magnetic Field," 1988 IEEE International Conference on Plasma Science, June 6-8, 1988, paper 5P7, pg. 122.

51. W.W. Destler, J. Rodgers, Z. Segalov, C.D. Striffler, R. L. Yao, X. Zhang, and J. Guillory, "Review of Intense Electron Beam Transport in Gases," Invited Paper, BEAMS

'88, Seventh International Conference on High-Power Particle Beams, Karlsruhe, Germany, July 4-8, 1988.

52. R.L. Yao, M.J. Rhee, T.A. Fine, W.W. Destler, and C.D. Striffler, "Collective Ion Acceleration in a Localized Ion Source System," BEAMS '88, Seventh International Conference on High-Power Particle Beams, Karlsruhe, Germany, July 4-8, 1988.

53. C.D. Striffler, R.L. Yao, and X. Zhang, Presentations at "Ion Beam and Plasmoid Propagation Workshop," October 18-19, 1988 at SAIC, on "Propagation of Electron-Ion Beam Through Transverse Magnetic Field," and "Equilibrium and Stability of Electron-Ion Beam in Laboratory Experiments."

54. C.D. Striffler and R.L. Yao, "Numerical Simulation of Collective Ion Acceleration in a Localized Plasma Source-Vacuum System," 1988 Plasma Physics APS Meeting, Bull. Am. Phys. Soc. 33, 1983 (1988).

55. X. Zhang, R.L. Yao, and C.D. Striffler, "Stability of an Intense Beam System with no Applied Magnetic Field," 1988 Plasma Physics APS Meeting, Bull. Am. Phys. Soc. 33, 1955 (1988).

56. R.L. Yao, J. Guillory and C.D. Striffler, "Numerical Simulation of Intense Beam Propagation and Plasmoid Formation in a Localized Plasma Source-Vacuum System," 1988 Plasma Physics APS Meeting, Bull. Am. Phys. Soc. 33, 1955 (1988).

57. W.W. Destler, J. Rodgers, and Z. Segalov, "Vacuum Propagation of Co-Moving Electron/Ion Beams," Bull. Amer. Phys. Soc. 33, 1955 (1988).

58. J. Rodgers, W.W. Destler, and Z. Segalov, "Experimental Studies of the Laser-Controlled Collective Ion Accelerator Concept," Bull. Amer. Phys. Soc. 33, 1983 (1988).

59. M.J. Rhee and D.J. Weidman, "Temporal Evaluation of Ion Energy in a Plasma Focus," Phys. Fluids 31, 703 (1988).

60. F. Begay, T.A. Fine, H. Griem, R.A. Hess, and M.J. Rhee, "Spectroscopic Study of Collective Ion Acceleration Experiments," IEEE Conf. Record-Abstracts, 1988 IEEE ICOPS, June 6-8, 1988, Seattle, Washington, p. 49.

61. M.J. Rhee, F. Begay and T.A. Fine, "Thomson Spectrometer Studies of Collectively Accelerated Ions," IEEE Conf. Record-Abstracts, 1988 IEEE ICOPS, June 6-8, 1988, Seattle, Washington, p 134.

62. M.J. Rhee, E. Boggasch, and T.A. Fine, "Behavior of Net Current in a Gas Filled Drift Tube," Bull. Am. Phys. Soc. 33, 1950 (1988).

63. T.A. Fine, M.J. Rhee, and D.J. Weidman, "Time-Resolved Thomson Spectrometer Study of Collective Ion Acceleration," Bull. Am. Phys. Soc. 33, 1986 (1988).

64. F. Begay, E. Boggasch, A.W. Desilva, T.A. Fine, H. Griem, J. Moreno, M.J. Rhee, and D.J. Weidman, "Light as a Plasma Probe," Bull. Am. Phys. Soc. 33, 2053 (1988).

65. M. Reiser, Invited presentation at Panel Discussion of BEAMS '88, Seventh International Conference on High-Power Particle Beams, Karlsruhe, W. Germany, July 4-8, 1988.

66. E. Boggasch, T. A. Fine, and M. J. Rhee, "The Pseudospark as an Electron Beam Source," Bull. Am. Phys. Soc. 34, 194 (1989).

67. T. A. Fine, E. Boggasch, and M. J. Rhee, "Current Measurements in a Gas Filled Drift Tube," Bull. Am. Phys. Soc. 34, 233 (1989).

68. M. J. Rhee and T. A. Fine, "Circuit Description of Pulse Power Systems," Bull. Am. Phys. Soc. 34, 279 (1989).

69. T. A. Fine and M. J. Rhee, "Dynamic Behavior of IREB in a Collective Ion Acceleration Experiment," IEEE Conference Record-Abstracts, 1989 IEEE International Conference on Plasma Science, p. 83 (1989).

70. E. Boggasch and M. J. Rhee, "Pseudospark as an Electron Beam Source," IEEE Conference Record-Abstracts, 1989 IEEE International Conference on Plasma Science, p. 100 (1989).

71. D. J. Weidman and M. J. Rhee, "Curve Fitting Analysis of Time-Resolved Thomson Spectrograms from a Plasma Focus," IEEE Conference Record-Abstracts. 1989 IEEE International Conference on Plasma Science, p. 104 (1989).

72. C. C. Kung and M. J. Rhee, "Circuit Description of Inductive Energy Storage Pulsed Power Systems," IEEE Conference Record-Abstracts. 1989 IEEE International Conference on Plasma Science, p. 125 (1989).

73. D. J. Weidman, C. B. Daniel, and M. J. Rhee, "Large-Scale Study of Time-Resolved Thomson Spectrograms from a Plasma Focus," Bull. Am. Phys. Soc. 34, 1946 (1989).

74. M. J. Rhee and E. Boggasch, "High Brightness Electron Beam Produced by a Pseudospark Discharge," Bull. Am. Phys. Soc. 34, 1991 (1989).

75. T. A. Fine, E. Boggasch, and M. J. Rhee, "Current Measurements in a Gas Filled Drift Tube," Proc. 1989 IEEE Particle Accelerator Conference, 1052 (1989).

76. M. J. Rhee and T. A. Fine, "Circuit Description of Pulsed Power Sytstems," Proc. 1989 IEEE Particle Accelerator Conference, 1052 (1989).

77. E. Boggasch, T. A. Fine, and M. J. Rhee, "The Pseudospark as an Electron Beam Source," Proc. 1989 IEEE Particle Accelerator Conference, 316 (1989).

78. E. Boggasch and M. J. Rhee, "Experimental Study of Pseudospark-Produced Electron Beams," AIP Conference Proceedings 195, Dense Z-Pinches, 418 (1989).

79. M. J. Rhee and E. Boggasch, "Emittance Measurement of a Pseudospark-Produced Electron Beam," to be published in Proc. Phys. and Appl. of High Power Hollow Electrode Glow Switches, (1989).

80. T. A. Fine and M. J. Rhee, "Anode Foil Changer for High-Current Relativistic Electron Beam Diode System," Rev. Sci. Instrum. 60, 3556 (1989).

81. M. J. Rhee, "Root-Mean-Square Emittance Increase in a Nonlinear Lens," Phys. Fluids B, 2, (2) (1990).

82. M. J. Rhee, T. A. Fine, and C. C. Kung, "Basic Circuits for Inductive-Energy Pulsed Power Systems," J. Appl. Phys. 67, (9) (1990).

83. R.L. Yao and C.D. Striffler, "Numerical simulation of collective ion acceleration in an intense electron beam-localized gas cloud system," to be published in J. Appl. Phys., Feb. 1990.

84. X. Zhang, C.D. Striffler, R.L. Yao, W.W. Destler, and M.P. Reiser, "Intense Electron Beam Propagation Across a Magnetic Field," Proc. 1989 IEEE Particle Accelerator Conference, March 20-23, 1989, Chicago, IL, pp. 1035-1037.

85. X. Zhang, C.D. Striffler, R.L. Yao, "Ion Hose Instability of a Beam with a Bennett Profile," Bull. Am. Phys. Soc. 34, 2103 (1989).

86. R. L. Yao, W. W. Destler, C. D. Striffler, J. Rodgers, Z. Segalov, "Measurements and Simulations of Controlled Beamfront Motion in the Laser Controlled Collective Accelerator," Proc '989 IEEE Part. Accel. Conf., March 20-23, 1989, Chicago, IL, pp. 624-626.

87. R.L. Yao, C.D. Striffler, and W.W. Destler, "Numerical Simulation of Collective Ion Acceleration in the Laser Controlled Collective Accelerator," 1989 IEEE Int. Conf. on Plasma Science, May 22-24, 1989. p. 56, paper IP27.

88. R.L. Yao, W.W. Destler, P. Huang, J. Rodgers, and C.D. Striffler, "Measurements and Simulation of Controlled Beam-Front Motion and Collection Ion Acceleration in the Laser Controlled Collective Ion Accelerator," Bull. Am. Phys. Soc. 34, 1991 (1989).

89. W.W. Destler, J. Rodgers, and Z. Segalov, "Experimental studies of the laser-controlled collective ion accelerator," J. Appl. Phys. 66, 2894 (1989).

90. E. Boggasch and M. J. Rhee, "High-Brightness Pseudospark-Produced Electron Beam," Appl. Phys. Lett. 56, 1746 (1990).

91. M. J. Rhee, K. K. Jain, and R. F. Schneider, "Phase Space Measurements by a Finite-Width Slit," IEEE Conference Record-Abstracts, 1990 IEEE International Conference on Plasma Science, p. 162 (1990).

41

92. K. K. Jain and M. J. Rhee, "Investigation of Repetitive High Quality Electron Beam from a Pseudospark," IEEE Conference Record-Abstracts, 1990 IEEE International Conference on Plasma Science, p. 162 (1990).

93. M. J. Rhee, "Beam Energy Reduction in an Acceleration Gap," IEEE Conference Record-Abstracts, 1990 IEEE International Conference on Plasma Science, p. 197 (1990).

94. R. F. Schneider and M. J. Rhee, "Emittance Measurements Using a Finite Slit-Hole Emittance Meter," IEEE Conference Record-Abstracts, 1990 IEEE International Conference on Plasma Science, p. 216 (1990).

95. K. K. Jain, E. Boggasch, M. Reiser, and M. J. Rhee, "Experimental Investigation of a Pseudospark Produced High-Brightness Electron Beam," to appear in Phys. Fluids B $\underline{2}$, (10) (1990).

96. K. K. Jain and M. J. Rhee, "Experimental Investigation of Pseudospark-Produced Electron Beams," to appear in Proc. of BEAMS '90.

97. X. Zhang, C.D. Striffler, and R. Yao, "Ion Hose Instability of an Intense Beam with a Bennet Profile, Bull. APS $\underline{35}$, 932 (1990).

98. X. Zhang, C.D. Striffler, and R.L. Yao, "Ion Hose Instability of an Intense Beam with a Bennet Profile," 1990 IEEE International Conf. on Plasma Science, pp. 219 (1990).

APPENDIX B

Copies of Selected Papers Published and/or Presented Under this Grant

Experimental studies of the laser-controlled collective ion accelerator

W. W. Destler, J. Rodgers, and Z. Segalov

Electrical Engineering Department and Laboratory for Plasma Research, University of Maryland, College Park, Maryland 20742

Detailed experimental studies of a collective acceleration experiment in which a time-sequenced laser-generated ionization channel is used to control the propagation of an intense relativistic electron beamfront are presented. Ions trapped in the potential well at the beamfront are accelerated as the velocity of the beamfront is increased in a manner controlled by the time-dependent axial extent of the ionization channel. Beamfront propagation data for two different accelerating gradients are presented, together with results of ion acceleration studies for both gradients.

I. INTRODUCTION

Interest in collective acceleration has arisen because the relatively high electric fields (100–1000 MV/m) that can be generated in relativistic electron beam systems are higher than can be easily maintained in conventional accelerator structures.[1,2] A typical collective accelerator involves the injection of an intense relativistic electron beam into a source of positive ions to be accelerated. Ion sources used have included neutral gas-filled drift tubes,[3,4] a neutral gas cloud localized to the injection region,[5-7] or a dielectric anode material (the Luce diode[8,9]). In each case, if the beam is injected at a sufficiently high current level, a virtual cathode forms immediately downstream of the injection point and ions can be produced and trapped by the potential well associated with the virtual cathode. Ion acceleration to energies in excess of the electron beam energy can occur as the virtual cathode moves downstream of the injection point, usually as a result of a gradual neutralization of the electron beam space charge by increasing numbers of ions generated by electron-impact and ion-ion avalanche ionization processes.

Although considerable progress has been achieved in the study of such "naturally occurring" collective acceleration processes in recent years,[3-10] the goal of controlling the acceleration process over longer distances has proven an elusive one. To date, the most successful experiments in this regard have been the IFA-1 and IFA-2 ionization front accelerator experiments of Olson.[11,12] Recently, our group reported initial successful operation of a laser-controlled collective ion acceleration experiment, based on the same fundamental concepts as the IFA experiments but significantly different in both design and operation.[13] In this paper, detailed experiments conducted in an attempt to understand the potentials and limitations of this new collective accelerator configuration are reported, including detailed measurements of controlled beamfront motion in experimental configurations designed for two different accelerating gradients. Results of ion acceleration experiments utilizing both gradients are reported and compared with theoretical expectations. In Sec. II of this paper the accelerator concept is described and basic design considerations are discussed. Experiments conducted to investigate the concept are described in Sec. III, and conclusions are drawn in Sec. IV.

II. THEORETICAL DISCUSSION

The basic concept behind the experiment is shown in Fig. 1. An intense relativistic electron beam (900 keV, 20 kA, 30 ns) is injected into an evacuated drift tube at a current level several times the vacuum space-charge limit, given approximately[14] by

$$I_I = \frac{17\,000(\gamma_0^{2/3} - 1)^{3/2}}{[1 + 2\ln(b/a)](1 - f)} \quad (A), \tag{1}$$

where b is the drift tube radius, a is the beam radius, γ_0 is the relativistic mass factor for the electrons at injection, and $f = n_i/n_e$ represents any charge neutralization provided by positive ions. As indicated in Fig. 1(a), a virtual cathode forms at the injection point with a depth approximately equal to the anode–cathode potential difference. The axial position of the virtual cathode downstream of the anode plane is usually on the order of the anode cathode gap,[15] so that megavolt potentials at the virtual cathode are formed only millimeters away from the grounded anode. It is this very high electric field on the upstream side of the virtual cathode that collective accelerators usually seek to exploit for ion trapping and acceleration.
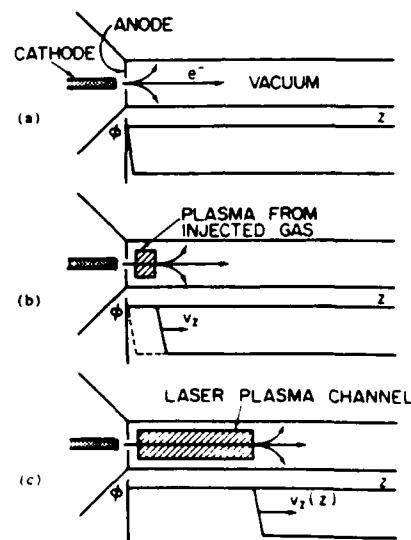

FIG. 1. Conceptual design of laser-controlled accelerator.

If the beam is injected into a localized gas cloud [Fig. 1(b)], ionization processes can quickly build up sufficient ion density to neutralize the electron beam space charge and the virtual cathode can move downstream to the edge of the gas cloud. This motion can result in the acceleration of a few ions to energies considerably higher than that associated with the depth of the potential well at the virtual cathode.

In order to control the motion of the virtual cathode over distances greater than a few centimeters, however, a means of providing an ionization channel whose axial extent can be controlled as a function of time is required [Fig. 1(c)]. In the present experiments, shown schematically in Fig. 2, the ionization channel is generated by time-sequenced laser-target interactions. A laser pulse is separated into ten approximately equal energy beams which are then optically delayed over different path lengths. The laser light then vaporizes and ionizes a target material on the drift tube wall, and ions drawn into the beam by the electron space charge at the beamfront provide the required time-sequenced channel of ionization to control beamfront motion.

This basic concept of operation results in a number of constraints on the design of the experiment The requirement that the injected beam current be several times the vacuum space-charge limit imposes a lower bound on the drift tube radius of about twice the beam radius. An upper bound for the drift tube radius is set by the requirement that ions created at the drift tube wall be drawn into the beam in a time less than or equal to the delay time between two adjacent laser pulses.

If the virtual cathode is accelerated continuously from a low initial velocity to a higher final one, ions will be trapped within the potential well at the beamfront only if the relative velocity of the well and the ions is less than a value given by

$$v_w - v_i < (2eV_0/m_i)^{1/2} \qquad (2)$$

where V_0 is the depth of the potential well associated with the virtual cathode. This result yields $v_w - v_i < 0.44$ c for a 900-keV electron beam. Another constraint upon the acceleration process is that the electric field associated with the virtual cathode at the beamfront must be large enough that ions remain trapped during the acceleration process. This imposes a limit on the accelerating gradient given by
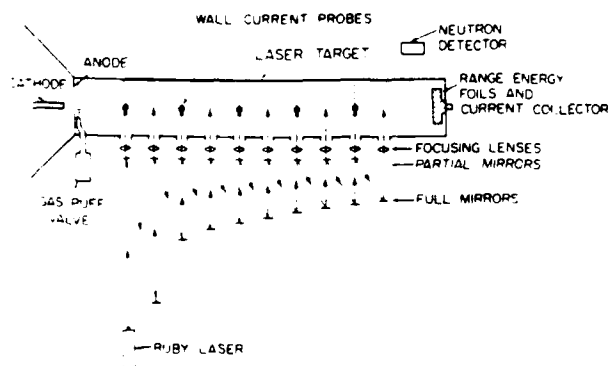
$$v_i \approx v_w < eE/m_i. \qquad (3)$$

FIG 2. Experimental configuration.

Although electric fields associated with the virtual cathode at the injection point can be as high as 100–1000 MV/m, beam dynamics at the beamfront as the beam propagates downstream may reduce these field strengths considerably. In addition, oscillations of the trapped ions in the potential well at the beamfront and fluctuations in the depth of the potential well should also be considered.

In addition to these considerations, the laser-target geometry must be carefully designed such that electron beam ionization of the target is negligible. Only if this requirement is satisfied will effective control over the beamfront motion by the laser be possible.

III. EXPERIMENT

A. Apparatus

The basic experimental configuration is shown in Fig. 2. An intense relativistic electron beam (900 keV, 20 kA, 30 ns FWHM) is emitted from a 4-mm-diam tungsten cathode located 1 cm upstream of a stainless-steel anode. A 14-mm-diam hole in the anode plate allows almost all of the beam current in the diode to pass into the downstream drift chamber. A drift chamber diameter of 10 cm was chosen on the basis of both theoretical calculations described in the previous section and experimental measurements of beam propagation in dielectric-lined drift tubes of various diameters.[16] Seed protons for acceleration were produced by electron-impact and ion-ion avalanche ionization of a localized hydrogen gas cloud produced by a fast gas puff valve. At the time of electron beam injection, the localized gas cloud was measured to extend no more than 2 cm into the vacuum drift tube. The laser target geometry chosen consisted of a 5-mm-wide strip of 0.8-mm-thick polyethylene (CH_2) sheet mounted in a stainless-steel bracket that allowed for axial movement of the target if necessary to provide a fresh target spot for the laser pulse. Experimental tests have confirmed that electron beam ionization of the laser target material is not sufficient to allow beam propagation downstream.[16] A Q-switched ruby laser (6 J, 15 ns) was divided into ten approximately equal energy beams and optically delayed to provide a time-sequenced source of ions down the 50 cm length of the drift tube. Optical tests of the system[16] have demonstrated that actual laser energy on the target varied from a maximum of 0.55 J at the first target spot to a minimum of 0.32 J at the last, with differences primarily due to optical losses in the system. Each laser beam was focused to a diameter of less than 1 mm on the target surface by a focusing lens, ensuring adequate laser power density (about 1–2 GW/cm^2) for plasma production.[17]

The following diagnostics were employed to monitor the control of the electron beamfront and the subsequent acceleration of ions in the accelerator. A Faraday cup current collector was installed at the downstream end of the drift tube to measure the total beam current propagated to this point. Five current collecting wall probes were also installed at axial positions 10, 20, 30, 40, and 50 cm downstream of the anode plane to measure beam current deflected to the drift tube wall at the beamfront as a function of time. The current probes consisted of open-ended 50-Ω semirigid coaxial cables with an effective collection area of about 2

mm^2. The energy of accelerated protons was determined using stacked foil nuclear activation techniques. Titanium [Ti$^{47}(p,n)$V^{47}] and copper [Cu$^{63}(p,n)$Zn^{63}] reactions were used having threshold energies of 3.7 and 4.2 MeV, respectively.

Neutrons produced by the interaction of accelerated protons with the target foils and with the drift tube walls were also measured using a silver activation neutron detector.

B. Results

Experiments were conducted using two sets of optical delays designed to smoothly accelerate the electron beamfront from 0.05 to 0.2 c and from 0.05 to 0.3 c over a distance of 45 cm. These corresponded to accelerating gradients of approximately 40 and 90 MV/m, respectively. Results of measurements of the beamfront motion down the drift tube as a function of time as determined from the arrival time of electron current pulses at the wall probes are shown in Figs. 3 and 4. In Fig. 3 is also shown typical beamfront propagation data for the case where the laser is fired 200 ns in advance of the beam, and the beam propagates freely downstream neutralized by a preformed plasma channel, and for the case where the laser is not fired at all, in which case beam propagation downstream can only occur as rapidly as accelerated ions from the gas cloud propagate downstream. Results for the case where the laser is swept along the target just as the electron beam is injected into the drift tube indicate that effective control is exercised by the laser in good agreement with design values for both accelerating gradients (Fig. 4). Peak currents measured by the wall probes both with and without the laser are plotted in Fig. 5, and indicate that, as expected, the laser allows more effective current propagation downstream than is possible in vacuum, even when wall currents are used as an indicator of beam transport.

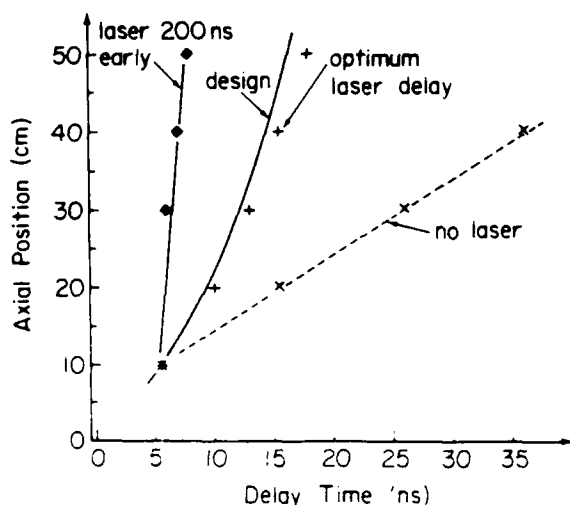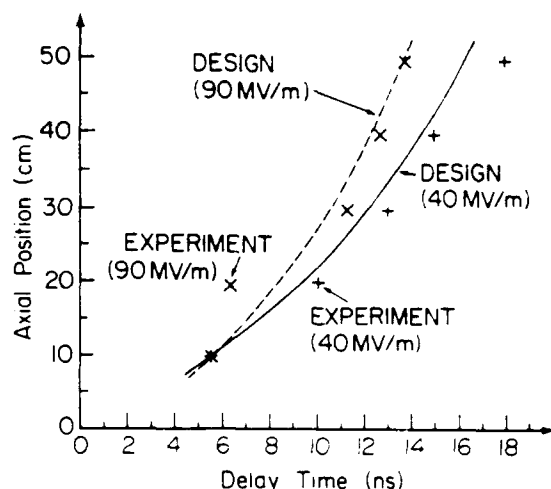Data from Faraday cup measurements of the total elec-

FIG. 4. Wall probe measurements of beamfront propagation vs time for optimum laser firing delay, 40 MV/m accelerating gradient and 90 MV/m accelerating gradient.

tron beam current reaching the downstream end of the drift tube as well as neutron counts and measured ion energies for the two different accelerating gradients are shown in Figs. 6 and 8 as a function of the delay time between the firing of the laser and the firing of the electron beam. It is easily seen from the data that firing the laser too early in time simply allows all of the beam current to flow rapidly downstream as indicated from the wall current probes. Firing the laser too late, which is equivalent to not firing the laser at all, results in greatly reduced currents collected by the Faraday cup, as expected. It is clear that the firing delays corresponding to the transition from total beam current propagation (ions produced too early with regard to beam injection) to little beam propagation (ions produced too late to provide neutralization) are those that should result in control of the virtual cathode motion down the drift tube. It is therefore expected that high-energy ions should be only observed within this range of firing delays. Data for the 40 MV/m

FIG. 3. Wall probe measurements of beamfront propagation vs time for optimum laser firing. laser-fired 200 ns in advance of electron beam injection. and without laser (40 MV/m accelerating gradient).
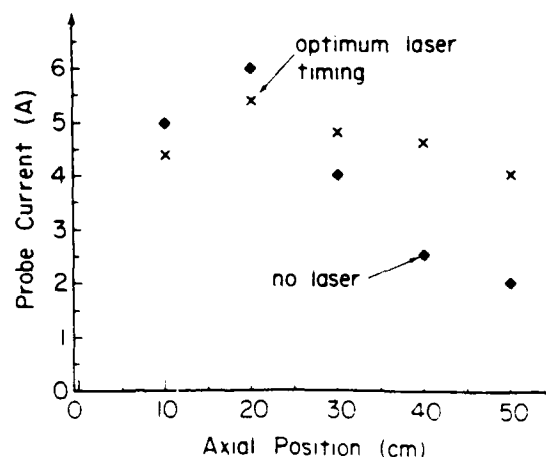

FIG. 5. Peak wall current pulse amplitudes vs axial position for both optimum laser firing delay and no-laser experiments. Collection area of wall probes is about 2 mm^2.

experiments (Fig. 6) clearly show an increase in observed peak proton energies at this point to values consistent with design expectations. About 10^9 protons/pulse were accelerated to the peak energy of about 18 MeV. Although the foil activation results do not easily yield an ion energy spectrum, the data are consistent with a spectrum having a substantial peak at about 18 MeV, as shown in Fig. 7. Data for the 90 MV/m experiments (Fig. 8), however, show some enhancement of accelerated proton energies over the no-laser results, but not to the designed value of about 41 MeV.

IV. CONCLUSIONS

Effective control of a relativistic electron beamfront by a laser-produced time-sequenced ionization channel has clearly been demonstrated for two different accelerating gradients. In addition, beamfront motion without the laser-produced ionization channel is consistent with theoretical expectations, as is the rapid propagation observed when the ionization channel is produced well in advance of electron beam injection.

Controlled collective acceleration of ions at a rate of 40 MV/m over a distance of 50 cm has also been demonstrated, but acceleration at the higher gradient (90 MV/m) has not been demonstrated to date. This is undoubtedly attributable to the difficulty in maintaining the required > 90 MV/m
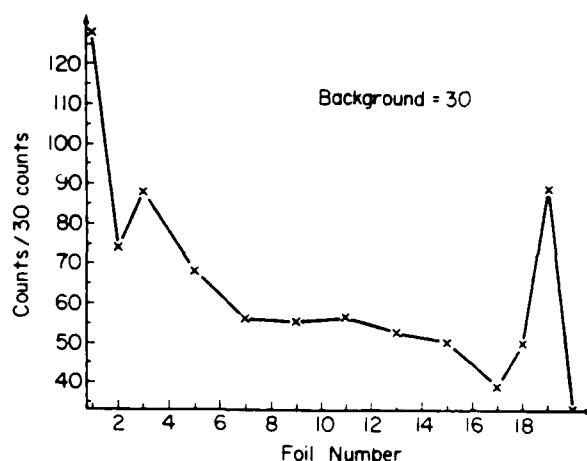

FIG. 7. Counts from activated 2-mil titanium foils vs foil number in the target stack, 40 MV/m accelerating gradient.

electric fields at the virtual cathode over the entire 50-cm accelerating distance. Higher accelerated ion energies will require, therefore, either longer accelerating distances and therefore longer electron beam pulse durations, or alternatively higher injected beam currents and energies to maintain higher electric fields at the virtual cathode. Future experiments are planned to investigate both of these possibilities.
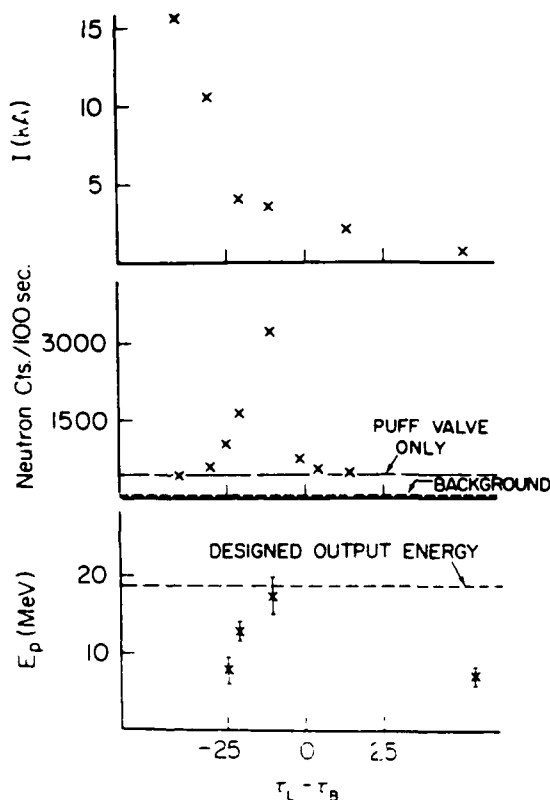

FIG 6. Propagated current, neutron production, and peak proton energy as a function of firing delay between the laser pulse and first rise of electron beam pulse in the diode in nanoseconds, 40 MV/m accelerating gradient
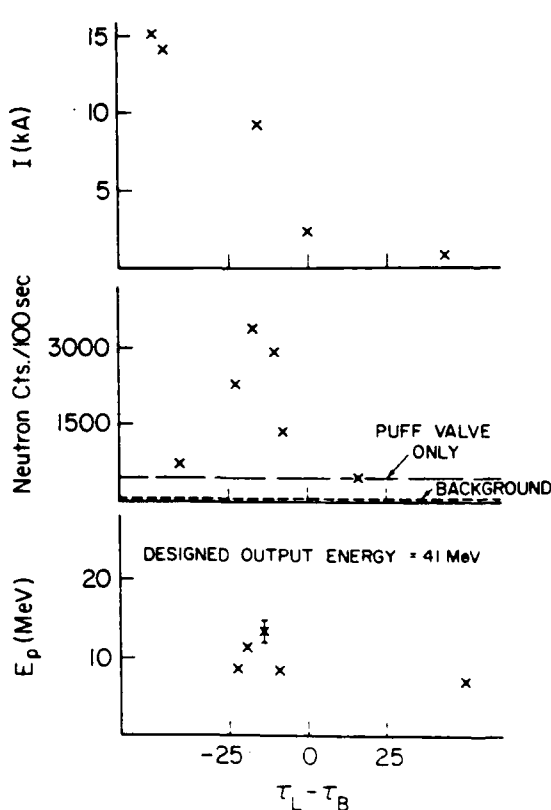

FIG. 8. Propagated current, neutron production, and peak proton energy as a function of firing delay between the laser pulse and first rise of electron beam pulse in nanoseconds, 90 MV/m accelerating gradient.

2897   J. Appl. Phys., Vol. 66, No. 7, 1 October 1989

Destler, Rodgers, and Segalov   2897

ACKNOWLEDGMENTS

[1]G. J. Budker, At. Energy Aust. **1**, 9 (1956).

[2]V. I. Veksler, in Proceedings of the Sixth International Conference on High Energy Accelerators, Cambridge, MA, 1967 (unpublished).

[3]S. E. Graybill and J. R. Uglum, J. Appl. Phys. **41**, 236 (1970).

[4]C. L. Olson, Phys. Fluids **18**, 585 (1975).

[5]W. W. Destler, L. E. Floyd, and M. Reiser, Phys. Rev. Lett. **44**, 70 (1980).

[6]W. W. Destler and J. T. Cremer, J. Appl. Phys. **54**, 636 (1983).

[7]J. T. Cremer and W. W. Destler, J. Appl. Phys. **57**, 4391 (1985).

[8]J. S. Luce, Ann. N.Y. Acad. Sci. **20**, 336 (1973).

[9]R. Adler, J. A. Nation, and V. Serlin, Phys. Fluids **24**, 347 (1981).

[10]R. F. Hoeberling and D. N. Payton III, J. Appl. Phys. **48**, 2079 (1977).

[11]C. L. Olson and U. Schumacher, in *Springer Tracts in Modern Physics: Collective Ion Acceleration*, edited by G. Hobler (Springer, New York, 1979), Vol. 84.

[12]C. L. Olson, C. A. Front, E. L. Patterson, J. P. Anthes, and J. W. Poukey, Phys. Rev. Lett. **56**, 2260 (1986).

[13]P. G. O'Shea, W. W. Destler, J. Rodgers, and Z. Segalov, Appl. Phys. Lett. **49**, 1696 (1986).

[14]L. S. Bogdankevich and A. A. Rukhadze, Usp. Fiz. Nauk. **103**, 609 (1971) [Sov. Phys. Usp. **14**, 163 (1971)].

[15]W. W. Destler, H. S. Uhm, H. Kim, and M. P. Reiser, J. Appl. Phys. **50**, 3015 (1979).

[16]W. W Destler, P. G. O'Shea, J. Rodgers, and Z. Segalov, in *Proceedings of Particle Accelerator Conference, Washington, DC, March 16–19, 1987*, edited by E. R. Lundstrom and L. S. Taylor, p. 103.

[17]J. T. Cremer, Ph.D. thesis, University of Maryland, 1984.

Numerical simulation of collective ion acceleration in an intense electron beam–localized gas cloud system

R. L. Yao and C. D. Striffler

Laboratory for Plasma Research and Department of Electrical Engineering, University of Maryland, College Park, Maryland 20742

In experiments in which an intense relativistic electron beam is injected into an evacuated drift tube with a localized gas cloud located near the anode, ions with energies several times the electron beam energy have been observed. These experiments have been simulated using a particle-in-cell code which realistically models ionization of the gas. It was found that when the injected electron beam current exceeds the space-charge limiting current, ions are accelerated to energies several times the electron beam energy by coherent motion of the ions and the intense virtual cathode electric fields. The dependence of the peak ion energy on the system parameters as observed in the simulations is also discussed. For the parameter regimes investigated with beam energies up to 3 MV, beam currents up to 35 kA, gas pressures up to 600 mTorr, and gas cloud widths up to 6 cm, peak ion energies of 5–6 times the electron beam energy have been observed.

I. INTRODUCTION

Because the electric fields produced by an intense relativistic electron beam (IREB) are much larger than those that can be attained in conventional accelerators, considerable work has been devoted to using IREBs to accelerate ions to high energies. In 1970, Graybill and Uglum[1] reported that ions with peak energies of four times the electron beam energy were produced when an IREB was injected into a gas-filled drift tube. In 1973, Luce, Sahlin, and Crites[2] reported that ions with energies several times the electron beam energy were produced when an IREB was injected into an evacuated drift tube using a diode with a dielectric insert in the anode. Since these results were published, collective ion acceleration has been reported for many other systems, including those in which the ions are produced by beam ionization of dielectric drift tube walls[3] or by laser ionization of a solid target.[4]

Recently, Destler, Floyd, and Reiser[5] reported that in experiments performed at the University of Maryland collective ion acceleration was observed when an IREB was injected into an evacuated drift tube after gas had been puffed into the drift tube through a nozzle located near the anode. A diagram of the University of Maryland experiment is shown in Fig. 1. The system consists of a foilless electron beam diode, a grounded cylindrical drift tube, a nozzle located near the anode through which gas is puffed into the drift tube, and magnetic field coils, which produce a guide field for the electron beam. In a typical experiment, the drift tube is first pumped down to vacuum (5×10^{-5} Torr). The puff value connected to the nozzle is then fired, injecting neutral gas into the drift tube through the nozzle and producing a cloud of gas extending no more than a few cm from the anode. The diode is then fired, injecting the beam into the drift tube through the cloud of gas. Current collectors placed at the downstream end of the drift tube measure the ion current and stacked-foil neutron activation analysis is used to determine the ion energy and flux.

In the experiments, it was found that when the injected current I_0 exceeded the space-charge limiting current I_L for the system, ions were accelerated to energies several times the electron beam energy V_0. For example, using a 1.5-MeV, 35-kA electron beam, protons were accelerated to energies of greater than 8 MeV (5.3 V_0/nucleon) and xenon ions were accelerated to energies of greater than 638 MeV (4.9 V_0/nucleon).[6] It was also found that the maximum ion energy was essentially independent of the applied magnetic field.[7]

The space-charge limiting current for a system is the maximum current that can be propagated through the system before the potential depression produced by the space-charge exceeds the beam energy. When the injected current exceeds the space-charge limiting current, a virtual cathode forms where the potential equals the beam energy. The fraction of the injected current which exceeds the space-charge limiting current is reflected by the virtual cathode back through the anode or deflected to the drift tube wall. For a solid beam of radius R_b in a cylindrical drift tube of radius R_w with a large focusing magnetic field, the space-charge limiting current is given by the formula[8]

$$I_L = \frac{17\,000(\gamma_0^{2/3} - 1)^{3/2}}{1 + 2\ln(R_w/R_b)} \quad \text{(Amps)}, \qquad (1)$$

where γ_0 is the Lorentz factor for the injected electrons and where it is assumed that $R_b \ll R_w$.

Many explanations have been offered for collective acceleration in both gas-filled systems and evacuated systems. Among the first models to be proposed for collective ion acceleration in a gas-filled drift tube was that of Olson.[9] According to this model, which is based on work by Poukey and Rostoker,[10] collective ion acceleration occurs only when the current exceeds the space-charge limiting current. Soon after the electron beam is injected, the beam front stops near the anode, forming a stationary potential well with a depth of two to three times the electron beam energy. As the space charge near the anode is neutralized by ionization of the gas, the beam front and the potential well suddenly start to prop-
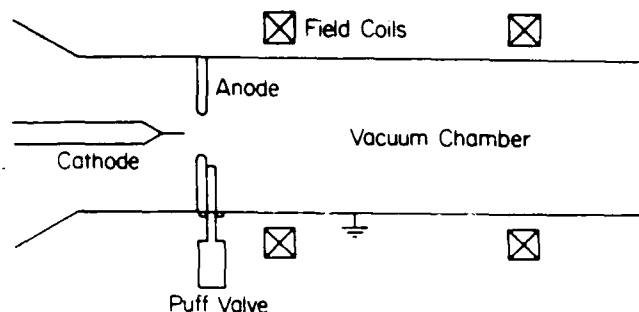
FIG. 1. Schematic of experimental setup for University of Maryland collective acceleration experiments.

agate downstream. Ions are accelerated by the deep, stationary potential well and by the moving potential well. This theory accounts for many of the experimental observations of collective ion acceleration in gas-filled systems and is consistent with some 2-D particle simulations of IREB injection into a neutral gas.[11]

The energies that are typically observed in evacuated systems such as the Luce diode configuration are much too high to be explained by the theory of Olson. Furthermore, Adier, Nation, and Serlin[12] have also reported detailed observations of collective ion acceleration in a Luce diode configuration which indicate that ion acceleration was not produced by a deep potential well or by a moving potential well at the beam front. They suggested instead that ions were accelerated by electrostatic waves which are driven by the two-stream instability. Destler et al.[4] suggested that in evacuated systems collective acceleration occurs by a bootstrap process. The early part of the beam pulse forms a dense plasma near the anode. If the beam current exceeds the space-charge limiting current and the plasma density is sufficiently high, a virtual cathode forms at the downstream edge of the plasma. The intense virtual cathode electric fields draw ions out of the plasma, the ions neutralize the electron beam space charge, and the virtual cathode moves further downstream. As this process is repeated, the beam electrons transfer momentum to the ions until the ions attain the same velocity as the beam-front electrons. A similar model was proposed earlier by Ryutov and Stupakov[13] for collective ion acceleration produced by injection of an IREB through a dense plasma layer. Mako and Tajima[14] modified the model using data obtained from experiments with a gas-filled drift tube, and were able to recover the experimentally measured peak ion energy (ten times the electron beam energy) and ion distribution. They also used a particle code to simulate injection of an IREB into an evacuated drift tube with a dense plasma layer located next to the injection plane. The simulations showed that the peak ion energies were limited by phase instability of the ions and the accelerating electric fields. However, using an artificially low ion mass, they also found that the peak ion energies never exceeded three times the electron beam energy and that, when the ion mass was doubled, the ion velocity decreased inversely as the square root of the mass. Using a 2-1/2-D electromagnetic particle code with a realistic ion mass, Faehl and Peter[15] and Peter et al.[16] simulated the same system and found that the virtual

cathode formed at the downstream edge of the plasma layer soon after the beam was injected and that no subsequent motion of the virtual cathode occurred. They also pointed out that no such motion should be expected because the maximum ion current that can be extracted from the plasma is never large enough to neutralize the electron beam space charge. They suggested that collective acceleration is the result of ambipolar expansion of the plasma rather than motion of the virtual cathode.

In simulations of injection of an IREB from a plasma into free space, Chang and Reiser[17] found that as ions were extracted from the surface of the plasma by the virtual cathode electric fields, the location of the virtual cathode minimum shifted downstream from its initial location. They also observed ions which had been accelerated to energies approximately twice the electron beam energy and proposed that the coherent motion of the virtual cathode and the ions as the virtual cathode shifts downstream to its final position was responsible for accelerating the ions.

In this paper we present a detailed picture of the acceleration mechanism in the University of Maryland experiments, in which an intense relativistic electron beam is injected into an evacuated drift tube with a localized gas cloud located near the anode. We have obtained this picture using particle-in-cell (PIC) code simulations which realistically model ionization of the neutral gas.

Our simulations differ from previous simulations of collective acceleration in the following respects. In our simulations, an IREB is injected into an evacuated drift tube with a well-localized gas cloud located next to the anode, as opposed to a gas-filled drift tube or an evacuated drift tube with a plasma layer located next to the anode. Ions are produced in the drift tube by realistically modeling ionization of the gas by impact ionization, as opposed to assuming an initial distribution of ions or injecting ions. Realistic ion masses are also used. The finite radius of the beam is also taken into account, so that the simulations are more realistic than strictly 1-D simulations. Finally, the IREB is injected into a grounded drift tube rather than free space so that inductive effects can confidently be neglected. (We also note that our code is simple enough to permit a detailed investigation of the acceleration mechanism.)

In our simulations, we find that when the injected electron current exceeds the space-charge limiting current, a virtual cathode forms near the anode plane soon after the beam is injected. Neutralization of the electron beam space charge by impact ionization of the neutral gas then causes the virtual cathode to move downstream to the end of the gas region, where the virtual cathode stops. As the virtual cathode moves through the gas, ions are accelerated to energies several times the electron beam energy by the coherent motion of the ions and the intense virtual cathode electric fields. (This picture is similar to the mechanism observed by Chang and Reiser.)

Before proceeding, we would like to point out that the general features of the above picture are similar to results which have been obtained earlier at the University of Maryland.[18] The present work has also been extended to simulate enhanced collective ion acceleration in a laser-controlled

collective accelerator.[19] Applications of the system to intense beam propagation are summarized elsewhere.[20]

In the following sections, we first describe the computer code which we have written to simulate collective ion acceleration in an intense electron beam–localized gas cloud system. We then discuss the acceleration mechanism which we observe in the simulations. Finally, we discuss the dependence of the peak ion energy on the system parameters.

II. DESCRIPTION OF COMPUTER CODE

In our simulations, a beam of current I_0, energy V_0, and radius R_b is injected into a grounded cylindrical drift tube of length d and radius R_w along the axis of the drift tube. A schematic of the model is shown in Fig. 2. The region of the drift tube extending from the anode to a distance z_0 downstream is filled by neutral hydrogen at a constant pressure p_0. The electron beam is assumed to be focused by an infinitely strong guide magnetic field, so that particles in the simulation move only along the axis of the drift tube. The beam radius is also assumed to be much smaller than the wall radius so that the charge and current density and the axial electric field are approximately uniform across the beam cross-section.

The macroparticles in the simulation obey the relativistic equations of motion

$$\frac{du}{dt} = \frac{q}{m} E_z, \tag{2}$$

$$\frac{dz}{dt} = v, \tag{3}$$

where z is the axial position of the center of the macroparticle, u is the four-velocity of the macroparticle, $v = u/\sqrt{1 + (u/c)^2}$, q is the charge and m is the mass of the macroparticle, and E_z is the electric field on the axis of the drift tube at z. The code integrates the equations of motion forward in time using a leapfrog scheme.

The electric field E_z on axis computed by first computing the potential ϕ on axis and then numerically computing the derivative $E_z = -\partial\phi/\partial z$. The potential ϕ is computed by finite differencing Poisson's equation in z, taking the finite sine transform of the finite-differenced equation, analytically solving the resulting system of ordinary differential equations in r, and taking the inverse finite sine transform.

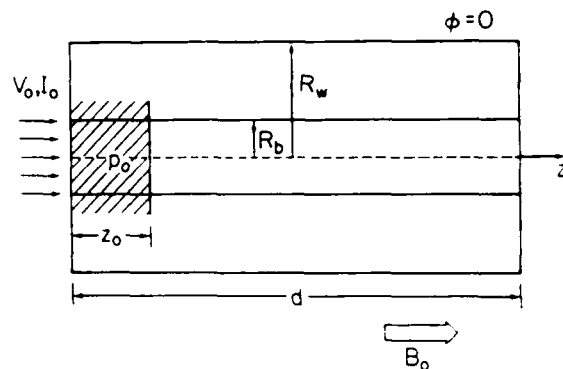Ionization of the neutral gas is modeled by monitoring

FIG. 2. Schematic of simulation model.

the amount of ionization in each grid cell that is produced by impact ionization. When the total number of ions produced in a grid cell exceeds the number of ions in an ion macroparticle, an ion macroparticle and an electron macroparticle are created at the center of the grid cell. The total ionization produced in a grid cell in one time step is computed using the formula

$$\Delta N = \Sigma_i N_i S_i (KE_i) v_i p_0 \Delta t, \tag{4}$$

where the sum is taken over all macroparticles in the grid cell, N_i is the number of real particles in the ith macroparticle, S_i is the ionization cross section in events/m/Torr for each particle in the ith macroparticle, KE_i is the kinetic energy of each particle in the ith macroparticle, v_i is the velocity of the macroparticle in m/s, p_0 is the pressure of the neutral gas in Torr at the center of the grid cell, and Δt is the time step in seconds. The ionization cross sections S_i used in the simulation are piecewise-linear approximations of published ionization cross sections for molecular hydrogen.[9] In units of events/cm/Torr, the cross section for electron impact ionization used in the simulation is given by

$$S_e = \begin{cases} 0, & KE < 20 \text{ eV}, \\ \sqrt{10}, & 20 \text{ eV} < KE < \sqrt{10} \times 10^2 \text{ eV}, \\ 10^3/KE, & \sqrt{10} \times 10^2 \text{ eV} < KE < 10^5 \text{ eV}, \\ 10^{-2}, & 10^5 \text{ eV} < KE. \end{cases}$$

where KE is the electron kinetic energy in eV. The cross section for proton impact ionization used in the simulation is given by

$$S_i = \begin{cases} 0, & KE < 10 \text{ eV}, \\ \exp(2.383 \log_{10} KE - 8.577), & 10 \text{ eV} < KE < 4.3 \times 10^4 \text{ eV}, \\ \exp(-1.839 \log_{10} KE + 11.036), & 4.3 \times 10^4 \text{ eV} < KE. \end{cases}$$

where KE is the proton kinetic energy in eV.

In the simulations, we chose to run at currents less than 35 kA, and gas cloud pressures less than 600 mTorr because we found that at high currents and high pressures and long pulse lengths, the number of particles in the simulation became too large.

Finally, we note that when no gas is present the current

that is observed downstream agrees with the limiting current formula Eq. (1).

III. PICTURE OF COLLECTIVE ACCELERATION MECHANISM

We have run the code for many different values of the electron beam current, electron beam energy, drift tube radi-

us, drift tube length, neutral gas pressure, and gas cloud width. We present a picture of the collective acceleration mechanism that we have observed in all of the simulations in which collective acceleration occurred. To do so, we will use the results of a single simulation. (We note that the parameter values differ from typical parameter values in the University of Maryland experiments. However, simulations performed with the experimental parameter values show that the acceleration mechanism is the same as described here.)

In the simulation, a 15-kA, 500-keV, 0.5-cm-radius electron beam is injected into a 4-cm-radius, 40-cm-long drift tube with a 1-cm-wide, 450-mTorr hydrogen cloud located next to the anode plane. The beam current and beam energy are assumed to rise instantaneously. According to Eq. (1), the space-charge limiting current for the system is approximately 1.4 kA. The time step is approximately 0.75 ps and the grid cell width is approximately 0.2 mm.

Figure 3 shows the time-integrated proton energy spectrum 7.5 cm from the anode plane 11 ns after the start of the run. The energy spectrum can be roughly divided into two parts—the bulk of the spectrum, which is centered about 0.6 MeV, and a tail that extends out to 1.5 MeV (three times the electron beam energy). We ignore the ions in the bulk of the spectrum and focus on the ions in the high-energy tail. Note that since the potential depression at the center of the drift tube is approximately -500 kV, the ion spectrum that would be observed by a grounded detector would be the same as the spectrum shown in Fig. 3 shifted to the left by 0.5 MeV. In the following, we present a detailed picture showing how the ions in the high-energy tail are accelerated to energies exceeding the electron beam energy.

In Fig. 4, the potential ϕ on axis near the anode plane is pictured as a function of distance z from the anode plane at several different time steps. About 40 ps after the start of the run, a virtual cathode forms about 2 mm from the anode plane, and the current measured downstream from the virtual cathode falls to a value approximately equal to the space-charge limiting current. After formation of the virtual cathode, the potential remains essentially the same for several thousand time steps (the position and amplitude of the virtual cathode oscillate in time at the local plasma frequen-
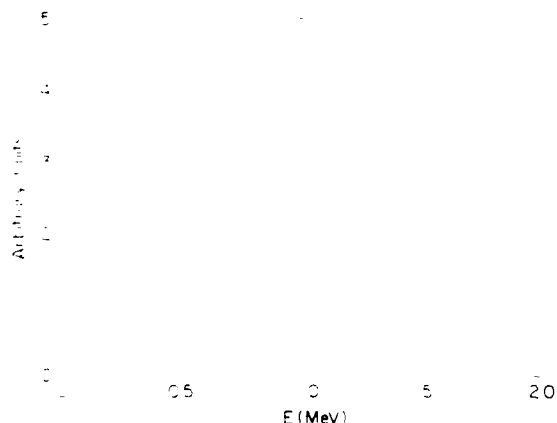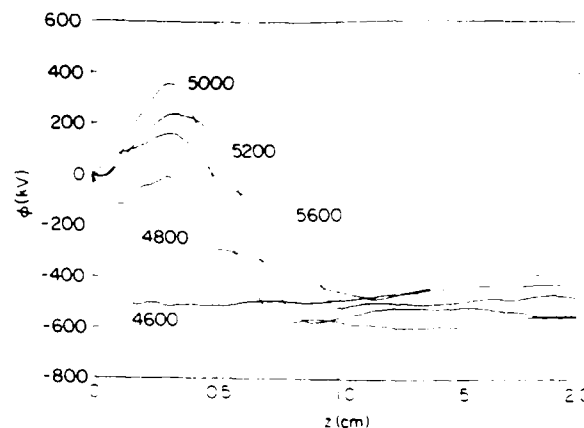

FIG. 4. Potential on axis ϕ near anode plane vs distance from anode plane z for time steps 4600, 4800, 5000, 5200, and 5600 during acceleration phase. Note that 1000 time steps equals about 0.75 ns. See Fig. 3 for system parameters.

cy, but the time-averaged position and amplitude are approximately the same). The potential for time step 4600, which is shown in Fig. 4, is typical for this stage. During this stage, the beam electrons ionize the neutral gas, producing a plasma in the vicinity of the virtual cathode. The intense electric fields near the virtual cathode quickly expel the plasma electrons from the plasma region. The plasma ions are also accelerated by these electric fields but leave the plasma region at a much slower rate than the plasma electrons. They also tend to be accelerated downstream, whereas the plasma electrons tend to be accelerated upstream, where they exit from the drift tube through the anode plane. As plasma ions drift through the gas, they also contribute to the ionization. As the ion density in the plasma region increases, the virtual cathode moves downstream to the end of the plasma region leaving behind a positive potential region (time steps 4600–5000). Ions lying to the left of the peak of the positive potential are accelerated upstream and exit the drift tube through the anode plane. Ions lying to the right of the peak of the positive potential are accelerated downstream. As the ions move downstream, the virtual cathode also moves downstream with the positive potential region widening and extending downstream behind it (time steps 5000–5600). The virtual cathode ceases to move when it reaches the end of the gas region at $z = 1$ cm (time step 5600). We will see that ions are accelerated to energies of nearly 1.5 MeV during the time that the virtual cathode and the positive potential region move downstream.

The formation of a positive potential region has been observed experimentally and in other simulations.[14] The reason the potential in the plasma region becomes positive can be understood as follows. Because the electron impact ionization cross section peaks at low energies, the majority of ions are formed near the virtual cathode. The buildup of ions in the vicinity of the virtual cathode causes the beam electrons to spend more time there, and as a result the electron density downstream from the virtual cathode decreases. Hence, when the ion density is sufficiently high, the position of the virtual cathode can no longer be maintained and the virtual cathode begins to move downstream. (In fact, our

FIG. 3. Time-integrated proton energy spectrum at $z = 7.5$ cm after 11 ns. The run parameters are $I_b = 15$ kA, $V_b = 500$ keV, $R_b = 0.5$ cm, $R_d = 4$ cm, $d = 40$ cm, $p_0 = 450$ mTorr, and $z_0 = 1$ cm
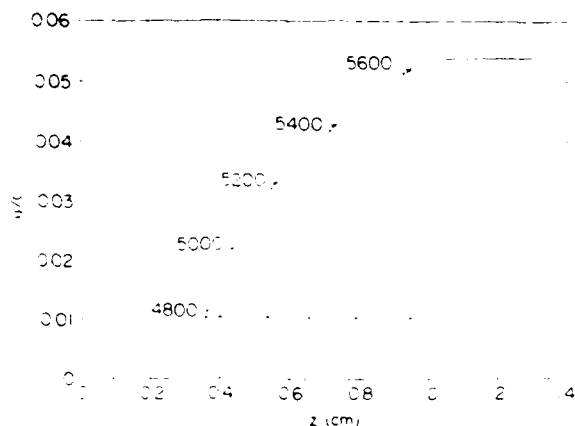
FIG. 5. Phase-space trajectory of collectively accelerated proton. The boxes plotted along the trajectory indicate the location of the ion at equally spaced time steps during the acceleration phase. The diamonds plotted along the base of the trajectory indicate the location of the peak electric field at the same time steps. See Fig. 3 for system parameters.

simulations show that immediately preceding the onset of the acceleration process, the electron current measured immediately downstream from the plasma region falls abruptly.) As the virtual cathode moves through the plasma region, the electrons behind the virtual cathode travel through the plasma with essentially the same speed with which they are injected. The increase in the speed of the electrons through the plasma region produces a sudden drop in the electron density. Hence, the virtual cathode leaves a net positive space charge in its wake and the potential becomes positive in the plasma region.

In Fig. 5, the phase-space trajectory of a collectively accelerated proton is shown during the collective acceleration process. The ion is created with zero velocity at a distance of about 1.3 mm from the anode plane about 2.6 ns after the start of the run (time step 3500). It is rapidly accelerated by the electric field near the virtual cathode to a velocity of about $0.008c$ (corresponding to an energy of 30 keV) and begins to drift downstream. When it has drifted about 2 mm downstream, the potential begins to go positive (at around time step 4700) and the virtual cathode begins to move downstream. As the virtual cathode moves downstream and the positive region extends downstream behind it (time steps 4800–5600), the proton is rapidly accelerated to a final velocity of about $0.054c$ (corresponding to an energy of 1.4 MeV).

The boxes plotted along the proton phase-space trajectory indicate points along the trajectory which are separated by equal time intervals of 200 time steps or about 150 ps. Each box is labeled with the corresponding time step starting with time step 4800. Below the phase-space trajectory, we have also plotted the location of the peak electric field at the same time steps. The peak electric field is always located in the region where the potential drops sharply from the edge of the positive potential region to the virtual cathode. As the virtual cathode moves downstream and the positive potential region extends downstream behind the virtual cathode the peak electric field also moves downstream. As can be seen from the figure, the ion follows closely behind the peak

electric field for time steps 4800 to 5600. It is this coherent motion of the ion and the peak electric field through the plasma region which enables the ion to be accelerated to energies several times the energy it would gain if the potential were stationary.

Note that the trajectory of the proton in Fig. 5 is similar to the trajectory of an ion being accelerated by a constant electric field $v_z(z) = \sqrt{v_{z0}^2 + 2(eE_z/m_p)z}$, where v_{z0} is the initial ion velocity. Using values obtained from the figure in the above formula, we find that the electric field E_z is about 200 MV/m, which is near the peak virtual cathode electric field of 250 MV/m.

The reason for the coherent motion of the ion and the peak electric field during the motion of the potential front can be understood by considering the free expansion of a slab of ions, which initially has uniform density. As the slab expands, an ion at the surface of the slab always feels the same electric field, that is, the ion and the electric field travel at the same velocity. We believe that the same effect occurs during motion of the potential front. In the simulations, the ions at the front of the accelerated ion beam are accelerated not only by the space charge produced by the ions following behind but also by the electric field produced by the virtual cathode which always moves in front of the ion beam—the ions are pushed ahead by the ions which follow and simultaneously pulled ahead by the virtual cathode.

The reason the potential front stops moving at the end of the gas region can also be understood by considering the free expansion of a slab of ions. As the slab expands, the ion density and the potential decrease uniformly. In the gas region, ionization of the gas, particularly by ions, can supply ions at a rate sufficiently high to prevent total collapse of the potential and reformation of a virtual cathode near the anode. Beyond the gas region, no ions are produced and the ion density is too low to permit the virtual cathode to move forward. (As Faehl and Peter[15] observed, the maximum ion current which can be extracted from the plasma is space-charge limited and hence ions can never be extracted at a rate sufficient to significantly neutralize the electron beam space charge downstream.)

Although all of the collectively accelerated ions are accelerated by the moving potential front, some ions continue to accelerate, although at a much lower rate, after they have left the gas region. This additional acceleration is probably produced by the interaction of the collectively accelerated ions among themselves—interactions between ions that have been collectively accelerated in a bunch will cause ions with velocities greater than the mean velocity to be accelerated and ions with velocities less than the mean velocity to be decelerated.

Several bursts of accelerated ions, which follow one another at short intervals, are often observed in simulations. The multiple bursts are produced when the positive potential region collapses after the ions have been accelerated out of the gas region. the virtual cathode retreats to a location inside the gas region and the acceleration process repeats itself. If the pressure is increased, with all other system parameters kept constant, the multiple bursts are suppressed, probably because the rate of ion production in the gas region is suffi-

cient to prevent collapse of the positive potential region. Such multiple bursts have been observed in some experiments in evacuated systems.[12]

IV. RESULTS OF PARAMETER STUDIES

A. Dependence on beam energy and current

In Fig. 6, the peak proton energy E_{max} measured at $z = 7.5$ cm in the first 10 ns of the run is plotted as a function of the injected beam current I_0 for beam energies V_0 of 0.5, 1.0, 1.5, and 3.0 MeV. In each case, the gas pressure is 600 mTorr and the gas cloud width is 1 cm. Generally, E_{max} increases with beam current and beam energy. In Fig. 7, the same data are plotted with E_{max} normalized to V_0 and I_0 normalized to the space-charge limiting current I_L, given by Eq. (1). Notice that all the plotted points lie on approximately the same curve. For all values of V_0 which were used, no collectively accelerated protons are observed for $I_0/I_L < 1$. As I_0/I_L increases above unity, E_{max} increases sharply and then continues to increase but at a much slower rate. (Note that for fixed I_0, the ratio $/I_L$ decreases with increasing V_0. Hence for the same current I_0, the ratio E_{max}/V_0 with $V_0 = 0.5$ MeV is much larger than the ratio for $V_0 = 3$ MeV.)

The observed dependence of the peak proton energy on beam energy and current can be understood quite simply by recalling that the strength of the peak electric field increases with V_0 and I_0/I_L. In Fig. 8(a), the phase-space trajectories of collectively accelerated protons are shown for three different values of the injected current—10, 20, and 30 kA—and the same beam energy of 0.5 MeV. In each case, the gas pressure is 600 mTorr and the gas cloud width is 1 cm. Recalling that the accelerating electric field is approximately proportional to the product of the velocity and the slope du/dz of the trajectory, it can be seen that as the current increases so does the accelerating electric field. In Fig. 8(b), the phase-space trajectories of collectively   elerated protons are shown for three different values of the beam energy—0.5, 1.0, and 1.5 MeV—and the same beam current of 30 kA. It can be seen that as the beam energy increases so
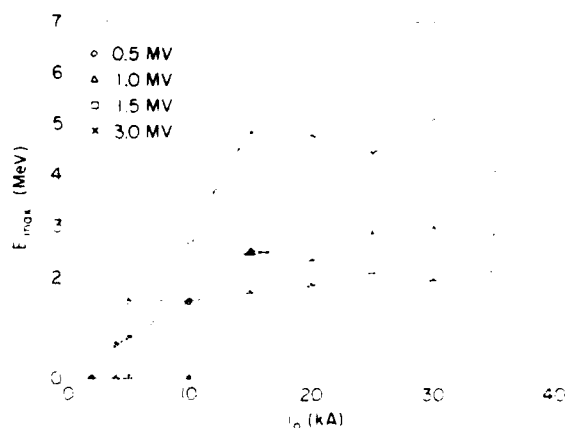
does the accelerating electric field. (This dependence is not so clear when the trajectories for 0.5 and 1.0 MeV are compared, which illustrates the complex nature of the acceleration process, that is, the final ion energy depends not only on the strength of the electric field but also on the location and velocity of the ion when the virtual cathode begins to move downstream and on the velocity with which the virtual cathode moves.)
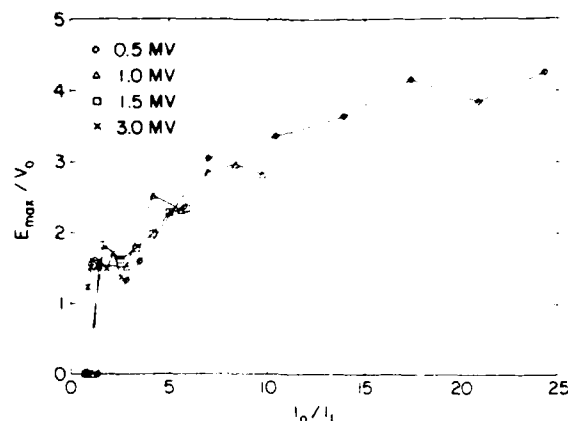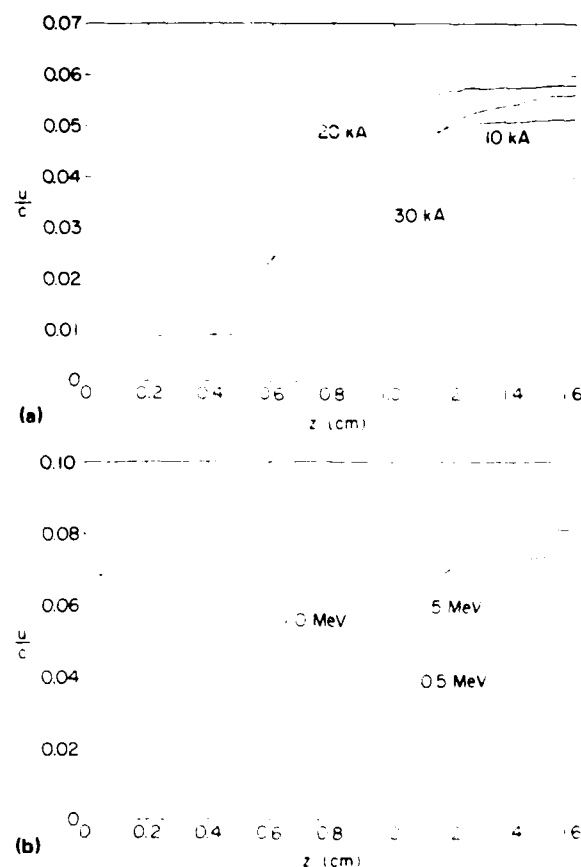

FIG. 7. Peak proton energy E_{max} normalized to beam energy V_0 vs injected current I_0 normalized to space-charge limiting current I_L. See Figs. 3 and 6 for system parameters.

FIG. 6. Peak proton energy E_{max} measured at $z = 7.5$ cm in the first 10 ns vs injected current I_0 for $p_0 = 600$ mTorr, $z_0 = 1$ cm, and $V_0 = 0.5$, 1.0, 1.5, and 3.0 MeV. See Fig. 3 for system parameters.

FIG. 8. Phase-space trajectories of collectively accelerated protons for (a) $V_0 = 0.5$ MeV and $I_0 = 10$, 20, and 30 kA, and for (b) $I_0 = 30$ kA and $V_0 = 0.5$, 1.0, and 1.5 MeV. See Fig. 3 for other system parameters.
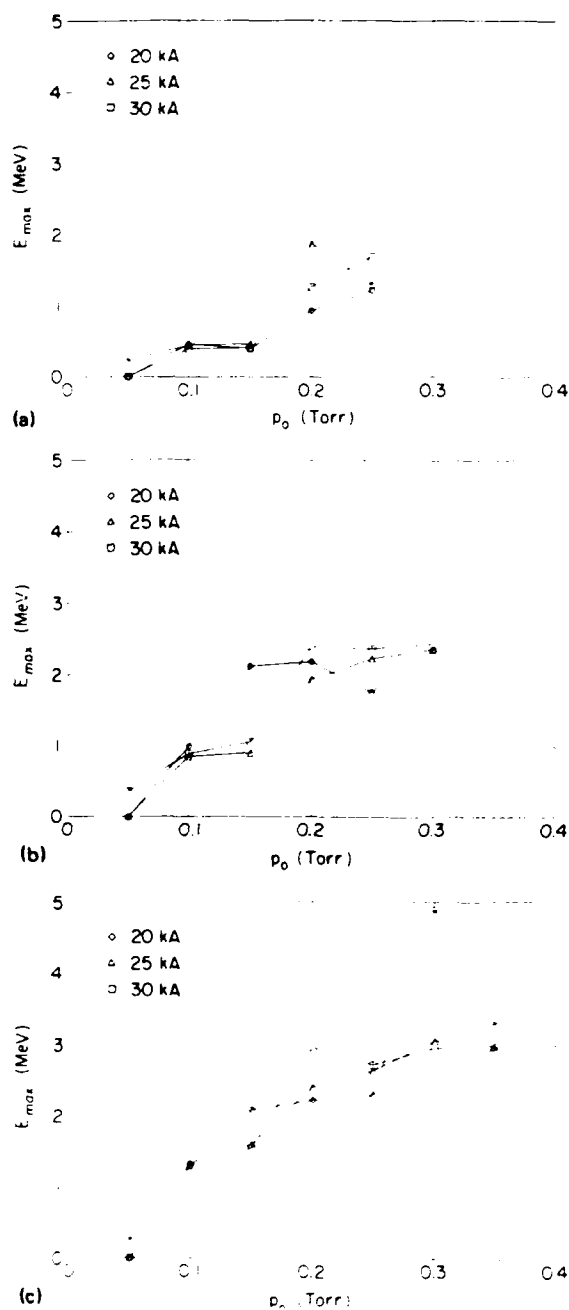
FIG 9 Peak proton energy E_{max} measured at $z = 7.5$ cm after 20 ns vs gas pressure p_0 for $z = 1$ cm and $V_0 = $ (a) 0.5, (b) 1.0, and (c) 1.5 MeV. See Fig 3 for other system parameters

B. Dependence on gas cloud pressure

In Fig. 9, the peak proton energy E_{max} measured at $z = 7.5$ cm in the first 20 ns of the beam pulse is plotted as a function of gas pressure p_0 for injected beam currents I_0 of 20, 25, and 30 kA and for beam energies V_0 of (a) 0.5, (b) 1.0, and (c) 1.5 MeV. In each case, the gas cloud width is 1.0 cm. At 50 mTorr, no collectively accelerated protons are observed in the first 20 ns of the beam pulse. Above 50 mTorr, E_{max} tends to increase with increasing pressure and level off at energies several times the electron beam energy. Generally, the higher the beam energy, the higher the energy and pressure at which the energy levels off.

The observed dependence of the peak proton energy on the pressure can be explained qualitatively as follows. At low pressures, the amount of ionization at the end of 20 ns is too small to neutralize the electron beam space charge and the virtual cathode remains at its initial position; no collective acceleration occurs and the peak proton energies which are measured are less than the electron beam energy. As the pressure is increased, the amount of ionization which is produced during the beam pulse becomes large enough to neutralize the electron beam space charge and permit the virtual cathode to move downstream. As it moves downstream, the virtual cathode electric fields accelerate ions to energies several times the electron beam energy. Once the acceleration process has begun, the final energy of a collectively accelerated ion depends only on the magnitude of the accelerating electric field and the distance over which the ion travels coherently with the electric field. Now, the magnitude of the electric field will be determined mainly by the electron beam energy and current and the density of ions in the plasma region at the start of the acceleration process (because the electric field at the surface of a slab of ions is proportional to the ion density in the slab). But the ion density at the start of the acceleration process is independent of the pressure, because it is proportional to the electron beam density, which is determined by the electron beam energy and current only. The only effect of increasing the gas pressure will be to decrease the time required for the ion density to build up before the acceleration process begins (which is in fact observed in simulations). Hence, the peak ion energy will depend only weakly on the neutral gas pressure, once the gas pressure is sufficiently high to cause collective acceleration.

The above picture is somewhat too simplistic because the gas pressure also affects the motion of the virtual cathode electric fields through the gas cloud. Generally, as the pressure increases, the virtual cathode moves through the gas cloud more quickly and higher peak proton energies are observed because the virtual cathode electric fields are able to accelerate the protons over a longer distance.

Although the dependence of collective acceleration on pressure as observed in our simulations is consistent with the model for collective acceleration which we have presented above, it disagrees with the experimental results obtained at the University of Maryland. In particular, Floyd et al.[6] reported that when a 1.5-MeV, 35-kA, 30-ns beam pulse was injected into a 25-cm-diam drift tube with a well-localized gas cloud located near the anode, collective acceleration was observed only in a narrow pressure window. In our simulations, we observe no such pressure window. In particular, we observe collective acceleration at all pressures up to 1 Torr.

The disagreement may have the following causes. First, in our simulations we have neglected charge exchange between protons and H_2 molecules. Since the mean free path for charge exchange for protons in H_2 is approximately 1 cm at 100 mTorr at approximately 100 keV,[?] at pressures of a few 100 mTorr charge exchange probably prevents acceleration of protons to energies much greater than a few 100 keV. Second, in our simulations we have neglected sources of ionization such as photoionization and prepulse ionization which could produce sufficient ionization in the gas region

to prevent formation of a virtual cathode near the injection plane. In simulations of injection of an IREB into vacuum with a localized plasma located next to the injection plane,[15,16,21] it was found that for plasma densities comparable to or exceeding the beam density, the virtual cathode formed near the downstream edge of the plasma. Finally, the disagreement with the reported experiments may be the result of changes in the electron beam diode characteristics as the pressure is increased. In the experiments, the peak gas cloud pressure at the time of beam injection was varied by simply varying the time delay between firing of the gas puff valve and firing of the diode. It was also found that when the gas puff was fired too early, the diode shorted out.[4]
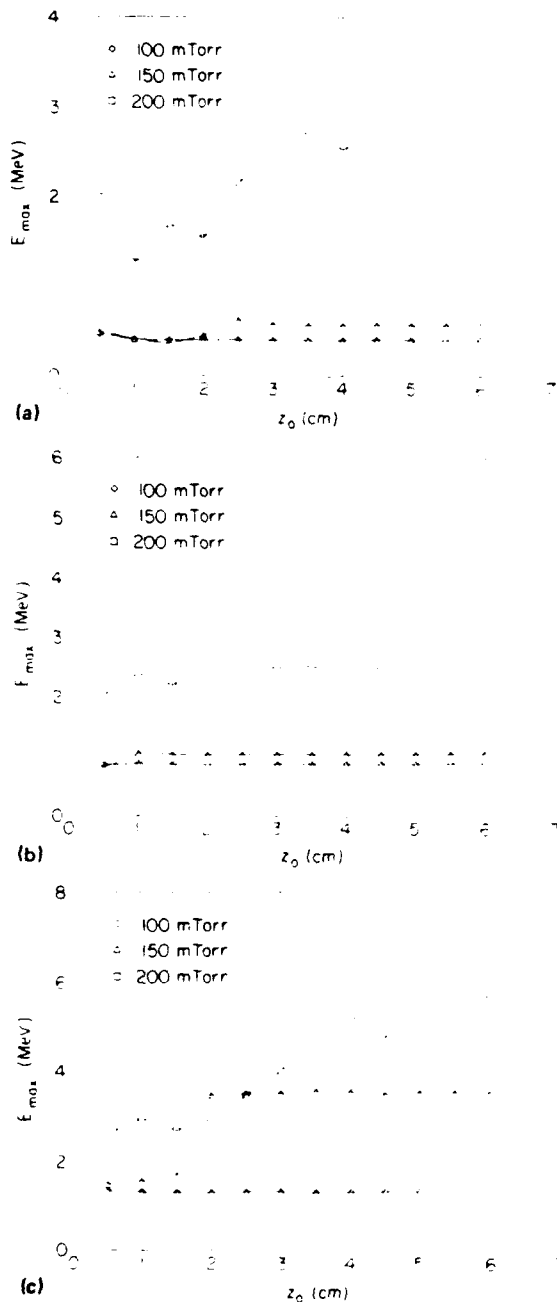
C. Dependence on gas cloud width

In Fig. 10, the peak proton energy E_{max} measured at $z = 7.5$ cm in the first 20 ns of the beam pulse is plotted as a function of gas cloud width z_0 for electron beam energies V_0 of (a) 0.5, (b) 1.0, and (c) 1.5 MeV and several neutral gas pressures p_0. In each case, the injected electron beam current is 30 kA.

Figure 10 shows that E_{max} tends to increase with gas cloud width and then level off, and that this tendency becomes more pronounced as the pressure increases. In Fig. 10(c), for example, which shows data obtained for $V_0 = 1.5$ MeV, E_{max} increases approximately linearly with increasing gas cloud width before leveling off at about 6.0 MeV at $z_0 = 5.0$ cm for $p_0 = 200$ mTorr. (When $p_0 = 100$ mTorr, no collectively accelerated protons are detected in the first 20 ns of the beam pulse.)

The tendency of E_{max} to increase with increasing gas cloud width is consistent with the simple picture of collective acceleration presented above. Protons are accelerated to higher energies as the gas cloud width is increased because they are accelerated over longer distances. This trend is more pronounced at higher pressures because, as noted in the last section, higher pressures enable the virtual cathode to move through the gas cloud more quickly. Closer examination of the simulation results shows that E_{max} tends to increase as the gas cloud width increases because the protons are indeed accelerated over longer distances. Figure 11 shows the phase-space trajectories of two collectively accelerated ions for the same beam energy and current (30 kA) and the same gas cloud pressure (200 mTorr) but different gas cloud widths. It is clear from the figure that one proton is accelerated to a higher energy because it is accelerated over a longer distance. The figure also illustrates the reason for the tendency of the peak proton energy to level off as the gas cloud width is increased—the ions tend to outrun the moving potential front as it moves through the gas cloud (seen in the 3-cm case).

Results of simulations performed with different values of the injected beam current I_0 indicate that the value at which E_{max} levels off also tends to increase with beam current, although the correlation is relatively weak. In Fig. 12,
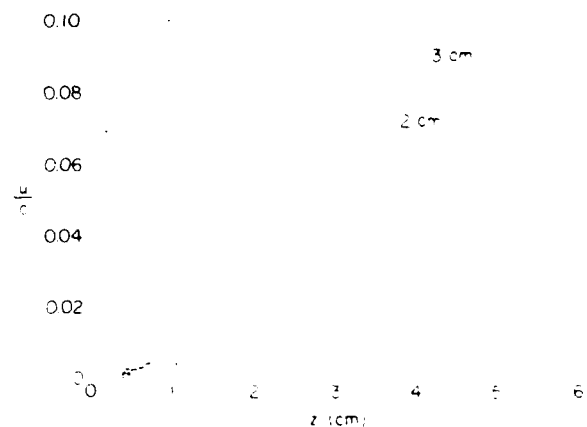

(a)

(b)

(c)

FIG. 10. Peak proton energy E_{max} measure at $z = 7.5$ cm after 20 ns vs gas cloud width z_0 for $I_0 = 30$ kA, $p_0 = 100$, 150, and 200 mTorr, and $V_0 = $ (a) 0.5, (b) 1.0, and (c) 1.5 MeV. See Fig. 3 for other system parameters.

FIG. 11. Phase-space trajectory of collectively accelerated proton for $V_0 = 1.5$ MeV, $I_0 = 30$ kA, $p_0 = 200$ mTorr, and $z_0 = 2$ and 3 cm. See Fig. 3 for other system parameters.
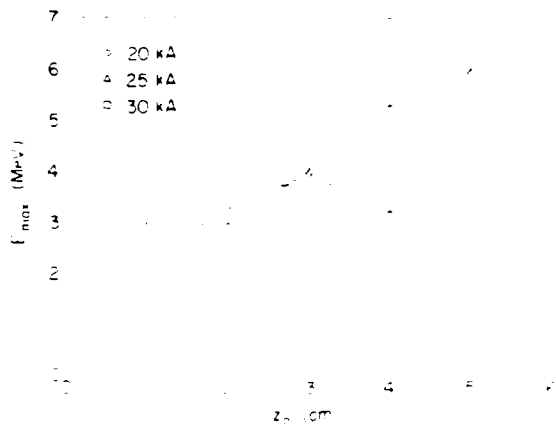
FIG. 12 Peak proton energy E_{max} measured at $z = 7.5$ cm after 20 ns vs gas cloud width z_0 for $V = 1.5$ MeV, $p_0 = 200$ mTorr, and $I_0 = 20$, 25, and 30 kA. See Fig. 3 for other system parameters.

for example, the peak proton energy measured at $z = 7.5$ cm in the first 20 ns of the beam pulse is plotted as a function of gas cloud width for a beam energy of 1.5 MeV, a gas pressure of 200 mTorr, and injected beam currents of 20, 25 and 30 kA.

V. SUMMARY

In order to investigate collective ion acceleration observed in experiments in which an intense relativistic electron-beam is injected into an evacuated drift tube with a localized gas cloud located near the anode, we have written a relativistic, electrostatic PIC code that realistically models ionization of the gas.

Using the code, we have developed a simple model for the collective acceleration mechanism in these experiments. In this model, ionization of the gas causes the virtual cathode to move downstream through the gas cloud. As the virtual cathode moves through the gas cloud, ions are accelerated to energies several times the electron-beam energy by coherent motion of the ions and the intense virtual cathode electric fields.

Using the code, we have also determined the dependence of the peak ion energy on the system parameters, including the beam energy V_0, beam current I_0, the gas cloud pressure p_0, and the gas cloud width z_0. We find that the peak energy E_{max} tends to increase with increasing values of beam energy V_0 and beam current I_0. In particular we find that E_{max}/V_0 tends to increase as I_0/I_f, where I_f is the space-charge limiting current given by Eq. (1), and that the functional dependence is nearly the same for a wide range of parameters. We also find that as the pressure is increased, E_{max} jumps from a value approximately equal to the beam energy to a value several times the beam energy, and that

generally, the higher the beam energy, the higher the pressure at which E_{max} reaches the final energy. We also find that, generally, E_{max} tends to increase with gas cloud width z_0 and then level off when z_0 is a few cm and that this tendency is more pronounced for higher pressures. Our results indicate that the mechanism for collective acceleration which we have observed in our simulations can produce protons with energies of at least 5–6 times the electron beam energy when the beam and the gas cloud properties are optimized.

ACKNOWLEDGMENTS

S. E. Graybill and J. R. Uglum, J. Appl. Phys. **41**, 236 (1970)

J. S. Luce, H. L. Sahlin, and T. R. Crites, IEEE Trans. Nucl. Sci. **NS-20**, 336 (1973)

A. Greenwald and R. Little, in *Collective Methods of Acceleration*, edited by N. Rostoker and M. Reiser (Harwood Academic, New York, 1979) p 371; J. A. Pasour, R. K. Parker, R. L. Gullickson, W. O. Doggett, and D. Pershing, *ibid.*, p 383; A. V. Agafonov, A. A. Kolomensky, E. G. Krastelev, A. N. Lebedev, and B. N. Yablokov, *ibid.*, p 395

W. W. Destler, H. S. Uhm, H. Kim, and M. Reiser, J. Appl. Phys. **50**, 3015 (1979)

W. W. Destler, L. E. Floyd, and M. Reiser, Phys. Rev. Lett. **44**, 70 (1980)

L. E. Floyd, W. W. Destler, M. Reiser, and H. M. Shin, J. Appl. Phys. **52**, 693 (1981)

L. E. Floyd and W. W. Destler, J. Appl. Phys. **57**, 1592 (1985)

L. S. Bogdankevich and A. A. Rukhadze, Sov. Phys. Usp. **14**, 163 (1971)

C. L. Olson and V. Schumacher, *Collective Ion Acceleration* (Springer, New York, 1979)

J. W. Poukey and N. Rostoker, Plasma Phys. **13**, 897 (1971)

J. W. Poukey and C. L. Olson, Phys. Rev. A **11**, 691 (1975)

R. Adler, J. A. Nation, and V. Serlin, Phys. Fluids **24**, 347, (1981)

D. D. Ryutov and G. V. Stupakov, Sov. J. Plasma Phys. **2**, 309 (1976)

F. Mako and T. Tajima, Phys. Fluids **27**, 1815 (1984)

R. J. Faehl and W. K. Peter, IEEE Trans. Nucl. Sci. **NS-32**, 3500 (1985)

W. Peter, R. J. Faehl, C. Snell, and M. E. Jones, IEEE Trans. Nucl. Sci. **NS-32**, 3506 (1985)

C. R. Chang and M. Reiser, J. Appl. Phys. **61**, 899 (1987)

J. M. Grossman, R. Kulkarni, C. D. Striffler, and R. J. Faehl, Proceedings of the Ninth Conference on Numerical Simulation of Plasmas, June 30–July 2, 1980, Northwestern University, Evanston, IL; J. M. Grossman, I. Mayergoyz, and C. D. Striffler, IEEE Trans. Nucl. Sci. **NS-28**, 2587 (1981); C. D. Striffler and H. Dantsker, Bull. Am. Phys. Soc. **27**, 983, 1982; H. Dantsker, L. E. Floyd, and C. D. Striffler, Bull. Am Phys. Soc. **29**, 1353 (1984)

R. L. Yao, W. W. Destler, C. D. Striffler, J. Rodgers, and Z. Segalov, Proceedings of the 1989 Particle Acceleration Conference, March 20–23, 1989, Chicago, IL

W. W. Destler, R. J. Faehl, M. Reiser, P. G. O'Shea, Z. Segalov, C. D. Striffler, and X. Zhang, Proceedings of the Sixth International Conference on High-Power Particle Beams, June 9–12, 1986, Kobe, Japan, p 215; W. W. Destler, J. Rodgers, Z. Segalov, C. D. Striffler, R. L. Yao, X. Zhang, and J. Guillory, Proceedings of the Seventh International Conference on High-Power Particle Beams, July 4–8, 1988, Karlsruhe, W Germany, p 185

M. Galvez and G. Gisler, Preprint LA-UR-88-1160, Los Alamos National Laboratories

1658   J. Appl. Phys., Vol. 67, No. 4, 15 February 1990

R. L. Yao and C. D. Striffler   1658

MEASUREMENTS AND SIMULATION OF CONTROLLED BEAMFRONT MOTION IN THE LASER CONTROLLED COLLECTIVE ACCELERATOR*

R.L. Yao, W.W. Destler, C.D. Striffler, J. Rodgers, Z. Segalov

University of Maryland, College Park, MD 20742

Abstract

In the Laser Controlled Collective Accelerator, an intense electron beam is injected at a current above the vacuum space charge limit into an initially evacuated drift tube. A plasma channel, produced by time-sequenced, multiple laser beam ionization of a solid target on the drift tube wall, provides the necessary neutralization to allow for effective beam propagation. By controlling the rate of production of the plasma channel as a function of time down the drift tube, control of the electron beamfront can be achieved. Recent experimental measurements of controlled beamfront motion in this configuration are presented, along with results of ion acceleration experiments conducted using two different accelerating gradients. These results are compared with numerical simulations of the system in which both controlled beamfront motion and ion acceleration is observed consistent with both design expectations and experimental results.

I. Introduction

The Laser Controlled Collective Accelerator concept[1-3] represents an attempt to extend the promising results from "naturally occurring" collective ion acceleration experiments to practical accelerators in which the accelerating gradient and distance can be systematically controlled. The concept is similar to that employed in the IFA-1 and IFA-2 experiments of Olson[4,5], although the actual experimental configuration is quite different. The basic concept behind the experiment is shown in Fig. 1. An intense relativistic electron beam is injected through a localized gas cloud into an evacuated drift tube at a current well above the vacuum space charge limit. A virtual cathode then forms immediately downstream of the injection point and ions produced within the localized gas cloud are accelerated to modest energies in a manner similar to more conventional collective accelerators. At this point, a channel of plasma is produced in a time sequenced manner down the drift tube by laser ionization of a CH_2 target strip located on the drift tube wall. The time sequencing of the plasma channel is achieved by dividing a Q-switched ruby laser pulse into ten approximately equal energy beams and using optical delays to ionize sequentially ten target spots equally spaced down the drift tube. In this manner, the virtual cathode at the beamfront can be carefully accelerated down the drift tube and ions trapped by the strong electric fields at the virtual cathode can be accelerated to high energies in a controlled manner.

In this paper we present in section II results of experiments in which controlled beamfront motion has been confirmed for two different accelerating gradients. Results of ion acceleration experiments are also presented. Numerical simulations of the experiments presented in section III confirm both controlled beamfront motion and the controlled acceleration of ions by the moving virtual cathode over significant distances. Conclusions are drawn in section IV.

II. Experiments

As shown in Fig. 1, an intense relativistic electron beam (900 keV, 20 kA, 30 ns) is emitted from a 4 mm diameter tungsten cathode located 1 cm upstream of a stainless steel anode. A 14 mm diameter hole in the anode plate on axis allows most all of the beam current to pass into a downstream drift tube 10 cm in diameter. Seed protons for acceleration are provided by beam ionization of a localized gas cloud produced a fast gas puff valve. The Q-switched ruby laser pulse (0.1 ns) is divided into ten approximately equal energy beams optically delayed to provide a time-sequenced source of p down the 50 cm length of the drift tube. Design consideration for the experiment and results of tests of the optical system have been reported previously.[2,3]

Five current collecting wall probes were installed to measure beam current deflected to the drift tube wall at the beamfront as a function of time. These probes were located at axial positions 10, 20, 30, 40, and 50 cm downstream of the anode plane. Total current reaching the downstream end of the drift tube was measured using a Faraday cup, and accelerated energies were measured using stacked foil activation technique. Titanium ($Ti^{47}(p,n)V^{47}$) and Copper ($Cu^{65}(p,n)Zn^{65}$) reactions were used having threshold energies of 3.7 and 4.2 MeV respectively. A silver activation neutron counter recorded neutrons produced by these reactions and by accelerated protons striking the drift tube walls.

Experimental data has been obtained for two different accelerating gradients; one at 40 MeV/m over a 50 cm accelerating distance and one at 90 MeV/m over the same distance. Data from the five wall current probes for the smaller current are shown in Fig. 2 for a) the case when the laser is fired 200 ns in advance of the beam, b) the case where the laser is not fired at all, and c) the case where the laser timing is such that the plasma is produced by laser-target interactions at the same time as the beam is being injected (optimal timing). As can be readily seen from these results, good control over beamfront motion has been achieved when the laser timing is optimal. Measurements of the accelerated ion energy and propagated current, shown in Fig. 3, clearly show that protons can be accelerated up to the designed output energy when laser-beam timing is such as to allow control of the beamfront.

Experimental data obtained at the higher accelerating gradient of 90 MV/m also indicate good control over the beamfront motion, but peak ion energies observed are actually less than those observed for the lower gradient experiments. This is undoubtedly due to a reduction in the electric field strength at the virtual cathode below 90 MV/m at some point in the acceleration process. The following results of numerical simulations of the experiments shed additional light on this result.

III. Numerical Simulations

A particle-in-cell code was used to simulate the laser controlled acceleration experiments. In the simulations, the beam is assumed to be focussed by an infinitely strong magnetic field so that the particles move only along the axis

the drift tube. The radius of the beam is also assumed to be much less than the radius of the drift tube so that the charge density, current density, and axial electrical field are approximately constant across the beam cross-section. Ionization of the neutral gas is modelled by keeping track of the amount of ionization produced by collisions with electrons and ions and introducing electrons and ions appropriately.

In the simulations, the laser-produced plasma is assumed to completely neutralize the space-charge on the axis of the drift tube once it reaches the electron beam from the wall. The time required for the laser-produced plasma to reach the electron beam from the wall is assumed to be given by the time required for a proton to fall through a logarithmic potential drop V_0 from $r = R_w$ to $r = R_b$, where V_0 is the electron beam voltage, R_w is the wall radius and R_b is the beam radius.

Results are shown for a 900-kV, 20-kA, 1-cm-radius electron beam which is injected into a 5-cm-radius, 50-cm-long drift tube with a 2-cm-wide, 100-mTorr hydrogen gas cloud located next to the anode plane. The front of the laser beam is assumed to travel down the drift tube at a velocity which increases linearly from $\beta_i = 0.04$ to $\beta_f = 0.2$ over a distance of 45 cm, corresponding to an accelerating gradient of 40 MeV/m.

Figure 4 shows the peak proton energy measured at 45 cm versus the time delay between the start of the laser pulse and the start of the beam pulse $\tau_L - \tau_B$. In plotting this data, we assumed that the laser requires 10 ns to produce plasma after striking the target on the wall. For a wide range of $\tau_L - \tau_B$, the peak proton energy which was measured actually exceeds the design value of 18.76 MeV.

Figure 5 shows the velocity versus position for an accelerated proton for $\tau_L - \tau_B = -8$ ns. Also shown in the figure is the velocity versus position for the front of the laser beam. The proton is accelerated relatively smoothly from an initial velocity of 0.04c to a final velocity of 0.2c.

In all runs the peak electric field E_z fell by an order of magnitude, e.g. from 3×10^8 V/m to 5×10^7 V/m, as the beam front moved downstream. Figure 6 shows the magnitude versus location of the peak E_z at a number of time steps approximately 2 ns apart for one run. The decrease in the strength of the peak electric field observed in the simulations is consistent with the experimental observation that the peak ion energy actually fell when a higher accelerating gradient was used.

IV. Conclusions

In conclusion, both experiments and numerical simulations now indicate that the laser-controlled collective accelerator concept is a promising one. Effective control over the propagation of a virtual cathode at the front of an intense relativistic electron beam has been achieved, and protons have been accelerated at a rate of 40 MV/m over a distance of about 50 cm. Furthermore, numerical simulations indicate that significantly higher ion energies can be achieved by either using longer accelerating distances (and consequently, longer injected electron beam pulse durations) and/or by injecting higher energy electron beams to maintain higher electric field strengths at the virtual cathode.

References

1. P.G. O'Shea, W.W. Destler, J. Rodgers, and Z. Segalov, Appl. Phys. Lett. 49, 1696 (1986)

2. W.W. Destler, P.G. O'Shea, J. Rodgers, and Z. Segalov, Proc. Particle Accelerator Conference, Washington DC,

March 16-19, 1987, p. 103.

3. W.W. Destler, J. Rodgers, and Z. Segalov, submitted to J. Appl. Phys., Feb. 1989.

4. C.L. Olson and U. Schumacher, in Springer Tracts in Modern Physics: Collective Ion Acceleration, edited by G. Hobler (Springer, New York, 1979), Vol. 84.

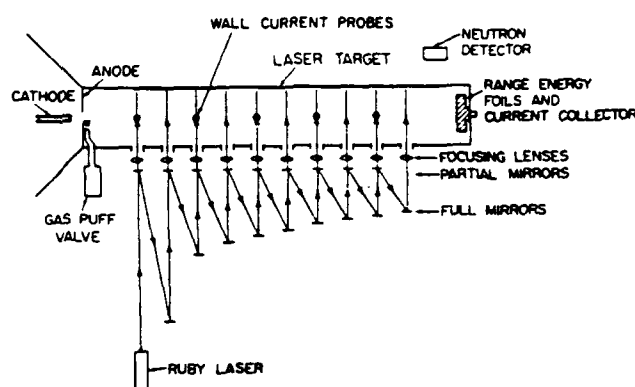5. C.L. Olson, C.A. Front, E.L. Patterson, J.P. Anthes, and J.W. Poukey, Phys. Rev. Lett. 56, 2260 (1986).
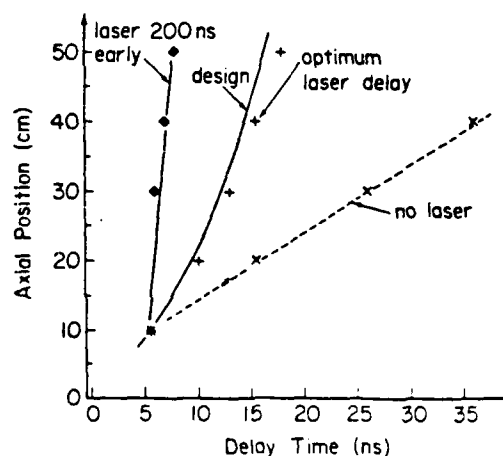
Fig. 1. Experimental Configuration.

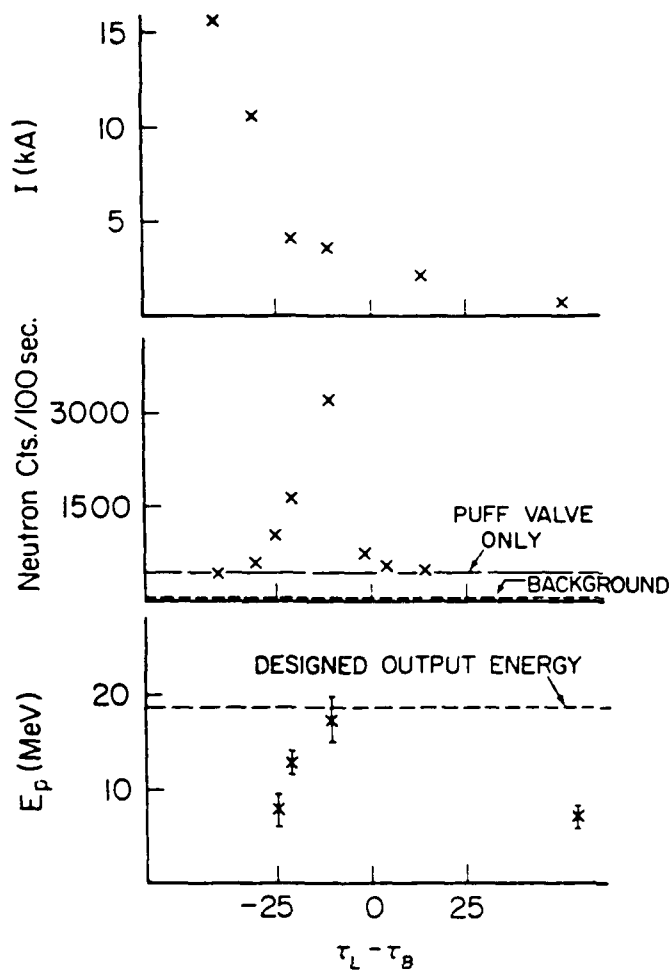Fig. 2. Data from 5 axially spaced current collectors located on drift tube wall.

Fig. 5. Velocity vs. position for accelerated proton.

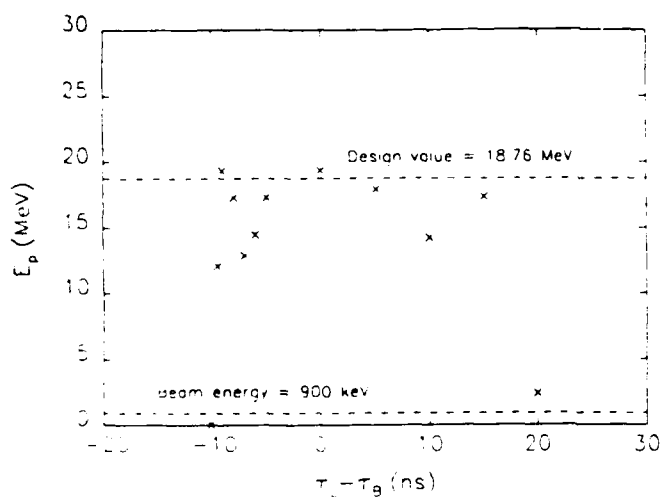Fig. 3. Propagated current at 50 cm. neutron counts, and peak proton energy vs. beam-laser firing delay.
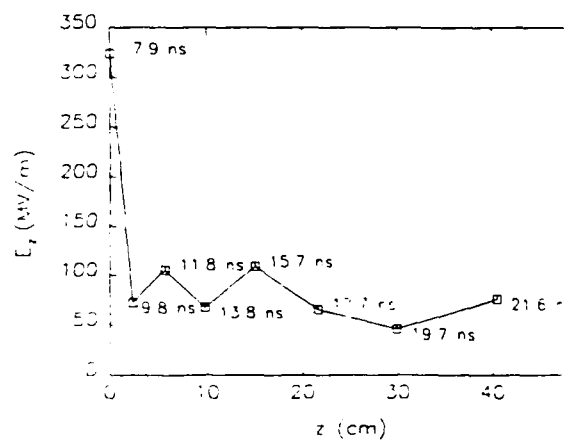
Fig. 6. Magnitude vs. location of peak electric field.

Fig. 4. Peak proton energy measured at 45 cm vs. time delay.

INTENSE ELECTRON BEAM PROPAGATION ACROSS A MAGNETIC FIELD

X. Zhang, C.D. Striffler, R.L. Yao, W.W Destler, and M. Reiser

Electrical Engineering Department

and

Laboratory for Plasma Research

University of Maryland, College Park, MD 20742

Abstract

In this paper we consider the propagation of an intense electron-ion beam across an applied magnetic field. In the absence of the applied field, the beam system is in a Bennett equilibrium state that involves electrons with both large axial and thermal velocities and a cold stationary space-charge neutralizing ion species. Typical parameters under consideration are $V_o \sim 1$ MV, $I \sim 5$ kA, $T_e \sim 100$ keV, and beam radii $\sim$ 1 cm. We find that in the intense beam regime, the propagation is limited due to space-charge depression caused by the deflection of the electron beam by the transverse field. This critical field is of the order of the peak self-magnetic field of the electron beam which is substantially higher than the single particle cut-off field.

Introduction

The objective of the present investigation is to provide a theoretical understanding of the experiments performed at the University of Maryland on electron-ion beam propagation across a transverse magnetic field[1],[2]. The configuration investigated is shown in Fig. 1. Nominal diode parameters are 1 MV, 20 kA, and a FWHM of 30 nsec. The beam is injected through a hole into an evacuated drift tube. In order to obtain effective beam propagation to the end of the drift tube, a localized gas cloud near the injection hole is employed and collectively accelerated ions from the gas cloud provide a channel of neutralization that allows electrons injected late in the pulse to propagate. Under optimum conditions 20 kA can be propagated to the Faraday cup with no applied axial magnetic field.

In order to investigate the effects of a transverse magnetic field on this co-moving electron-ion beam, a Helmholtz coil is placed about half-way down the drift tube. If no gas is puffed into the system, that is, no ions are supplied, about 1 kA is observed at the Faraday cup with zero transverse magnetic field. As the transverse field is increased, the observed current steadily decreases to zero at about 200 gauss. When the gas cloud is present, about 5 kA are detected at the Faraday cup with zero transverse field. As the transverse field is increased, the entire 5 kA is propagated up to about 200 gauss with a steady but slow decrease in collected current above 200 gauss. The detected current goes to zero around 500 gauss. The purpose of these studies is to evaluate the properties of co-moving electron and ion beams for use in collective field accelerators and for beam propagation into free-space.

Previous theoretical studies have shown the existence of a self-consistent downstream Bennett equilibrium for the electrons and ions when no applied magnetic field is present[3]. We have related these downstream properties to the diode voltage, the transmitted electron beam current, and the ion properties

in the localized gas cloud region. For our experimental parameters, $V_o = 1$ MV, $I = 5$ kA, the downstream self-pinched equilibrium state is composed of cold ions with low axial speed ($<$ 0.05 c), and electrons with a temperature of about 60 keV and an axial speed of about 0.84 c. The nearly charge-neutral beam system has been shown to effectively propagate up to the diode current of 20 kA where the electron temperature is predicted to be about 200 keV. The 5 kA case was chosen for examining the effects of a transverse magnetic field on the electron-ion beam system, mainly because of experimental reproducibility.

Other work in the area of beam propagation across transverse magnetic fields usually consider a charge and current neutralized ion beam [4]-[8]. These systems have application to ion beam heating of dense plasmas, where an intense ion beam is charge and current neutralized by electrons so that it can penetrate the large applied fields in a fusion plasma. In these cases a two layer polarization model is adopted in the rigid beam limit. The polarization electric field allows the beam to propagate across the magnetic field by means of an $\mathcal{E} \times \mathcal{B}$ drift.

Model, Basic Equations, and Results

Consider a rigid beam model of the Bennett equilibrium system discussed in the previous section. Electron and ion beams of equal radii are incident along the z-axis onto a transverse magnetic field region. To simplify the analysis the profile of the Helmholtz coil is replaced by a constant magnetic field B_T in the y-direction over an axial distance $L_T \sim 20$ cm. In the parameter regime of interest, the electron gyroradius is comparable to L_T which is much larger that the effective Bennett beam radius a and the ion beam is assumed to be stationary and centered on the z-axis. The electron beam is confined by the self-magnetic field. The rigid electron beam is deflected by the transverse field B_T but feels a restoring force due to the ion beam. In this model, we examine only the effects of transverse forces on the rigid electron rod. Longitudinal forces and/or effects that arise as the beam front end enters the transverse magnetic field region are ignored.

When there is no transverse field, $B_T = 0$, the electron and ion components of the beam system are centered on the z-axis, are charge neutral, $n_{io} = n_{eo} = n_o$, and have identical Bennett profiles of the same effective radius, $a_i = a_e = a$. That is, the density profiles are

$$n_\alpha(r) = \frac{n_{oo}}{[1 + (r/a)^2]^2}, \alpha = i, e \qquad (1)$$

and the electron beam self-magnetic field due to the mean axial electron velocity V_{eo} is

$$B_{S\phi}(r) = -\frac{e\mu_o}{2} V_{eo} \frac{n_{eo}r}{1 + (r/a)^4}. \qquad (2)$$

The ions are stationary and assumed infinitely massive. The equations of motion for the center of the electron beam are

$$\frac{dp_x}{dt} = eB_T V_z + F_n(x) \qquad (3)$$

$$\frac{dp_z}{dt} = -eB_T V_x. \tag{4}$$

where $p_x = m\gamma V_x$, $p_z = m\gamma V_z$, and $\gamma = [1-(V_x/c)^2-(V_z/c)^2]^{-1/2}$. The averaged ion electric force acting on the rigid electron beam when the electron rod is displaced a distance x is

$$
\begin{aligned}
F_{ei}(x) &= -\frac{e}{Ne}\int E_{ri}(r)n_e(r)dS_e \\
&= \frac{-e^2 n_o a}{S\epsilon_o}\left[\frac{\bar{x}/2}{1+(\bar{x}/2)^2} + \frac{1}{(\bar{x}/2)} \right. \\
&\quad \left. + \frac{\sinh^{-1}(-\bar{x}/2) - \sinh^{-1}(3\bar{x}/2 + \bar{x}^3/2)}{\bar{x}^2[1+(\bar{x}/2)^2]^{3/2}}\right]
\end{aligned} \tag{5}
$$

where $\bar{x} = x/a$.

In general, Eqns. (3) and (4) have to be solved numerically. However, if the displacement distance x is small compared to the beam radius, $\bar{x} \ll 1$, the ion electric restoring force can be approximated as

$$F_{ei}(x) \simeq \frac{-e^2 n_o}{6\epsilon_o}x. \tag{6}$$

Furthermore, assuming the relativistic factor γ remains constant, $\gamma = \gamma_o = [1 - (V_{zo}/c)^2]^{-1/2}$, we find the solutions to Eqns. (3) and (4) to be

$$x(t) = \frac{\omega_c V_{zo}}{\omega^2}(1 - \cos\omega t) \tag{7}$$

and

$$V_z(t) = V_{zo}\left[1 - \left(\frac{\omega_c}{\omega}\right)^2(1 - \cos\omega t)\right], \tag{8}$$

with

$$\omega^2 \equiv \omega_c^2 + \frac{\omega_p^2}{6}, \quad \omega_c = \frac{eB_T}{m\gamma_o}, \quad \omega_p^2 = \frac{e^2 n_o}{\epsilon_o m\gamma_o}, \tag{9}$$

where ω_c, ω_p are the electron cyclotron and plasma frequencies. These solutions are similar to the results obtained by Peter and Rostoker[8], who used the two-layer polarization model. Since the oscillatory behavior of the electron rod is due to the deflecting applied transverse magnetic field and the restoring ion beam electric field force, we see that the frequency of these oscillations is a function of both ω_c and ω_p. Averaging out the oscillations in Eq. (8), we obtain for the time-averaged mean axial velocity of the electron beam

$$\bar{V_z} = V_{zo}\left(1 - \frac{\omega_c^2}{\omega^2}\right) \equiv V_{zo}(1 - 1/\epsilon), \tag{10}$$

where $\epsilon = 1 + \omega_p^2/6\omega_c^2$. This result is identical to that in reference [8] with the modified definition of ϵ.

Returning to Eqns. (3) and (4), we have solved these equations numerically for a given beam current as a function of the applied transverse magnetic field amplitude. The results for a 5 kA beam are displayed in Fig. 2. From reference [3], the self-consistent : an electron axial velocity is $V_{zo} = .84c$ for a beam radius of 1.0 cm. The peak self-magnetic field for this beam system is about 500 G [from Eqn. (2)]. The results displayed are typical for beams in the "intense" regime. Specifically, we have plotted in Fig. 2a the maximum beam displacement versus the transverse field amplitude, B_T, shown as the solid line. In Fig. 2b, the minimum axial velocity of the electron beam, which occurs at maximum displacement, is plotted versus B_T (solid line). As shown, the maximum displacement continually increases with B_T until a value is reached such that the axial velocity goes to zero. This value of the magnetic field

at which $\beta_{z,MIN} \to 0$, is defined as B_{TC} and the displacement amplitude for this field x_c. For values of B_T above B_{TC}, the beam will blow up in its own space-charge. We see that this critical value is very close to the peak self-magnetic field of the Bennett beam.

The values of B_{TC} and x_c can be related from the constants of motion. From Eqns. (3) and (4), these constants are the total energy and the axial canonical momentum, which can be written as

$$(\gamma - 1)mc^2 - e\Phi_e = (\gamma_o - 1)mc^2 \tag{11}$$

and

$$p_z + eB_T x = p_{zo} = m\gamma_o V_{zo}, \tag{12}$$

where the effective potential is given as $\Phi_e = (1/e)\int_o^x F_{ei}(x')dx'$. From Eqn. (12), when $p_z = 0$, then $x \to x_c$ and $B_T \to B_{TC}$, that is

$$B_{TC}x_c = \frac{p_{zo}}{e} = m\gamma_o e V_{zo}. \tag{13}$$

In the intense beam regime, when β_z goes to zero at B_{TC} we also have $\beta_x = 0$. That is, at this critical magnetic field $\gamma(x_{MAX} = x_c) = 1$, all the electron beam energy goes into potential energy. From Eqn. (11), with $\gamma = 1$, we obtain

$$e\Phi_e(x_c) = \frac{eI}{4\pi\epsilon_o V_{zo}}\ln\left[1 - \frac{1}{3}\left(\frac{x_c}{a}\right)^2\right] = (\gamma_o - 1)mc^2 \tag{14}$$

Thus, from Eqn. (14) we can determine x_c for a given injected beam, and determine the critical magnetic field from Eqn. (13). That is,

$$B_{TC} = \frac{m\gamma_o V_{zo}}{ex_c} = \frac{m\gamma_o V_{zo}}{e\sqrt{3}a}\left[\exp\left(\frac{17}{I(kA)}(\gamma_o - 1)\beta_{zo}\right) - 1\right]^{-1/2}. \tag{15}$$

the critical magnetic field for beam propagation in the intense beam regime.

If the beam current is sufficiently low, $I < 4kA$, we find that when $\beta_z \to 0$, β_x is not zero. In the single particle limit, this is obvious since as $\beta_z \to 0, \beta_x \to \beta_o$, since $\gamma = \gamma_o$ along the entire trajectory. In this case $x_c = p_{zo}/eB_{TC} = V_{zo}/\omega_c = R_e = L_T$, the electron Larmor radius. For beam currents between the single particle limit and the intense beam regime discussed above, Eqn. (11) tells us that part of the initial beam kinetic energy goes into potential energy as the beam is deflected. A summary of these results is shown in Fig. 3 where we have plotted the critical magnetic field B_{TC} versus beam current I. This graph is generated for the case of a 1 MV diode[3] and the self consistent downstream Bennett equilibrium. The mean axial velocity V_{zo} depends on the transmitted current as shown in reference[3] and this is included in the plot in Fig. 3. We see that the single particle cutoff field is about $250G[V_o = 1MV, L_T = 18cm = R_e]$. As the current is increased the critical field remains at the single particle limit until the beam current reaches a value such that its peak self-magnetic field is near the single particle cut-off field. Further increases in the beam current result in entering the intense beam regime where the critical field is a result of potential depression ($\gamma \to 1$ as $\beta_z \to 0$).

In order to explicitly compare our results with those of the experiment, we must normalize our uniform field model with a Helmholtz coil profile. We have displayed in Fig. 2a and 2b the numerical results of solving Eqns. (3) and (4) for a

5 kA electron beam transversing a Helmholtz coil configuration. The coil field amplitude is the peak on-axis value. From conservation of axial canonical angular momentum and energy conservation, the relationship between the critical uniform field B_{TC} and that of the Helmholtz coil field profile is

$$B_{TC} = \frac{1}{x_c} \int_o^{x_c} B_{HC}(x', z(x')) \, dx'. \qquad (16)$$

Discussion

For a given injected electron beam that is charge neutralized but not current neutralized by a stationary ion beam and has a Bennett equilibrium profile, we have determined the critical transverse magnetic field above which the beam will not propagate. In the intense beam regime, this limit is a result of space-charge depression caused by the deflection of the electron beam from the center of the ion channel. The value of the critical field is approximately given by the peak self-magnetic field of the electron beam.

A concern about the rigid beam model is the individual particle confinement in the Bennett equilibrium. The application of a transverse field results in a non-symmetric force about the beam axis. We have examined the individual particle trajectories for typical Bennett particles and have found the non-symmetry has substantial individual particle effects as B_T approaches $B_{s\phi}(a)$. We believe that this will lead to fractional loss of beam current as the beam transverses the field region. This fractional loss is observed in the experiment as B_{TC} is approached.

References

1. W.W. Destler, C.D. Striffler, Z. Segalov, R.L. Yao, X. Zhang, and J. Rodgers, Proc. O-E/LASE '88, Sym. Innovative Sci. & Tech., paper 873-33, Jan. 10-15, 1988.

2. W.W. Destler, J. Rodgers, Z. Segalov, C.D. Striffler, R.L. Yao, X. Zhang, and J. Guillory, 7th Inter. Conf. on High-Power Particle Beams, Beams '88, July 4-8, 1988, p. 185.

3. C.D. Striffler, R.L. Yao, and X. Zhang, Proc. of the 1987 IEEE PAC, page 975.

4. G. Schmidt, Phys. Fluids 3, 961 (1960).

5. K.D. Sinel'nikov and B.N. Rutkevich, Sov. Phys. - Tech. Phys. 12, 37 (1967).

6. E. Ott and W.M. Manheimer, Nuclear Fusion 17, No. 5, 1057 (1977).

7. F. Wessel and S. Robertson, Phys. Fluids 24, 739 (1981).

8. W. Peter and N. Rostoker, Phys. Fluids 25, No. 4, 730 (1982).

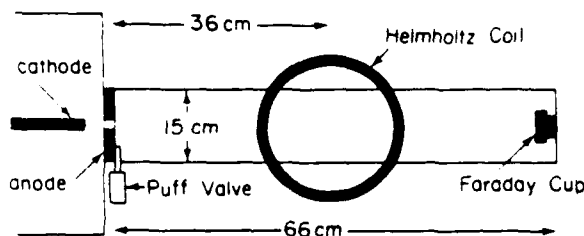**Fig. 1.** Experimental configuration used for beam propagation studies across a magnetic field.
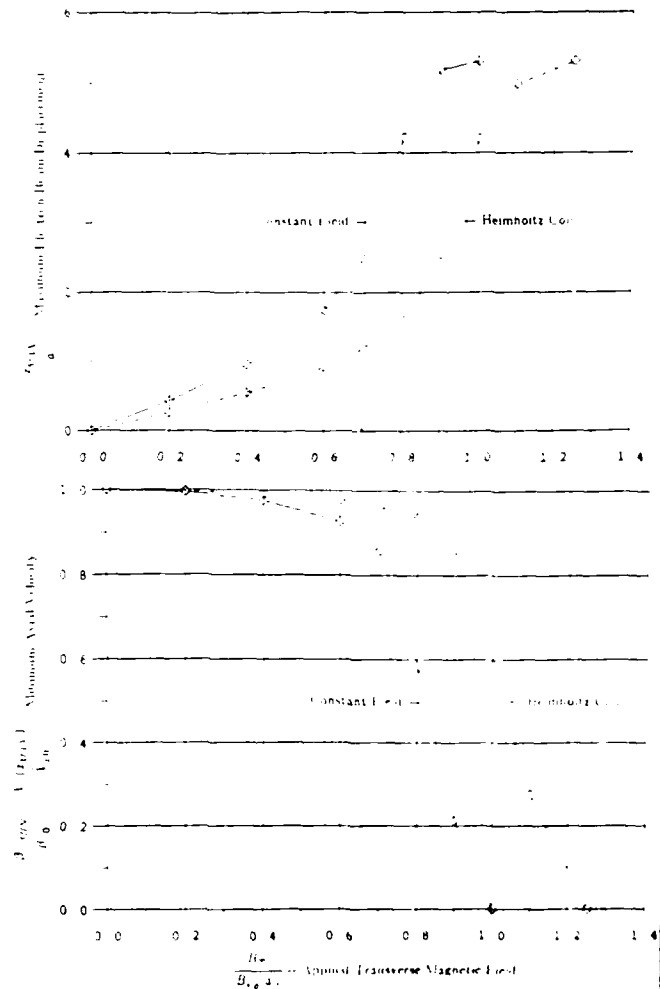

Fig. 2. Typical results in the Intense Beam Regime. (a) Maximum electron beam displacement and (b) minimum beam axial velocity versus the applied transverse magnetic field amplitude. The "solid" line represents the constant field model and the "dashed" line a Helmholtz coil configuration (peak on-axis amplitude). Fixed beam parameters are: $I = 5$ kA, $\beta_{zo} = 0.84$, $a = 1$ cm, and $B_{s\phi}(a) \simeq 500$ G.
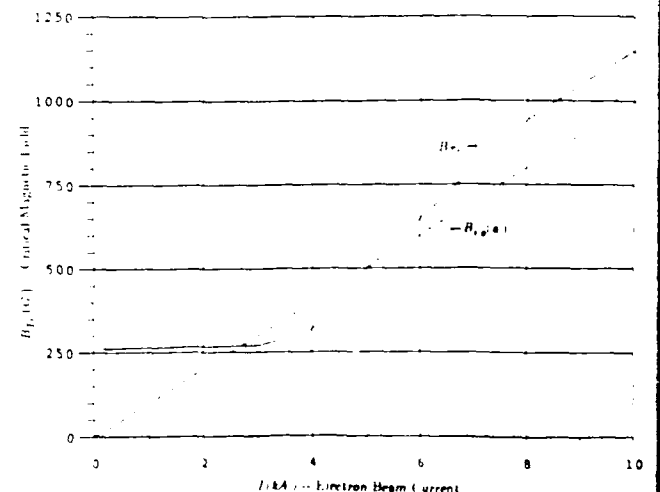

Fig. 3. Critical transverse magnetic field, defined by $\beta_z = 0$, versus electron beam current. The "dashed" line represents the peak self-magnetic field of the electron beam. The beam radii are 1 cm and the diode voltage is 1MV. See reference [3].

EMITTANCE MEASUREMENT OF A PSEUDOSPARK-PRODUCED ELECTRON BEAM

M. J. Rhee and E. Boggasch

Laboratory for Plasma Research

University of Maryland, College Park, Maryland 20742 U.S.A.

ABSTRACT

We report the first measurement of the rms emittance of a pseudospark-produced electron beam. A six gap pseudospark chamber filled with argon gas was operated at ~ 25 kV, producing a ~ 10 Hz repetitive pulse train of electron beams. Typically, a beam of average energy 20 keV, peak current ~ 50 A and pulse duration ~ 10 ns FWHM was extracted from the chamber. The rms emittance was evaluated by using the slit-hole method. A typical value of rms emittance was found to be $\epsilon \simeq 55$ mm-mrad, yielding a normalized emittance of $\epsilon_n \simeq 15$ mm-mrad. The normalized brightness of the beam was then estimated as $B_n = I/\epsilon_n^2 \simeq 2 \times 10^{11} A/(m^2 rad^2)$.

I. INTRODUCTION

Interest in high quality, high current electron beams has been stimulated by their application with regard to such field as advanced accelerators and free electron lasers.[1,2] Pseudospark discharge phenomenon with interesting charged particle emission characteristics was reported by Christiansen and Schultheiss[3] in 1979. At the University of Maryland, an experiment was performed to measure for the first time the emittance of an electron beam produced by a pseudospark discharge.

In this paper, we shall describe the operation of a six gap pseudospark chamber which is characteristically similar to the devices reported by other laboratories.[3-7] Repetitively pulsed (~ 10 Hz) electron beams were extracted through an anode hole into a drift region. The beam currents were measured by a Rogowski coil at the anode and a Faraday cup placed downstream. A simple emittance meter[8] consisting of a series of thin slits and detector film was placed downstream of the anode. Angular distributions of sheet beamlets formed after passing through the slits were recorded on radiachromic film.[9] The optical density distribution of the film after exposure to the beam provide us with the distribution of the transverse components of electron velocities from which the rms emittance is evaluated. Subsequently, we describe the emittance analysis and estimation of brightness of the beam. Finally,

II. EXPERIMENTAL ARRANGEMENT

The experimental setup is shown in Fig. 1. The discharge chamber consists of a hollow cathode, five modules of intermediate electrodes and insulators, and an anode with a center hole for electron beam extraction. Intermediate electrodes made of 3.2 mm thick brass have outer diameter of 6.35 cm and center hole diameter of 3.2 mm. The 3.2 mm thick plexiglas insulator washers have outer and inner diameters of 7 cm and 2.54 cm respectively. In addition to the chamber capacitance of 11 pF between anode and cathode, a low inductive external capacitor of 420 pF was added for the present work. A 50 cm long drift chamber is attached to the anode side to accommodate diagnostics such as the emittance meter or the Faraday cup. A capacitance-manometer type vacuum gauge was used to measure the gas fill pressure which was almost statically balanced by a needle valve and a throttle vacuum valve as shown in Fig. 1. Two Rogowski coils were molded into axisymmetric grooves milled into both side of the anode flange so that the azimuthal component of the magnetic field, which arises from the axisymmetric current, is predominantly supported and other components (noises) are suppressed. The rise time of the Rogowski coil system may be approximately given by L/Z_0, where L is the inductance of the coil and Z_0 is the characteristic impedance of the transmission line used, and is found to be less than 0.5 ns. A Faraday cup consisting of a 3 cm diam graphite beam collector and a 10 mΩ current viewing resistor placed on axis of the downstream drift chamber was employed to measure the beam current at various axial positions. The chamber voltage was measured by a homemade high impedance resistive voltage probe of division ratio 1:20,000 into a 50 Ω load. The response of the probe was greatly improved by a proper compensation for the stray capacitance in the carbon resistors used. The resulting rise time is less than 0.5 ns, and the RC droop time constant due to the blocking capacitor is $\sim$120 ns. For emittance measurement, a slit-hole type emittance meter was employed and was placed in the drift chamber 9 cm downstream of the anode. The emittance meter consists of a series of parallel thin slits of 200 μm width and 2 mm spacing constructed from 0.6 mm thick stainless steel plate; 2 mil thick radiachromic film, used as a beam detector was placed 12 mm downstream of the slit plane.
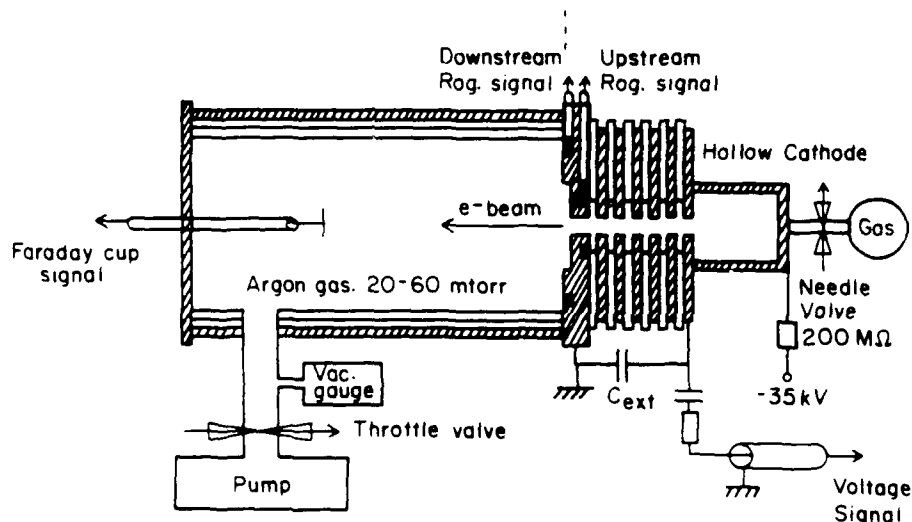

Fig. 1. Experimental setup.

The system was operated typically at 30 kV. with an argon gas pressure of 30 mTorr.

For the emittance measurement. exposures of approximately five consecutive beam pulses to the radiachromic film through the slits in the emittance meter were enough to produce an appropriate density profile. with the peak value of the optical density not exceeding 0.5. This ensure that the measured optical density distribution is linear to the beam intensity.[9] The density profile was obtained by scanning the film using an optical microdensitometer. and is shown in Fig. 2.

III. ROOT-MEAN-SQUARE EMITTANCE ANALYSIS

The root-mean-square (rms) emittance[10] (or effective emittance[11]). which has been widely used as a measure of beam quality. was defined as

$$\epsilon = 4\left\{ <r^2><r'^2> - <rr'>^2 \right\}^{1/2}. \tag{1}$$

where r' is the gradient of the particle trajectory given by $r' = dr/dz = p_r/p_z$. and the angular brackets denote average values over the two-dimensional trace space as

$$<o> = \int o\rho(r.r')drdr'. \tag{2}$$

where ρ is the projected density in two-dimensional trace space. and is assumed to be normalized. i.e.. $\int \rho dr dr' = 1$.

It is very reasonable to assume that as in Ref. 8. the beam produced in this experiment is axisymmetric and of Maxwellian transverse velocity distribution. This allows us to use the simple slit-hole type emittance meter mentioned above. whose results can be easily analyzed.[8] We find empirical functions $\alpha(r)$. $\beta(r)$. and $\sigma(r)$ as functions of radial position r from the density profile shown in Fig. 2. where $\alpha(r)$ is the mean diverging angle. $\beta(r)$ represent the peak values. and $\sigma(r)$ is the rms width of the individual distributions. Numerical integrations were then performed using the empirical functions α. β. and σ to find ρ and the moments $<r^2>$. $<r'^2>$. and $<rr'>$ (see Ref. 8 for details). Several isodensity contours of the resultant $\rho(r.r')$ were constructed in $r - r'$ space (known as an emittance plot) as shown
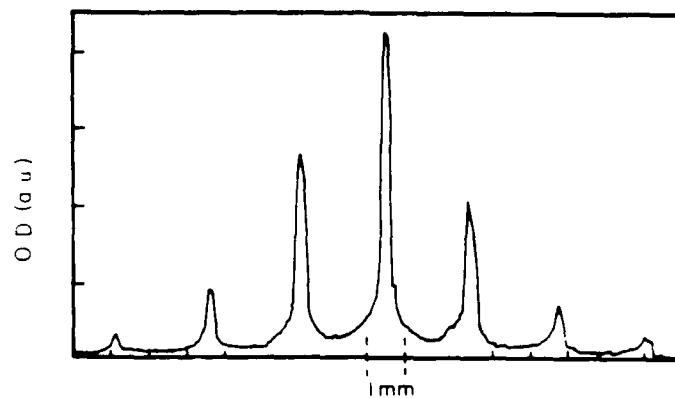

Fig. 2. Optical density distribution on the radiachromic film after exposure to the beamlets.

in Fig. 3. The measured rms emittance, given by Eq. (1) with the obtained moments, was found to be

$$\epsilon \simeq 55mm - mrad. \tag{3}$$

It is interesting to note that the emittance plot in Fig. 3 shows a slightly S-shaped contour; this is indicative of the existence of nonlinear focusing(defocusing) in the beam indicating the possible existence of space charge field of substantial strength. The normalized rms emittance $\epsilon_n = \beta\sigma\epsilon$, which is invariant[11,12] when there is acceleration in the axial direction, is conveniently used for comparing beam qualities at different energies. With an average beam energy of 20 keV inferred from the voltage probe signal, the normalized emittance is estimated to be $\epsilon_n \approx 15$ mm-mrad. Another useful invariant of the beam associated with the emittance is the brightness.[11] We use here a simpler mathematical expression of normalized rms brightness $B_n = I/\epsilon_n^2$, so as to compare with other results by other laboratories using different definitions.[13] With a measured current of $\sim$50 A, we obtained the brightness

$$B_n = I/\epsilon_n^2 \simeq 2 \times 10^{11} A/m^2 rad^2. \tag{4}$$

which is an order of magnitude higher than that of other high brightness sources.[13] It should be noted here that the results in this work are all time integrated over 5 shots.

IV. CONCLUSIONS

We have measured, for the first time, the emittance of a pseudospark-produced electron beam. A *six gap pseudospark* chamber with argon gas was operated at $\sim$ 25 kV and produced a $\sim$ 10 Hz repetitive pulse train of electron beams. Typically, a beam of average energy 20 keV, peak current $\sim$50 A and pulse duration $\sim$10 ns FWHM was extracted from the chamber. The rms emittance was evaluated by using the slit-hole method. The typical value of rms emittance was found to be $\epsilon \simeq$ 55 mm-mrad, yielding a normalized emittance of $\epsilon_n \simeq 15$ mm-mrad. These values
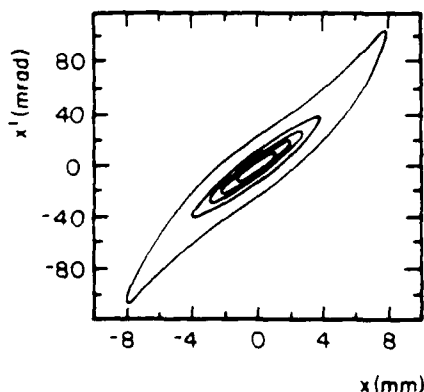

Fig. 3. The emittance plot in x-x' trace space.
The isodensity contours correspond to 0.1, 20,
40, 60, and 80% of the peak value.

are time integrated over 5 shots: thus they represent upper limits. The normalized rms brightness of the beam was then estimated as $B_n = I/\epsilon_n^2 \simeq 2 \times 10^{11} \, \text{A}/(\text{m-rad})^2$. which is an order of magnitude higher than existing high brightness electron beam sources.

ACKNOWLEDGMENTS

REFERENCES

1. R. Stiening. "The status of the Stanford Linear Collider." Proc. 1987 IEEE *Particle Accelerator Conference* (Edited by E.R. Lindstrom and L.S. Taylor. 1987). p. 1.

2. IEEE J. Quantum. Electron. QE-21. (1985). pp. 804-1119. special issue papers therein.

3. J. Christiansen and C. Schultheiss. "Production of high current particle beams by low pressure spark discharges." Z. Phys. A. 290. 35 (1979).

4. X.L. Jiang. K.F. Chen. S.C. Jiang, and Y.B. Piao. "Neutralization and focusing of pulsed beams with high current densities." IEEE Trans. Nucl. Sci. NS-32. 1814 (1985).

5. P. Choi. H.H. Chuaqui. M. Favre, and E.S. Wyndham. "An observation of energetic electron beams in low pressure linear discharges." IEEE Trans. Plasma Sci.. PS-15. 428 (1987).

6. C. Schultheiss. "Insulator with reduced E-field on surface." *Nuclear Instruments and Methods* A 254. 398 (1987).

7. H. Gundel. H. Riege. J. Handerek. and K. Zioutas. "Low pressure hollow cathode switch triggered by a pulsed electron beam emitted from ferroelectrics." Appl. Phys. Lett. 54. 2071 (1989).

8. M.J. Rhee and R.F. Schneider. "The root-mean-square emittance of an axisymmetric beam with a Maxwellian velocity distribution." Particle Accelerators. 20. 133 (1986).

9. W.L. McLaughlin. R.M. Uribe. and A. Miller. "Megaray dosimetry." Radiat. Phys. Chem.. 22. 333 (1983).

10. P.M. Lapostolle. "Possible emittance increase through filamentation due to space charge in continuous beams." IEEE Trans. Nucl. Sci.. NS-18. 1101 (1971).

11. J.D. Lawson. The Physics of Charged-Particle Beams (2nd ed.. Clarendon. Oxford. U.K. 1988).

12. M.J. Rhee, "Invariance properties of the root-mean-square emittance in a linear system." Phys. Fluids. 29. 3495 (1986).

13. D.A. Kirkpatrick. R.E. Shefer. and G. Bekefi. "High brightness electrostatically focused field emission electron gun for free electron laser applications." J. Appl. Phys. 57. 5011 (1985). references therein.

Basic circuits for inductive-energy pulsed power systems

M. J. Rhee, T. A. Fine, and C. C. Kung

Department of Electrical Engineering, University of Maryland, College Park, Maryland 20742

A comprehensive analysis of pulse formation in inductive-energy pulsed power circuits is presented. The output waveforms, with relevant circuit parameters, are derived for four basic systems, including two new circuit configurations useful for practical applications.

I. INTRODUCTION

Inductive-energy pulsed power systems (PPS's) have recently attracted a great deal of attention, mainly because of their compactness in size as compared to the more often used capacitive PPS's. Due to relatively slow progress in the development of fast opening switches, most of the inductive-energy PPS's now in use have been limited to slow pulse systems[1] in which a simple lumped inductor is employed as the energy-storage element. It has been shown[2] that, in lieu of the lumped inductor, a transmission line can be used to store the inductive energy in order to produce a square output pulse. Such square-pulse generation has been experimentally demonstrated by using a light-activated, fast semiconductor opening switch.[3] As the development of opening switches progresses, one may expect to see—as in the case of capacitive PPS's—a demand for a variety of circuit configurations in order to meet the requirements of the many and diverse applications that will naturally arise.

It is realized that there exists a "dual" relationship[4] between the capacitive- and the inductive-energy PPS's. One can construct an inductive-energy PPS circuit from a capacitive energy PPS circuit by replacing capacitance with inductance, inductance with capacitance, resistance with conductance, closing switch with opening switch, and series connection with parallel connection. The behavior of voltage in the dual circuit is the same as that of current in the original circuit, and vice versa.

In this paper we present a comprehensive analysis of pulse formation in four basic inductive-energy PPS circuits, including two new circuits. Most other possible systems may be considered as a variation and/or combination of the above systems. The circuits described in the following sections are (1) the lumped inductor system, (2) the current charged transmission line, (3) the dual of the LC generator,[5] and (4) the dual of the Blumlein line.[5] Also discussed are the features and results of each system in conjunction with possible applications.

II. LUMPED INDUCTOR SYSTEM

This may be the simplest form of inductive-energy PPS's. It consists of a current charged inductor and an opening switch with a capacitor connected in parallel, as shown in Fig. 1(a). The stored energy in the inductor, $\frac{1}{2}LI_0^2$ is released to the load resistor by the opening switch. This circuit is the well known parallel RLC circuit, for which the governing equation is given by

$$\frac{d^2v}{dt^2} + \frac{1}{RC}\frac{dv}{dt} + \frac{v}{LC} = 0. \tag{1}$$

The switch is opened at $t = 0$, interrupting the initial charging current I_0. Three different types of solutions for the output waveform exist, depending on the circuit parameters: (a) for $\alpha > \omega_0$ (overdamped),

$$v(t) = \frac{I_0}{C(\alpha^2 - \omega_0^2)^{1/2}}e^{-\alpha t}\sinh(\alpha^2 - \omega_0^2)^{1/2}t, \tag{2}$$

where $\alpha = 1/(2CR)$ and $\omega_0 = (LC)^{-1/2}$; (b) for $\alpha = \omega_0$ (critical damping),

$$v(t) = (I_0 t/C)e^{-\alpha t}, \tag{3}$$

(c) for $\alpha < \omega_0$ (underdamped),

$$v(t) = \frac{I_0 e^{-\alpha t}}{C(\omega_0^2 - \alpha^2)^{1/2}}\sin(\omega_0^2 - \alpha^2)^{1/2}t. \tag{4}$$

These solutions, with typical parameters, are plotted in Fig. 1(b).

Due to the presence of the parallel connected capacitance, the output waveforms have a finite rise time, which, in turn, results in a reduction of peak amplitude. The rise time T_p (at which the amplitude peaks) is found by solving $dv/dt(T_p) \equiv 0$, yielding the corresponding peak amplitude $V_p = v(T_p)$. The expressions for T_p and V_p for the above three cases are listed in Table I.

It should be mentioned that this simple system is the most popular electrical PPS found in practical applications. The ignition-coil system used in most automobile engines is a slight variation of this type. The role of the parallel capacitance in this case is to optimize the rise time in such a way that the finite rate of output voltage rise matches the voltage-holding characteristics of the mechanical opening switch (known as "breaker points") as it opens.

III. CURRENT CHARGED TRANSMISSION LINE

As shown in Ref. 2, a transmission line can be used in lieu of the lumped inductor and capacitor as a pulse-forming network. The transmission line of characteristic impedance Z_0 is initially current charged to I_0 as shown in Fig. 2(a). In this case the stored magnetic field energy, $\frac{1}{2}\int\mu H^2\,dv$, is again found to be $\frac{1}{2}LI_0^2$ (just as for the lumped inductor system), where L is the total inductance of the transmission line.
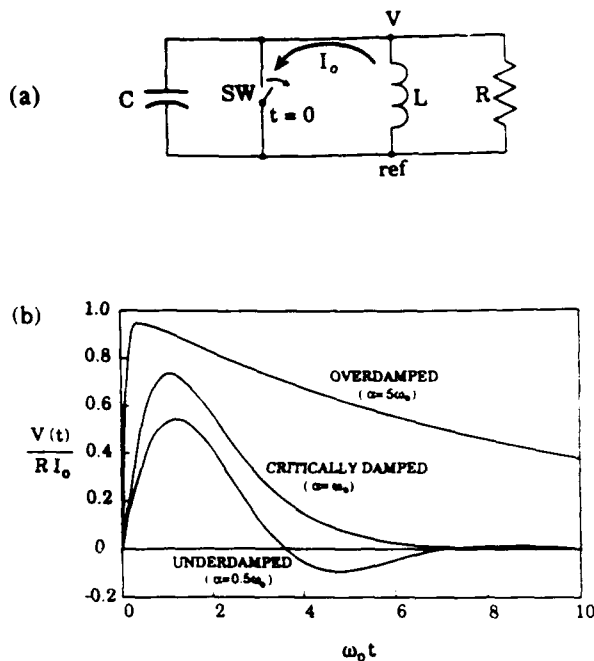
FIG. 1. Lumped inductor system (a) schematic diagram, and (b) typical output-voltage waveforms showing overdamped, critically damped, and underdamped cases.
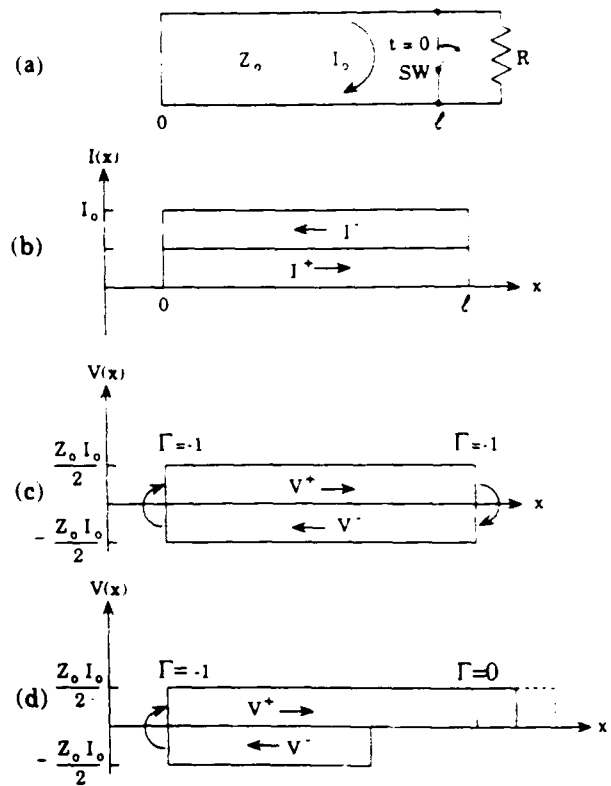

FIG. 2. Current charged transmission line: (a) schematic diagram; spatial distribution of (b) current and (c) voltage, shown as the superposition of a positively $\cdots\cdots\cdots$ wave and a negatively traveling wave before the switch is opened ($t < 0$), and (d) spatial distribution of voltage during the period $0 < t < \ell/v$.

The current I_0 may be considered the superposition of a positively traveling wave (PTW) ($I^+ = \frac{1}{2}I_0$, $V^+ = \frac{1}{2}Z_0 I_0$) and a negatively traveling wave (NTW) ($I^- = \frac{1}{2}I_0$, $V^- = -\frac{1}{2}Z_0 I_0$), both of which are constantly reflected back and forth by the shorted end ($\Gamma = -1$) and the closed switch ($\Gamma = -1$) until the switch opens [see Figs. 2(b) and 2(c)]. Γ is the reflection coefficient[6] (the ratio of reflected voltage wave to incident voltage wave), and is given by $\Gamma = (R - Z_0)/(R + Z_0)$. After the switch opens ($\Gamma = 0$) at $t = 0$, the charging current is then interrupted, allowing the PTW (I^+, V^+) to travel towards the resistive load, while the shorted end converts the rest of the NTW (I^-, V^-) to a PTW [see Fig. 2(d)]. As the PTW arrives at the matched load ($\Gamma = 0$), the wave is completely dissipated, resulting in the generation of a square output pulse. this resultant output pulse at the matched load has parameters $I_{out} = \frac{1}{2}I_0$, $V_{out} = \frac{1}{2}I_0 Z_0$, and $\tau = 2\ell/v$,

where ℓ is the length of the transmission line and v is the wave velocity in the transmission line [see Fig. 3(a)].

If the load is mismatched (i.e., $R \neq Z_0$) the PTW arriving at the load experiences a partial reflection due to the mismatch ($\Gamma \neq 0$); this reflected wave is then again reflected at the shorted end and sent back to the load. This cycle repeats with gradually reduced amplitude, resulting in a series of postpulses after the main pulse as shown in Figs. 3(b) and 3(c). Note that the two distinctive types of resulting waveforms, corresponding to $R > Z_0$ and $R < Z_0$, respectively, have a resemblance to those of the overdamped ($\alpha > w_0$) and underdamped ($\alpha < w_0$) cases in the

TABLE I. Rise time T_p and peak amplitude V_p of the output pulse in the lumped inductor system for three different damping conditions.

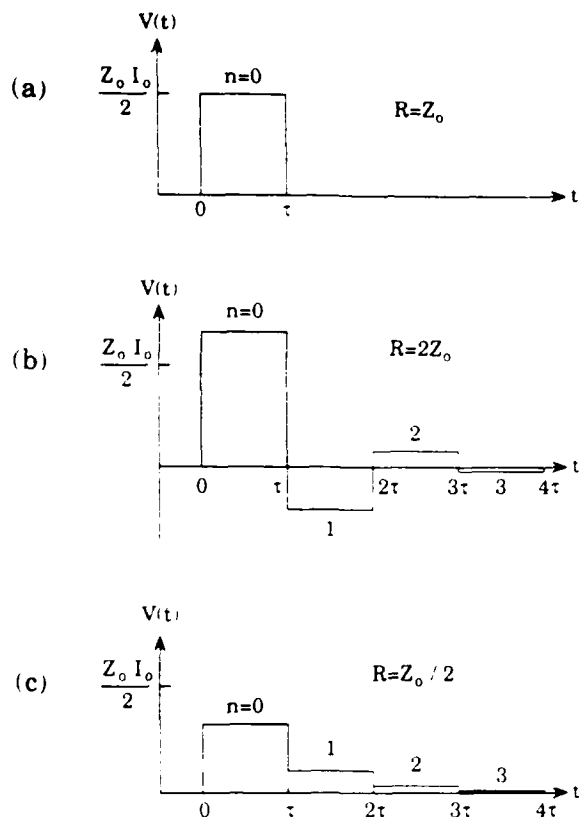| Damping condition	Rise time T_p	Peak amplitude V_p
Overdamped: ($\alpha > w_0$)	$\dfrac{1}{(\alpha^2 - \omega_0^2)^{1/2}} \tanh^{-1} \dfrac{(\alpha^2 - \omega_0^2)^{1/2}}{\alpha}$	$\dfrac{I_0}{C\omega_0}\left(\dfrac{\alpha - (\alpha^2 - \omega_0^2)^{1/2}}{\alpha + (\alpha^2 - \omega_0^2)^{1/2}}\right)^{\alpha/2(\alpha^2 - \omega_0^2)^{1/2}}$
Critical damping: ($\alpha = w_0$)	α^{-1}	$2RI_0 e$
Underdamped: ($\alpha < w_0$)	$\dfrac{1}{(\omega_0^2 - \alpha^2)^{1/2}} \tan^{-1} \dfrac{(\omega_0^2 - \alpha^2)^{1/2}}{\alpha}$	$\dfrac{I_0}{C\omega_0}\exp\left(\dfrac{-\alpha}{(\omega_0^2 - \alpha^2)^{1/2}} \tan^{-1} \dfrac{(\omega_0^2 - \alpha^2)^{1/2}}{\alpha}\right)$

FIG. 3. Typical output-voltage waveforms of the current charged transmission line with (a) matched load ($R = Z_0$), (b) $R > Z_0$ ($R = 2Z_0$), and (c) $R < Z_0$ ($R = Z_0/2$).
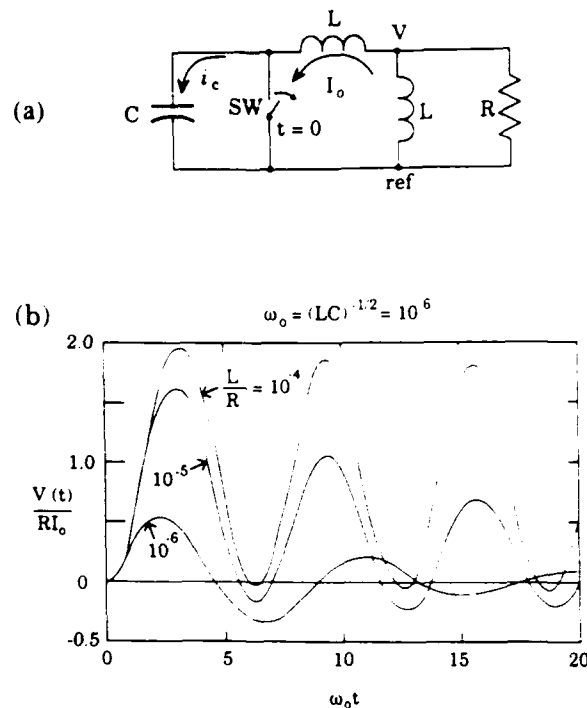

FIG. 4. Dual of the LC generator: (a) schematic diagram, and (b) typical output-voltage waveforms normalized to RI_0 for which $(LC)^{-1/2} = 10^6$, and $L/R = 10^{-4}$, 10^{-5}, and 10^{-6}.

lumped inductor system. The amplitude of the nth post-pulse for both cases is given by

$$V_{out}^n = RZ_0 I_0 [(Z_0 - R)^n/(Z_0 + R)^{n+1}], \qquad (5)$$

where $n = 0$ corresponds to the main pulse.

This current charged transmission line system may be considered the dual of the simple voltage-charged transmission line system; both systems produce a square output pulse. In the case of lumped energy-storage systems, the peak amplitude of the output is restricted by the finite rise time, which is inevitable due to stray capacitance, especially for very short pulse generation. For the case of the current-charged transmission line system, a very high-power pulse may be easily generated by simply shortening the pulse duration for a given stored energy, just as with its counterpart of the voltage-charged transmission line.

IV. DUAL OF THE LC GENERATOR

We introduce here a new circuit as shown in Fig. 4(a). Two inductors, which are current charged in series, and an opening switch are utilized. From the circuit point of view, this is a dual of the LC generator, which is a well-known capacitive energy PPS. The circuit may be described by the following third-order differential equation:

$$\frac{d^3v}{dt^3} + \frac{2R}{L}\frac{d^2v}{dt^2} + \frac{1}{LC}\frac{dv}{dt} + \frac{Rv}{L^2C} = 0. \qquad (6)$$

With appropriate initial conditions $v(0) = 0$, $dv/dt(0) = 0$, and $d^2v/dt^2(0) = I_0R/LC$, the solution (see Appendix) is found to be

$$v(t) = \frac{I_0 R}{LC[(\alpha - \beta)^2 + \omega^2]}$$

$$\times (e^{-\alpha t} - e^{-\beta t}\{\cos \omega t - [(\alpha - \beta)/\omega]\sin \omega t\}),$$

$$\qquad (7)$$

where $\alpha = 2R(3L)^{-1} - (r + d)^{1/3} - (r - d)^{1/3}$, $\beta = 2^{-1}[(r + d)^{1/3} + (r - d)^{1/3}] + 2R(3L)^{-1}$, $\omega = 3^{1/2}2^{-1}[(r + d)^{1/3} - (r - d)^{1/3}]$, $d = (q^3 + r^2)^{1/2}$, $q = (3LC)^{-1} - (2R)^2(3L)^{-2}$, and $r = -R(6L^2C)^{-1} - (2R)^3(3L)^{-3}$. The behavior of this solution depends largely on the circuit parameters R, L, and C; three typical cases are plotted in Fig. 4(b).

The main advantage of this system over the simple lumped inductor system is that, as with its dual counterpart, the LC generator, the output current amplitude can be as high as twice the initial charging current.

V. DUAL OF THE BLUMLEIN LINE

Here we introduce another new circuit that is the dual of the Blumlein line, a popular capacitive energy PPS. This circuit may also be considered as a distributed circuit version of the above mentioned dual LC generator. As shown in Fig. 5(a), two identical transmission lines of characteristic impedance Z_0 are initially current charged in series to I_0. This I_0 may be considered a superposition of a PTW ($I^+ = \frac{1}{2}I_0$, $V^+ = \frac{1}{2}Z_0I_0$) and a NTW ($I^- = \frac{1}{2}I_0$,
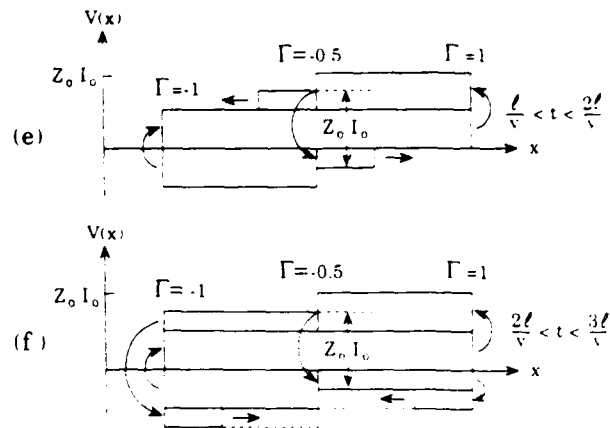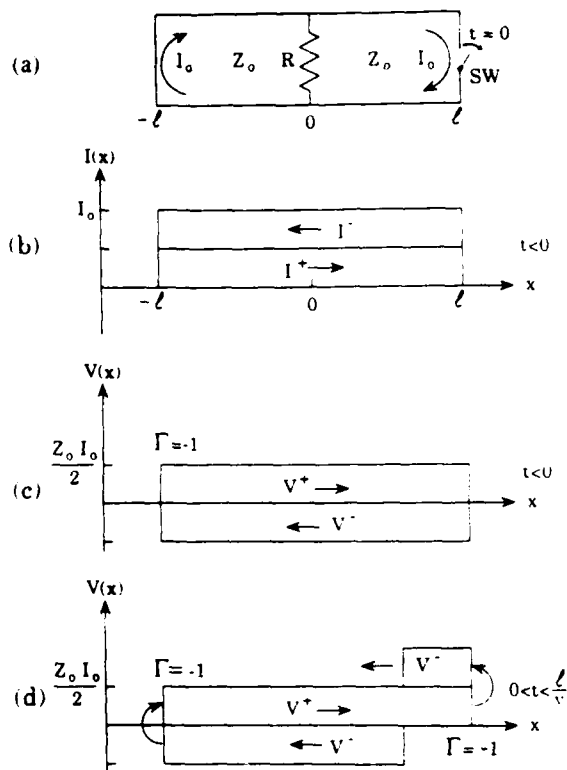
FIG. 5. Dual of the Blumlein line: (a) schematic diagram; spatial distribution of (b) current and (c) voltage, shown as the superposition of a positively traveling wave and a negatively traveling wave before the switch is opened ($t < 0$); and spatial distributions of voltage during the periods, (d) $0 < t < \ell/v$, (e) $\ell/v < t < 2\ell/v$, and (f) $2\ell/v < t < 3\ell/v$, respectively.

$V^- = -\frac{1}{2}Z_0I_0$), which are continuously reflected by both ends ($\Gamma = -1$), maintaining a steady state as shown in Figs. 5(b) and 5(c). Note that both the PTW and NTW experience a discontinuity at the midpoint where the load resistance R is connected in parallel; it can be shown, however, that the voltage (current) across the load resistance produced by both the PTW and NTW are of equal amplitude but of opposite sign. Thus no energy is dissipated in the load, just as if there were no discontinuity.

At $t = 0$, the current I_0 is disrupted by an opening switch ($\Gamma = 1$); the PTW (V^+) arriving at the switch end is reflected back with equal amplitude and same sign ($V^- = \frac{1}{2}Z_0I_0$) as shown in Fig. 5(d). This newly generated NTW (V^-) arrives at the midpoint and "sees" the discontinuity; for a matched load ($R = \frac{1}{2}Z_0$) the effective resistance and the reflection coefficient at this point are $Z_0/3$ and $\Gamma = -\frac{1}{2}$, respectively. The resulting reflected and transmitted waves are shown in Fig. 5(e). At this point, the voltage across the load resistance due to this new NTW is of the same sign as that of the PTW from the shorted end, thus generating the output voltage and current $V_{out} = I_0Z_0$ and $I_{out} = I_0$ until time $\tau = 2\ell/v$ when both the reflected wave (towards the switch) and the transmitted wave (towards the shorted end) reflect back again to the midpoint; after this time, both voltage and current are completely canceled along the entire length of both transmission lines [see Fig. 5(f)]. It is straightforward to show that for the cases with mismatched loads ($R \neq \frac{1}{2}Z_0$) a series of postpulses of gradually decreasing amplitude with either the same sign or alternating sign (depending on the condition $R > \frac{1}{2}Z_0$ or $R < \frac{1}{2}Z_0$) are generated, as shown in Fig. 6. The amplitude of the nth postpulse (again $n = 0$ corresponds to the main pulse) is given by

$$V_{out}^n = 2RZ_0I_0[(Z_0 - 2R)^n/(Z_0 + 2R)^{n+1}]. \qquad (8)$$
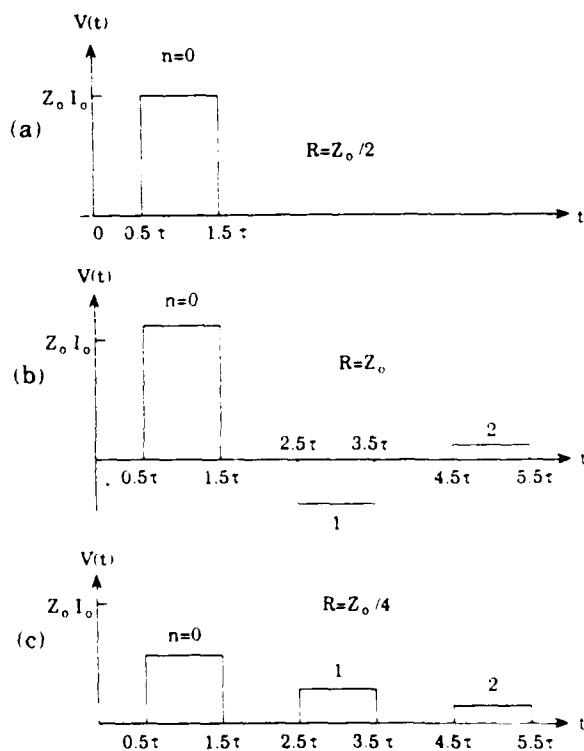
Note that, in this case, each pulse is separated by time

FIG. 6. Typical output waveforms of the dual of the Blumlein line with (a) matched load ($R = \frac{1}{2}Z_0$), (b) $R > \frac{1}{2}Z_0$ ($R = Z_0$), and (c) $R < \frac{1}{2}Z_0$ ($R = Z_0/4$).

$2\ell/v$. This is in contrast to the current-charged transmission-line case in which no such interpulse separation exists, as described previously.

As with its dual counterpart, the Blumlein line, this system is capable of producing a square pulse of equal amplitude to the charging current; this is twice that of the simple current charged transmission-line case. Another notable feature of this system is that the opening switch is positioned at the end of the transmission line; this allows direct connection of the load to the output of the system, thus removing possible circuit interference by the switch.

VI. CONCLUSIONS

We have systematically analyzed pulse formation in basic inductive-energy-storage PPS circuits. Exact expressions for output waveforms with relevant circuit parameters are derived for four basic circuits: the lumped inductor system, the current charged transmission line, the dual of the LC generator, and the dual of the Blumlein line. The last two systems are newly proposed and may be useful for practical applications.

ACKNOWLEDGMENTS

APPENDIX: DERIVATION OF EQ. (7)

For the circuit of Fig. 4, using Kirchhoff's current law at the node where v is measured, we obtain

$$\frac{V}{R} + \frac{1}{L}\int_0^t v\,dt + i_c = 0, \tag{A1}$$

where i_c is the charging current for the capacitor. The voltage v may be expressed in terms of i_c as

$$v = L\frac{di_c}{dt} + \frac{1}{C}\int_0^t i_c\,dt. \tag{A2}$$

Elimination of I_c in Eqs. (A1) and (A2) yields the following third-order differential equation:

$$\frac{d^3v}{dt^3} + \frac{2R}{L}\frac{d^2v}{dt^2} + \frac{1}{LC}\frac{dv}{dt} + \frac{Rv}{L^2C} = 0. \tag{A3}$$

Assuming the exponential solution $v = \Sigma A_n \exp(z_n t)$, the characteristic equation for Eq. (A3) is written as

$$z^3 + \frac{2R}{L}z^2 + \frac{1}{LC}z + \frac{R}{L^2C} = 0. \tag{A4}$$

This is a standard cubic equation having three roots—z_1, z_2, and z_3. The calculation of these roots may be found in any mathematical handbook. In this case, one real and two complex conjugate roots are found as

$$z_1 = -\alpha, \quad z_2 = -\beta + i\omega, \quad z_3 = -\beta - i\omega, \tag{A5}$$

where $\alpha = 2R(3L)^{-1} - (r + d)^{1/3} - (r - d)^{1/3}$, $\beta = 2^{-1}[(r + d)^{1/3} + (r - d)^{1/3}] + 2R(3L)^{-1}$, $\omega = 3^{1/2}2^{-1}[(r + d)^{1/3} - (r - d)^{1/3}]$, $d = (q^3 + r^2)^{1/2}$, $q = (3LC)^{-1} - (2R)^2(3L)^{-2}$, and $r = -R(6L^2C)^{-1} - (2R)^3(3L)^{-3}$.

The final form of the solution to Eq. (A3) may now be written as

$$v(t) = Ae^{-\alpha t} + e^{-\beta t}(B\cos\omega t + C\sin\omega t). \tag{A6}$$

To evaluate the unknown constants A, B, and C, we need three initial conditions. These initial conditions are found as follows

(i) initial voltage $v(0) = 0$;

(ii) taking the derivative of Eq. (A1), eliminating the term di_c/dt in Eq. (A2), and setting $v(0) = 0$, we obtain $dv/dt(0) = 0$; and

(iii) taking the second derivative of Eq. (A1) and the derivative of Eq. (A2), eliminating the term d^2i_c/dt^2, and setting $v(0) = 0$, $dv/dt(0) = 0$, and $i_c(0) = I_0$, we obtain $d^2v/dt^2(0) = RI_0/LC$.

We now obtain the final solution using the above initial conditions as

$$v(t) = \frac{I_0R}{LC[(\alpha - \beta)^2 + \omega^2]}$$
$$\times (e^{-\alpha t} - e^{-\beta t}\{\cos\omega t - [(\alpha - \beta)/\omega]\sin\omega t\}). \tag{A7}$$

[1] E. M. Honig, in *Opening Switches*, edited by A. Guenther, M. Kristiansen, and T. Martin (Plenum, New York, 1987), pp. 1–48, and references therein.

[2] M. J. Rhee and R. F. Schneider, IEEE Trans. Nucl. Sci. NS-30, 3192 (1983).

[3] E. A. Chauchard, C. C. Kung, C. H. Lee, M. J. Rhee, and V. Diadiuk, IEEE Trans. Plasma Sci. PS-15, 70 (1987).

[4] See, for example, W. H. Hyat, Jr. and J. E. Kemmerly, *Engineering Circuit Analysis*, 2nd ed. (MaGraw-Hill, New York, 1978), pp. 158–162.

[5] R. J. Adler. *Pulse Power Formulary* (North Star Research, Albuquerque, NM, 1989), pp. 4–14.

[6] See, for example, S. Ramo, J. R. Whinnery, and T. Van Duzer, *Fields and Waves in Communication Electronics*, 2nd ed. (Wiley, New York, 1984), pp. 216–222.

EXPERIMENTAL INVESTIGATION OF
PSEUDOSPARK-PRODUCED ELECTRON BEAMS

K. K. Jain and M. J. Rhee

Laboratory for Plasma Research

University of Maryland

College Park, MD 20742 U. S. A.

Abstract

The pseudospark discharge which produces pulsed electron beams of interesting characteristics has been studied. The multigap pseudospark chamber filled with argon gas is operated at voltages up to 50 kV. The electron beams of peak current $\sim$150 A and pulse duration $\sim$20 ns for $C_{ext} = 980$ pF at repetitive frequency up to 1 kHz are extracted. A study of the empirical scaling law for the electron beam with various experimental parameters is carried out. The normalized rms emittance of the electron beam, measured by a slit-hole technique, is $\sim$15 mm-mrad, yielding a normalized brightness of $B_n \sim 2 \times 10^{10}$ A/m^{2}rad^2.

1 INTRODUCTION

In recent years, pseudospark discharge has received a significant attention because of its ability to sustain anomalous current density in low pressure region of the Paschen curve[1], gas breakdown (conduction) in nanosecond time scale[2] and production of high brightness electron beams.[3,4] As a result, the pseudospark opens a wide field of applications such as in accelerator, free electron laser and high voltage, high current switch technology.

The pseudospark discharge may be characterized as a gas discharge between a planar anode and a hollow cathode in the lower pressure side of the characteristic breakdown curve, which is very similar to the Paschen curve for parallel electrodes. The pseudospark chamber consists of a hollow cathode separated from a planar anode by an insulator in the outer region. The key features of the pseudospark are that although it operates in low pressure region (unlike spark), gas breakdown takes place in fast time scale and sustains large current density, like in a spark. During the breakdown phase, generation of a short duration, pinched electron beam has been observed.
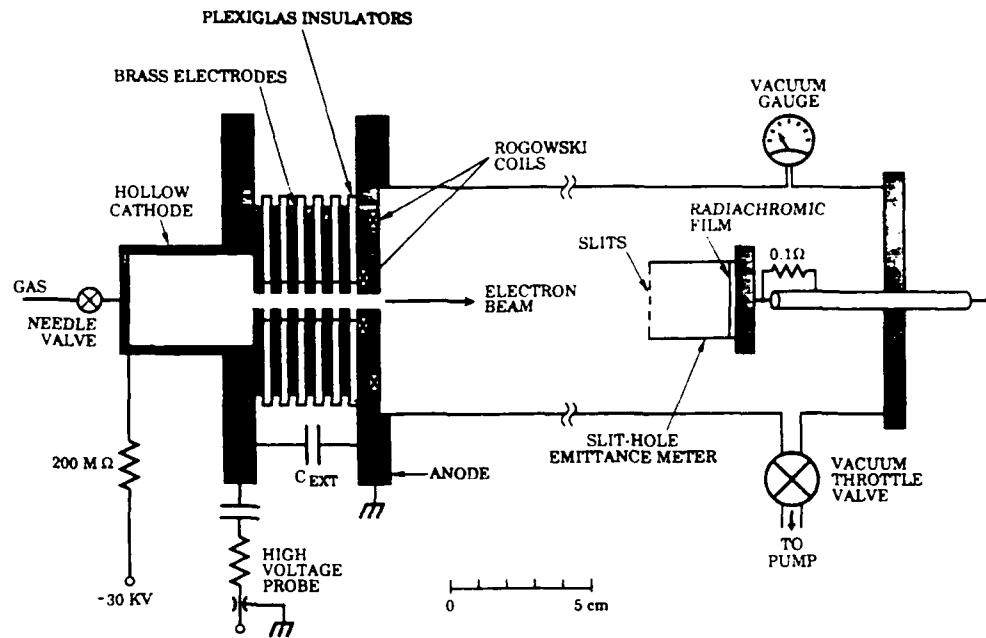
Figure 1: Schematic of the experimental setup

We present here experimental results of an investigation of electron beams produced by a pseudospark with reference to its ability to produce high current, high quality beams. Discharge and electron beam parameters and their scaling behavior are determined.

2 EXPERIMENTAL SYSTEM

The experimental setup[3,4] is schematically shown in Fig. 1. The pseudospark system used in this study is a modular, multigap discharge chamber, consists of a hollow cathode, intermediate brass electrodes and insulating plexiglas disks, and an anode. The intermediate electrodes have a center hole of 3.2 mm diam which provides a channel for the discharge and also passage for the electron beam. The electron beam is extracted through anode hole of 3.2 mm. Experiments have been carried out with 1, 3, 6, and 10 gap systems. Negative high voltages up to 50 kV are applied to the cathode via a 200 MΩ current limiting resistor. In addition to the self-capacitance of the chamber, the total discharge capacitance was increased by adding various values of external capacitance to investigate the discharge and beam characteristics with different stored energies. A 6.3 cm diam, 50 cm long drift chamber is attached to the anode side of the discharge chamber to accomodate diagnostics such as a Fara-
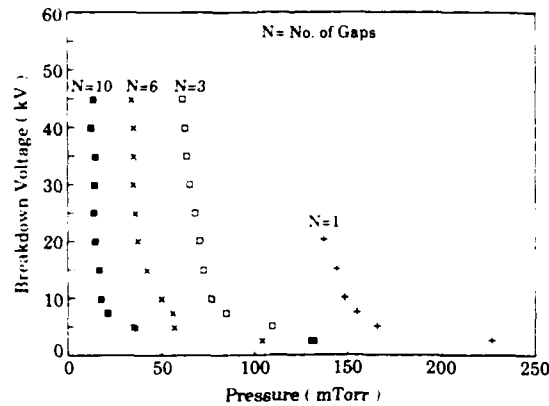
Figure 2: Measured characteristic breakdown curve for four different gap systems.

day cup and an emittance meter. The pseudospark chamber and the drift tube are evacuated to less than 10^{-5} Torr pressure by a diffusion pump. The argon working gas is fed through a needle valve and nearly static gas pressure is maintained in the experimental system by adjusting the needle valve and the throttle vacuum valve. The operating gas pressure range is between 20 and 250 mTorr.

Two calibrated miniature Rogowski coils around the center hole are built into the anode flange. The coil facing the cathode side (upstream) measures the total discharge current while the other coil (downstream) measures electron beam current ejected into the drift chamber. The cathode voltage is measured by a capacitively coupled resistive voltage divider. A movable 100 mΩ Faraday cup of 5 cm diam is inserted on-axis to determine the electron beam current at various axial positions. The rms emittance of the electron beam is obtained using a slit-hole type emittance meter. It consists of an array of seven parallel slits of 300 μm width and a 50 μm thick radiachromic film as a beam detector, placed 47 mm downstream of the slit plane. The slits sample the beam at the given slit locations producing flat beamlets. The beamlets are then allowed to disperse with their transverse velocity after passing through the slits. The spatial current density profiles of dispersed beamlets at the detector plane are recorded on the radiachromic film, from which the rms emittance of the electron beam is analyzed.
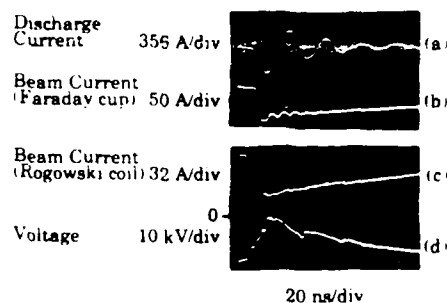
Figure 3: Temporal evolution of the six-gap pseudospark discharge: (a) discharge current (upstream coil) 356 A/div, (b) Faraday cup output (1 cm away from the anode) 50 A/div, (c) injected electron beam current (downstream coil) 32 A/div, (d) cathode voltage signal 10 kV/div.

3 EXPERIMENTAL RESULTS AND DISCUSSIONS

The breakdown voltage characteristics of the pseudospark chamber is determined for various number of gaps. In Fig. 2 the breakdown voltage V_b is plotted as a function of pressure for four different number of gaps. It is evident from this result that the breakdown voltage is an approxiamte function of pd, $V_b \approx f(pd)$, where d, which is proportional to the number of gaps, is the distance between the cathode and anode. Repetitive pulse discharges are easily attained with a time period τ of which is approximately determined by $\tau = RC\ell n(V_0/(V_0 - V_b))$. By choosing an RC value properly, periodic pulse discharges with a frequency of 1 Hz to 1 kHz are obtained.

The temporal behavior of the single pulse discharge of the six-gap pseudospark chamber with $C_{ext} = 380$ pF and $V_b = -24$ kV is shown in Fig. 3. The discharge process occurs in two stages. Up to ~15 ns, the cathode voltage drops slowly, and the currents measured by Rogowski coils and Faraday cup are small. At ~15 ns, the main breakdown occurs. The cathode voltage drops to almost zero and the currents rise very fast to large values within a fast time scale. The discharge current shows a damped oscillating waveform with a peak value of 570 A. The measured electron beam current is ~ 100 A in Fig. 3. The beam current density, estimated assuming beam diam equals to the anode hole opening, is 1.4 kA/cm². Typically, 10 to 20% of the peak discharge current appears as the electron beam current. The beam-induced plasma current appears to be contributing to the downstream Rogowski
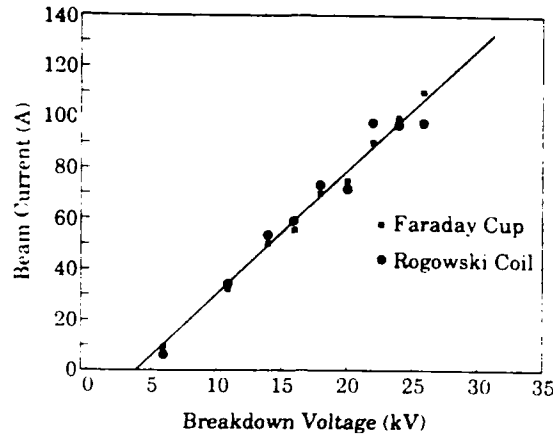
Figure 4: Dependence of electron beam current measured by the downstream Rogowski coil and Faraday cup with breakdown voltage for six-gap pseudospark (C_{ext} = 380 pF).

coil and Faraday cup signals later in time, thus leading to their slow decay.

The dependence of the electron beam current measured by the downstream Rogowski coil as well as Faraday cup (located at 1 cm away from the anode) as a function of breakdown voltage is illustrated in Fig. 4 for C_{ext} = 380 pF and for six-gap chamber. The electron beam current increases linearly with the breakdown voltage up to 25 kV and has a slope of $\sim$ 5 A/kV. For a fixed breakdown voltage, the electron beam current increases with C_{ext} and the beam currents up to a few kA are extracted out of the anode hole. Higher values of C_{ext} also lead to increase of duration of the electron beam current pulse.

The rms emittance[5] (or effective emittance), which is a measure of beam quality, is determined using a slit-hole type emittance meter with the analysis technique described in Refs. 4 and 6. The rms emittance of the electron beam is found to be $\epsilon \sim 65$ mm-mrad. The calculated normalized emittance $\epsilon_n = \beta\gamma\epsilon$ at beam energy of 20 keV is $\sim$ 18 mm-mrad. Thus, the normalized beam brightness can be obtained from the expression $B_n = 2I/\pi^2\epsilon_n^2$ which is $\sim 2 \times 10^{10}$ A/m^{2}rad^2 and compares favorably with that of other high brightness electron beam sources.

4   CONCLUSIONS

The behavior of a multigap pseudospark system and electron beam produced are studied. The pseudospark discharge occurs reproducibly at the pressure and voltage

defined by the lower pressure side of the characteristic breakdown curve. The breakdown voltage is a function of pd, where d is the distance between the cathode and anode. During the breakdown phase, the pseudospark ejects high current density electron beams. An electron beam of average energy of 20 keV, pulse duration ~ 10 ns and of peak current ~ 150 A is obtained for $C_{ext} = 980$ pF. The beam current increases with the breakdown voltage up to 25 kV and with the external capacitance. Approximately 20% of the stored electrical energy appears as the total beam energy. The time-integrated rms emittance of the electron beam, measured using a slit-hole method, is ~ 65 mm-mrad. The normalized brightness of the beam is estimated to be $B_n \sim 2 \times 10^{10}$ A/m^{2}rad^2, which compares favorably with that of existing high-brightness sources. Thus, the pseudospark appears to be a simple , compact, high-brightness electron beam source.

ACKNOWLEDGMENTS

REFERENCES

1. Christiansen, J. and Schultheiss, C., Z. Phys. A 290, 35 (1979).
2. Choi, P., Chauqui, H. H., Favre, M. and Wyndham, E. S., IEEE Trans. Plasma Sci. PS-15, 428 (1987).
3. Boggasch, E. and Rhee, M. J., Appl. Phys. Lett. 56, 1746 (1990).
4. Jain, K. K., Boggasch, E., Reiser, M. and Rhee, M.J., to appear in Phys. Fluids B 2 (10), (1990).
5. Lapostolle, P. M., IEEE Trans. Nucl. Sci. NS-18, 1101 (1971).
6. Rhee, M. J. and Schneider, R. F., Part. Accel. 20, 133 (1986).

Experimental investigation of

a pseudospark-produced high-brightness electron beam

K. K. Jain, E. Boggasch,[a] M. Reiser, and M. J. Rhee

Laboratory for Plasma Research

University of Maryland, College Park, Maryland 20742

ABSTRACT

A high-brightness electron beam produced by a six-gap pseudospark chamber operated in 5 - 25 kV voltage and 30 - 70 mTorr pressure ranges is experimentally investigated. The electron beam of current 150 A at an average energy of 20 keV and pulse duration of 10 ns is extracted with a repetitive frequency of ~10 Hz. The electron beam current scales linearly with the breakdown voltage and about 20 % of the stored energy is converted into the total beam energy. The time-integrated rms emittance of the electron beam is measured, and a typical value is found to be 65 mm mrad, yielding a normalized brightness of the beam $B_n \approx 2 \times 10^{10}$ $A/(m^2 rad^2)$.

a) Present address: Max-Planck Institut für Quantenoptik, D-8046 Garching; GSI-Darmstadt, D-6100, Darmstadt, F.R.G.

I. INTRODUCTION

High-current and low transverse-energy-spread electron-beam sources are required in advanced accelerators such as e^-e^- linear colliders[1] and free-electron lasers.[2,3] Thermionic cathodes produce electron beams of relatively low transverse velocity-spread; however, the current density is limited[4] to less than 100 A/cm^2 and nonuniformity of the charge distribution may cause significant emittance growth.[5] On the other hand, field emission diodes are capable of producing high current-density electron beams but usually have high energy spread. Strong magnetic fields are often used to guide such a beam[6] to reduce the beam spreading. Use of strong magnetic fields, however, has disadvantages,[7] such as rippling of the beam surface, undesirable beam instabilities, etc.

The limitations of presently available sources have motivated a search for new types of electron beam sources such as photocathodes[8] that can produce a beam of high brightness. In recent years,[9-11] the pseudospark device has been found to be capable of generating electron beams of high current density (> 1 kA/cm^2) and high-brightness. The breakdown voltage between two parallel electrodes as a function of gas pressure is described by the well-known Paschen curve. However, if the planar cathode is replaced by a hollow cathode, the discharge characteristics are changed: the breakdown voltage curve is slightly modified from the Paschen curve in the region between

the Paschen minimum and vacuum breakdown.[11-13] The discharge mechanism, in this region, is different from that of a high pressure spark, but the breakdown time is comparable; this is why it is called a "pseudospark." A single-gap pseudospark chamber consists of a hollow cathode and an anode. Normally, for breakdown in the lower pressure side of the Paschen minimum, the longer discharge path is preferred, which in the case of pseudospark geometry is along the axis. The hold-off voltage of a single-gap is limited to ~50 kV due to onset of surface flashover;[14] however this can be increased by additional stacks of intermediate electrodes and insulator disks between the anode and the cathode. Thus, a multi-gap pseudospark chamber can be operated at higher voltages.

During the breakdown phase, the generation of a short duration, pinched electron beam has been observed. Until now, the understanding of the mechanism of electron beam generation has been merely qualitative. During the pre-breakdown phase, electrons and ions are created by ionization. The electrons are immediately collected by the anode while the positive charges move toward the cathode and mainly into the hollow region of the cathode, forming a virtual anode. In the breakdown phase, a fast carrier multiplication process[9] inside the virtual anode leads to a high plasma density, which is followed by a very fast breakdown, discharging the system. The field distribution between virtual anode, cathode, and anode favors the formation of a pinched electron beam[13] directed toward the anode.

3

In this paper, we report results of an investigation of an electron beam produced by a pseudospark with reference to its ability to produce high-current, high-quality beams. Detailed experimental studies are performed to determine the electrical parameters of the beam and its scaling behavior. The rms emittance of the electron beam is measured and then the brightness is analyzed. In Sec. II, the experimental device and associated diagnostics used are described. Results and discussions are presented in Sec. III. The main results of the experimental study are concluded in the last section.

II. EXPERIMENTAL ARRANGEMENT

Figure 1 shows a schematic of our experimental setup.[10] The pseudospark chamber consists of an easy-to-change, O-ring seal, modular, six-gap electrodes, and insulator disks stacked between a hollow cathode and an anode. The anode has a 3.2 mm-diam, on-axis hole for the beam extraction. Intermediate electrodes made of 3.2 mm-thick brass have outer diam of 6.35 cm and a center hole of diam 3.2 mm. The 3.2 mm thick plexiglas insulator disks have outer and inner diam's of 7.0 cm and 2.54 cm, respectively. In addition to the self capacitance of 11 pF of the chamber between cathode and anode, a low inductance, external capacitance of 380 pF, 760 pF, or 980 pF is added to investigate the beam behavior with different stored energies. Negative high voltage up to 30 kV is applied to the hollow cathode via a 200 MΩ charging resistor. A 50 cm-long drift tube is attached to the anode side for beam propagation and to accomodate diagnostics,

such as a Faraday cup and an emittance meter.

A mechanical pump evacuates the experimental system down to
about 1 mTorr. The pressure is measured by a capacitance
manometer type vacuum gauge. The argon working gas is fed
through a needle valve, from the cathode side, into the system.
The operating pressure range is between 30 to 70 mTorr. Two
calibrated Rogowski coils are molded into axisymmetric grooves
milled into both sides of the anode flange. The coil facing the
cathode side (upstream coil) measures the total discharge
current, while the other coil facing the drift chamber
(downstream coil) measures the electron beam current (or net
current) passing through the anode hole into the drift chamber.
The cathode voltage is measured by a high-impedance resistive
voltage probe. A movable 100 mΩ Faraday cup of 5 cm-diam
graphite is inserted on-axis through the end flange of the drift
tube to measure the electron beam current at various axial
positions as it propagates in the drift tube.

The rms emittance of the pseudospark-produced electron beam
is measured using a slit-hole type emittance meter.[15] It
consists of a series of parallel thin slits of 300 μm width and 2
mm spacing, constructed from a 0.6 mm thick stainless steel
plate. These slits produce sheet beamlets which are detected by
a radiachromic film[16] placed 47 mm farther downstream. The film
material gives a linear response up to an absorbed dose of 10^8
rad. By use of an applied magnetic field it is found that the
response pattern on the film is completely swept away, assuring

5

that UV or other light, for which the film is also sensitive, produced in the experiment does not contribute to the film response. The resulting spatial density distribution on the film is scanned by an optical microdensitometer and the emittance is analyzed.

III. MEASUREMENTS, RESULTS, AND DISCUSSION

A. Breakdown and beam characteristics

The electrical breakdown characteristic of the pseudospark chamber is measured by fixing the charging voltage to a certain value, and slowly increasing the gas pressure, until breakdown occurs. Nearly static gas pressure is maintained in the experimental system by adjusting the needle valve and throttle vacuum valve, as shown in Fig. 1. The measured breakdown-voltage V_b is plotted as a function of pressure in Fig. 2, which shows that the breakdown voltage is a sensitive function of pressure in the 30 - 45 mTorr range. Having an RC time constant of a fraction of a second, a periodic pulse discharge at 1 - 15 Hz can be easily attained. The frequency of discharge can be adjusted by either changing the charging voltage V_o, the gas pressure, or both.

The temporal evolution of the discharge is shown in Fig. 3 for a breakdown voltage of $V_b = -24$ kV and $C_{ext} = 380$ pF. All the signals show that the discharge process occurs in two stages. For the first 15 ns, the discharge voltage drops slowly from -24

6

kV to -22 kV, and the discharge and electron beam currents are small (less than 10 % of the peak value). At around 15 ns, the main breakdown occurs. The discharge voltage drops from -22 kV to almost zero in the next 20 ns. During this period, the discharge and the electron beam current start rising to a large value. The discharge current shows a damped oscillating waveform. The downstream Rogowski coil and the Faraday cup (located at 1-cm away from the anode) register only one negative peak at the time of discharge current maximum. The peak discharge current in Fig. 3(a) is 570 A. The measured electron beam current is ~100 A at V_b = 24 kV and C_{ext} = 380 pF. The beam current density at the source exit is estimated: assuming a beam diam of 3.2 mm (anode hole opening), the observed beam current of 100 A yields the beam current density of 1.4 kA/cm^2. Typically, 10 to 20 % of the total discharge current appears as electron beam current. Perhaps beam-induced plasma current is contributing to the downstream Rogowski coil and Faraday cup signals later in time, thus leading to their slow decay. Measurements of the beam current as it propagates in the drift tube are done with a movable Faraday cup. In Fig. 4(a), the peak value of the beam current is plotted as a function of axial distance from the anode, showing exponential decay.

The dependence of electron beam current as a function of breakdown voltage is determined and shown in Fig. 5 for C_{ext} = 380 pF. The electron beam current increases linearly with the voltage and has a slope of ~5 A/kV. It is observed that the higher values of C_{ext} lead to increase in both the duration and

7

amplitude of the beam current. The beam current roughly scales as the square root of C_{ext}. The beam current scales linearly with the breakdown voltage for all values of C_{ext}'s used. The efficiency of the electron beam generation by the pseudospark may be defined here as

$$\eta = \int V_b I \, dt / \tfrac{1}{2} C_{ext} V_b^2, \tag{1}$$

and is found to be nearly 20 % in the case of C_{ext} = 380 pF.

B. Emittance measurement

The rms emittance[17,18] or effective emittance,[5] defined as

$$\epsilon = 4(\langle x^2 \rangle \langle x'^2 \rangle - \langle xx' \rangle^2)^{1/2}, \tag{2}$$

is a figure of merit for the beam quality. In Eq. (2), x' is the gradient of the particle trajectory given by $x' = dx/dz = P_x/P_z$ and the angular brackets denote average values over the two-dimensional phase-space as

$$\langle \varphi \rangle = \int \varphi \, \rho(x,x') dx dx' , \tag{3}$$

where $\rho(x,x')$ is the projected density in the two-dimensional phase-space. The second moments of this distribution, $\langle x^2 \rangle$,

$<x'^2>$, and $<xx'>$, are related to the beam width, the velocity spread, and the beam divergence, respectively.

Various experimental methods[18,20] have been used to measure the beam emittance, such as two-slit, hole-slit, and hole-hole. Under the assumption of a Maxwellian transverse velocity distribution and an axisymmetric, nonrotational beam, a simple slit-hole type emittance meter has recently been suggested.[15]

In our experiment, we have used a slit-hole type emittance meter with the analysis technique described in Ref. 15 to determine the pseudospark-produced electron beam emittance. The electron beam is allowed to pass through an array of seven thin slits. The slits are long (in the y direction) as compared to the beam dimension and thin (in the x direction). Thus, the slits integrate over all velocity distributions in the y direction while the velocity distribution in the x direction is determined. The transmitted sheet beamlets formed by the slits are then allowed to traverse a field-free region of 4.7 cm in length before they strike a thin radiachromic film. A shutter (which is not shown in Fig. 1) blocks the beam path after a few discharges when the darkening profile on the film due to the beam is just visible: the peak value of optical density of the profile is kept under 0.5, which insures that the film response is linear.

To obtain the rms emittance of the beam, we scan the optical density profile of sheet beamlets as recorded on the film along

the line of $y = 0$ by a microdensitometer. A typical measured

density profile as a function of radial position r (or x) is

shown in Fig. 6. In order to simplify the emittance analysis as

described in Ref. 15, the measured density profile of each

beamlet is approximated as a Maxwellian. Ideally, infinitely

thin slits should be used in the emittance meter to directly

obtain the mean diverging angle α_i, the peak density β_i, and the

rms width σ_i of the individual profile, where i denotes the ith

slit. In the experiment, however, a finite slit width of 0.3 mm

is used to obtain the beamlet's profile, which is subject to

deviation from the true profile of the beam distribution. We

have derived a method of correcting the rms width and the peak

height of the density profile produced by the finite-width slit.

In this method, the density profile on the detector plane is

considered as a superposition of profiles of beamlets which are

produced by infinitely thin slits distributed continuously across

the finite width of the slit. If one assumes that the beam has a

Maxwellian velocity distribution and its intensity remains

constant (or a very weak function of x) within the slit width 2w,

the resulting profile for the ith sheet beamlet is found as

$$D_i(x) = \beta_i \int_{(x-w)/L}^{(x+w)/L} \exp[-\tfrac{1}{2}(x'/\sigma_i)^2]\ dx'$$

$$= (\pi/2)^{1/2}\beta_i\sigma_i[\mathrm{erf}(\frac{x+w}{s_i}) - \mathrm{erf}(\frac{x-w}{s_i})], \qquad (4)$$

where x is the distance measured from the ith slit position,

10

$erf(x) = 2/\sqrt{\pi} \int_{0}^{x} exp(-u^2)du$, and $s_i = \sqrt{2}\sigma_i L$. It is noted

that for an ideal case as $w \rightarrow 0$, Eq. (4) reduces to

$2w\beta_i L^{-1} exp[-\frac{1}{2}(x'/\sigma_i)^2]$, which is $2w/L$ times the original

distribution. Given the peak value of measured profile $D_i(0)$,

one can find the β_i as

$$\beta_i = D_i(0)/[(2\pi)^{1/2}\sigma_i \ erf(\frac{w}{\sqrt{2}\sigma_i L})]. \tag{5}$$

The difference of the two error functions inside the bracket [ ]

in Eq. (4) determines the shape of the resulting profile as a

function of x for two parameters w and $s_i = \sqrt{2}\sigma_i L$. The full-

width at half-maximums (FWHM's) of Eq. (4) are numerically

calculated for various values of w/L and σ. The σ as a function

of measured FWHM (normalized to L) with a parameter w (normalized

to L) is plotted as shown in Fig. 7. Thus, one can find σ_i in

terms of measured FWHM of the ith beamlet, knowing the slit width

w used. The height of the beam distribution β_i is then found

from Eq. (5) using the obtained value of σ_i. A general method

which can be applicable to other beam distributions is derived

and will be treated elsewhere. Analytical expressions of $\alpha(r)$,

$\beta(r)$, and $\sigma(r)$ are found by curve fitting the discrete values of

α_i, β_i, and σ_i, respectively.

Numerical integrations are then performed using the

expressions of $\alpha(r)$, $\beta(r)$, and $\sigma(r)$ to find   and the moments .

$<x^2>$, $<x'^2>$, and $<xx'^2>$ (see Ref. 15 for details). The rms

emittance given by Eq. (3), with the obtained moments at an axial

11

distance of 9 cm from the anode, is found to be

$$\epsilon = 65 \text{ mm mrad} . \qquad (6)$$

The normalized rms emittance $\epsilon_n = \beta \gamma \epsilon$ (where $\beta = v/c$, $\gamma = (1-\beta^2)^{-1/2}$, v is the beam velocity, c is the velocity of light) is used for comparing the beam quality at different energies. With an average beam energy of 20 keV, the calculated normalized emittance ϵ_n is ~18 mm mrad. Once the emittance and the beam current are determined, the normalized beam brightness can be calculated from the expression[2,5,21]

$$B_n = \frac{2I}{\pi^2 \epsilon_n^2} . \qquad (7)$$

For measured beam current of 32 A at 9 cm axial distance from the anode for this set of experiments,

$$B_n = 2 \times 10^{10} \text{ A/(m}^2 \text{ rad}^2), \qquad (8)$$

which compares favorably with that of other high-brightness sources. Further, assuming a Maxwellian transverse velocity distribution with an rms velocity $v_{rms} = (kT/m_o)^{1/2}$ in the transverse direction, the normalized emittance at the source can be written as $\epsilon_n = 2r_s(kT/m_o c^2)^{1/2}$, where r_s is the electron beam source radius and T is the temperature. Assuming the same value of $\epsilon_n = 18$ mm mrad at the source and with beam radius of 1.6 mm, an approximate electron beam temperature of 15 eV is obtained.

The electron beam profile and its emittance are determined

at different axial distances from the anode with the help of a movable emittance meter. By fitting the optical density peaks of the beamlets recorded on the film to a Gaussian profile, the rms radius of the beam is obtained as shown in Fig. 4(b). The beam radius increases from 2.2 mm to 5.0 mm during its propagation over an axial distance of 15 cm. The measured dependence of emittance on axial distance from the anode is plotted in Fig. 4(c). This observed increase of the beam emittance as it propagates may be due to the nonlinear space-charge effect.

The calculated value of ε from the measurements is used to obtain isodensity contours of $\varepsilon(x,x')$ in x-x' space (known as an emittance plot) and is shown in Fig. 8 for the breakdown voltage of 20 keV and at an axial distance of 15 cm from the anode. It is interesting to note from Fig. 8 that the emittance plot shows slightly S-shaped contours (non-elliptical) which is indicative of the existance of nonlinear forces on the beam, again perhaps due to the strong nonlinear space-charge field[5] of the beam.

IV. CONCLUSIONS

We have studied the characteristics of a pseudospark-produced electron beam. The pseudospark discharge takes place at the lower pressure side of the Paschen minimum in the characteristic breakdown curve. The main pseudospark discharge occurs after some time-delay. During the breakdown phase, the pseudospark discharge ejects an electron beam of average energy 20 keV, peak current 150 A, and pulse duration ~10 ns. The observed current

corresponds to beam current density greater than 10^3 A/cm^2 (at the anode exit), which is an extremely high value at such a modest beam energy of 20 keV. Approximately 20 % of the stored electrical energy appears as the total beam energy. The time-integrated rms emittance of an electron beam is measured using a slit-hole method. An rms emittance of value ~ 65 mm mrad is found at an axial distance of 9 cm from the anode. The normalized brightness of the beam is then estimated as $B_n \approx 2 \times 10^{10}$ A/(m^2 rad^2), which compares favorably with that of existing high-brightness sources. The electron beam current scales linearly with the breakdown voltage as 5 A/kV. This is a very encouraging result, suggesting that the electron beam brightness may further increase at higher voltage operation of the pseudospark. Thus, the pseudospark appears to be a simple, compact, high-brightness, electron-beam source.

ACKNOWLEDGMENTS

REFERENCES

1. R. Stiening, in <u>Proceedings of the 1987 IEEE Particle Accelerator Conference</u>, edited by E. R. Lindstrom and L. S. Taylor (IEEE, New York, 1987), p. 1.

2. C. W. Roberson and P. A. Sprangle, Phys. Fluids B <u>1</u>, 3 (1989).

3. T. J. Kwan and C. M. Snell, Phys. Fluids <u>26</u>, 835 (1983).

4. R. B. Miller, <u>An Introduction to the Physics of Intense Charged Particle Beams</u> (Plenum Press, New York, 1982), p. 34.

5. M. Reiser, in <u>Proceedings of the 1989 Workshop on Advanced Accelerator Concepts</u>, AIP Conference Proceedings 193, edited by C. Joshi (AIP, New York, 1989), p. 311.

6. M. L. Sloan and H. A. Davis, Phys. Fluids <u>25</u>, 2337 (1982); R. L. Sheffield, M. D. Montgomery, J. V. Parker, K. B. Riepe, and S. Singer, J. Appl. Phys. <u>53</u>, 5408 (1982).

7. D. A. Kirkpatrick, R. E. Shefer, and G. Bekefi, J. Appl. Phys. <u>57</u>, 5011 (1985).

8. R. L. Sheffield, Nucl. Instrum. & Methods A <u>272</u>, 222 (1988).

9. J. Christiansen and C. Schultheiss, Z. Phys. A <u>290</u>, 35 (1979).

10. E. Boggasch, T. A. Fine, and M. J. Rhee, in <u>Proceedings of the 1989 IEEE Particle Accelerator Conference</u>, edited by F. Bennett, J. Kopta (IEEE, New York, 1989), p. 316; E. Boggasch and M. J. Rhee, Appl. Phys. Lett. <u>56</u>, 1746 (1990).

11. P Choi, H. H. Chuaqui, M. Favre, and E. S. Wyndham, IEEE Trans. Plasma Sci. <u>PS-15</u>, 428 (1987).

12. D. Bloess, I. Kamber, H. Riege, G. Bittner, V. Brückner, J. Christiansen, K. Frank, W. Hartmann, N. Lieser, C. Schultheiss, R. Seeböck, and W. Steudtner, Nucl. Instrum. & Methods <u>205</u>, 173 (1983).

13. W. Benker, J. Christiansen, K. Frank, H. Gundel, W. Hartmann, T. Redel, and M. Stelter, IEEE Trans. Plasma Sci. <u>17</u>, 754 (1989).

14. C. Schultheiss, Nucl. Instrum. & Methods A <u>254</u> , 398 (1987).

15. M. J. Rhee and R. F. Schneider, Part. Accel. <u>20</u>, 133 (1986).

16. W. L. McLaughlin, R. M. Uribe, and A. Miller, Radiat. Phys. Chem. <u>22</u>, 333 (1983).

17. P. M. Lapostolle, IEEE Trans. Nucl. Sci. <u>NS-18</u>, 1101 (1971).

18. C. Lejeune and J. Aubert, in <u>Applied Charged Particle Optics</u>, edited by A. Septier (Academic, New York, 1980), Part A, p. 198.

19. J. D. Lawson, <u>The Physics of Charged Particle Beams</u>, 2nd ed. (Clarendon, Oxford, U. K., 1988), p. 192.

20. A. van Steenbergen, Nucl. Instrum. & Methods <u>51</u>, 245 (1967).

21. A. van Steenbegen, IEEE Trans. Nucl. Sci. <u>NS-12</u>, 746 (1965).

Fig. 1   Schematic of the experimental setup.

Fig. 2.   Measured characteristic breakdown curve.

Fig. 3.   Temporal evolution of the pseudospark discharge:

(a) discharge current (upstream coil) 356 A/div,

(b) Faraday cup output (1-cm away from the anode) 50

A/div, (c) injected electron beam current (downstream

Rogowski coil) 32 A/div,   (d) cathode voltage signal

10 kV/div.

Fig. 4.   Dependence of beam parameters on the axial distance

from the anode: (a) the electron beam current, (b) rms

beam radius, (c) rms emittance.

Fig. 5.   Variation of electron beam currents measured by

the downstream Rogowski coil and Faraday cup with

breakdown voltage (C_{ext} = 380 pF).

Fig. 6.   Optical density distribution on the radiachromic film

after exposure to the sheet beamlets at a 9 cm distance

from the anode.

Fig. 7.   Plot of measured FWHM of the beamlet's optical density

distribution against the rms width of the original

distribution for various values of slit-width w. Here

FWHM and w are normalized to L, the distance between the

film and the slit plane.

Fig. 8.   Two-dimensional isodensity-contour plot of phase-space

density $c(x,x')$.
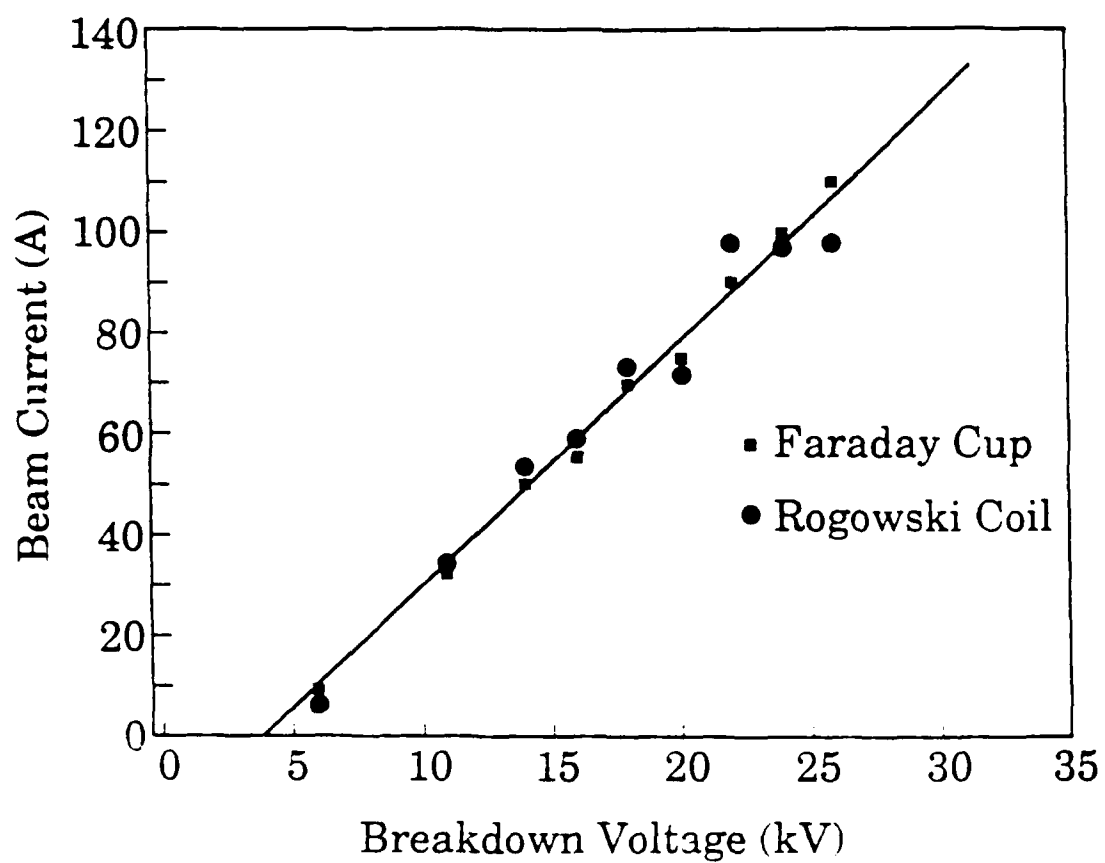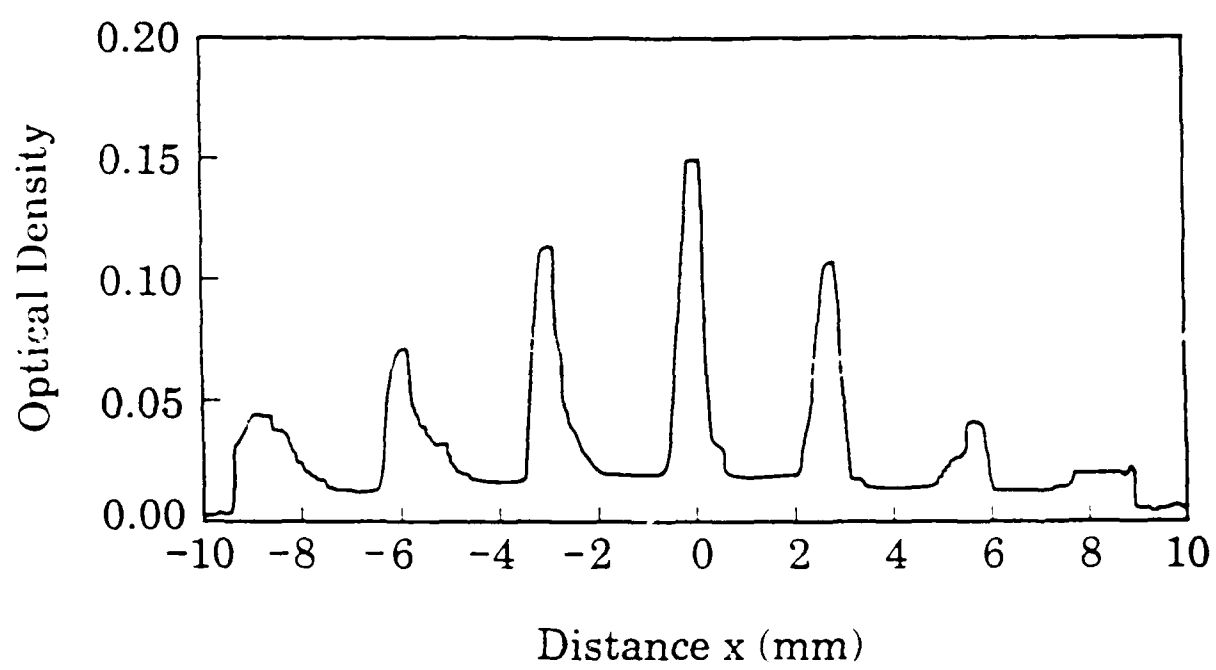
VACUUM GAUGE

VACUUM THROTTLE VALVE

RADIACHROMIC FILM

0.1Ω

TO PUMP

SLITS

SLIT-HOLE EMITTANCE METER

ROGOWSKI COILS

ELECTRON BEAM

ANODE

PLEXIGLAS INSULATORS

BRASS ELECTRODES

C_{EXT}

HIGH VOLTAGE PROBE

HOLLOW CATHODE

GAS

NEEDLE VALVE

200 MΩ

-30 KV

5 cm

0

Fig. 1

Fig. 2

Discharge
Current   356 A/div _____ (a)

Beam Current
(Faraday cup)   50 A/div _____ (h)

Beam Current
(Rogowski coil) 32 A/div _____ (c)

                  0 ⊣
Voltage   10 kV/div _____ (d)

                    20 ns/div

Fig. 3

Fig. 4

Fig. 5

Fig. 6
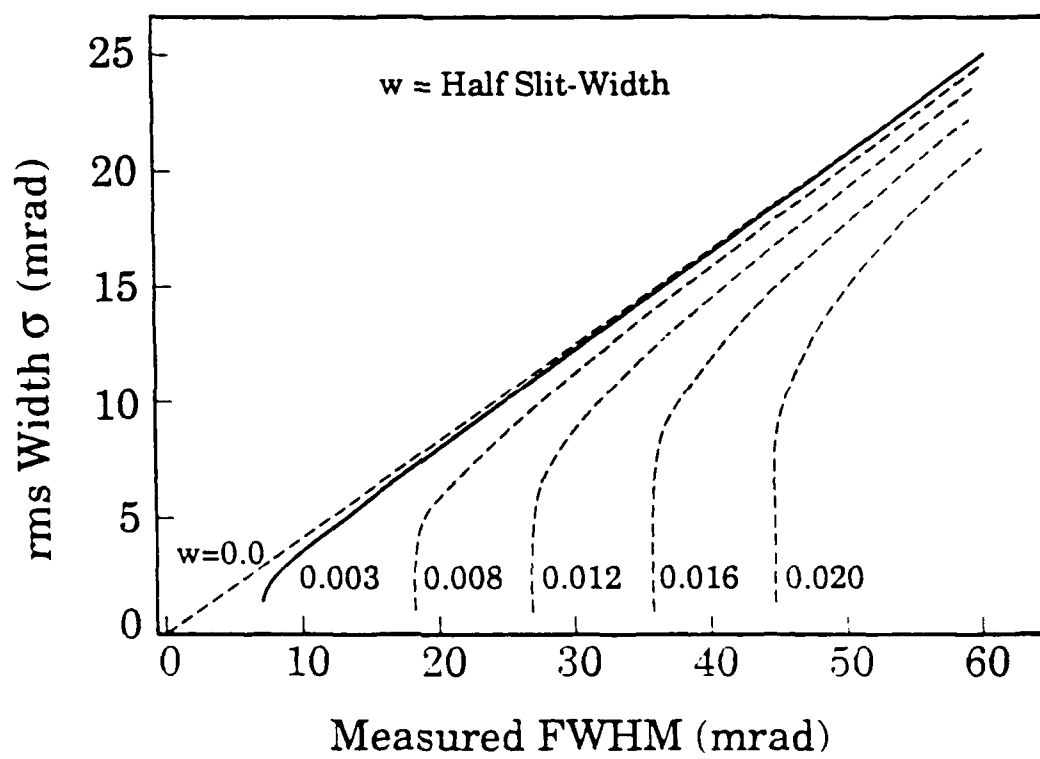
Fig. 7
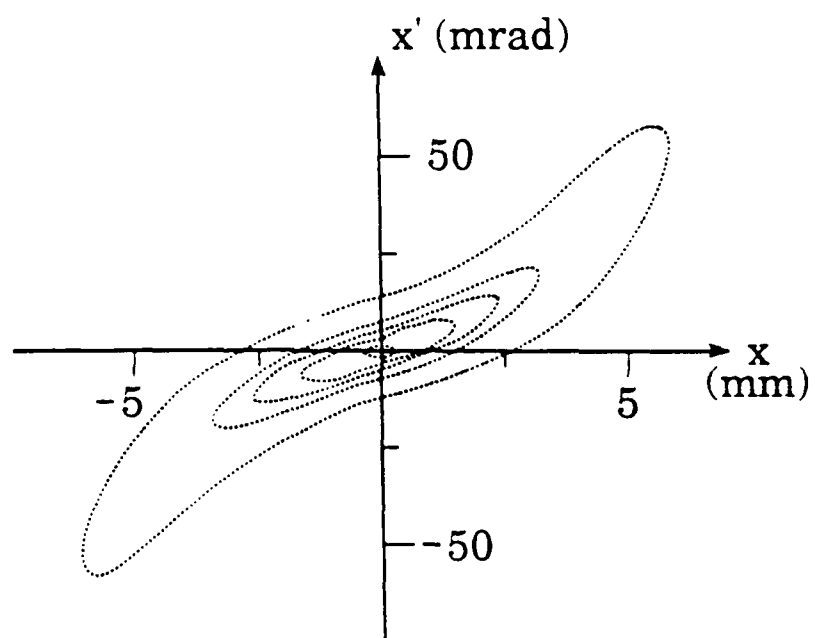
Fig. 8

AIP
CONFERENCE
PROCEEDINGS 195

DENSE
Z-PINCHES

SECOND INTERNATIONAL CONFERENCE

LAGUNA BEACH, CA 1989

EDITORS: NINO R. PEREIRA
JACK DAVIS
NORMAN ROSTOKER

418

EXPERIMENTAL STUDY OF PSEUDOSPARK-PRODUCED ELECTRON BEAMS

E. Boggasch and M.J. Rhee
Laboratory for Plasma Research
University of Maryland, College Park, MD 20742, U.S.A.

ABSTRACT

A brief review on the status of pseudospark research is given. A modular pseudospark chamber was built to investigate this new discharge type as a source of intense electron beams. Typical experimental parameters are a breakdown voltage of 25 kV and a discharge current of about 500 A, with an electron beam of ~100 A and ~10 ns FWHM emitted through the anode hole into a drift chamber. Electrical parameters of the circuit, including the plasma channel, were evaluated by monitoring the discharge current waveform. First results of emittance measurements of the electron beam are presented. Based on the measured rms emittance of ~ 55 mm-mrad, a normalized brightness of about 2×10^{11} A/m^2-rad^2 is estimated. This characterizes the pseudospark as a high brightness electron beam source.

REVIEW OF PSEUDOSPARK MECHANISM AND APPLICATIONS

The "pseudospark" phenomenon was first reported by Christiansen and Schultheiss in 1978[1] as a fast, gas discharge which occurred at low pressure in a special device, called a pseudospark chamber. The breakdown time of this discharge is found to be similar to that of a high pressure spark, although their mechanisms appear to be totally different.[2,3] A single-gap pseudospark chamber consists of an anode with a center hole and a hollow-cathode; the electrodes are separated by a few mm thick insulating washer. The pseudospark chamber may be described as a combination of a restricted linear discharge geometry and a hollow cathode. The breakdown characteristics depend on the operating point on the breakdown curve: fast breakdown occurs at higher voltage (lower pressure). A characteristic breakdown curve similar to the Paschen curve for parallel electrodes is obtained. The pseudospark is initiated on the left side of this breakdown curve. In this regime, the gas discharge occurs along the longest possible path in the gap which, in the case of a pseudospark geometry, is found on the axis. The holdoff capability of one gap is limited to 40 to 50 kV due to the onset of surface flashover and field emission; however, this holdoff voltage can be enhanced by adding additional stacks of intermediate electrodes and insulator discs forming a multigap chamber. Thus the field is graded by the capacitively divided voltage, resulting in a reduced voltage across each gap by the increased number of stacks.

Although the pseudospark phenomenon was discovered more than a decade ago, its mechanisms are still not fully understood. Some of the interesting information was obtained through spectroscopic observations.[2,3]

The discharge starts with a high impedance Townsend predischarge, which lasts for a few microseconds before the main breakdown occurs. During this period a light emitting zone has been observed, starting from the anode and moving towards the cathode with a constant velocity which is measured to be 1 cm/μs in 150 mTorr of

argon gas. The current rises from 10 μA to a few hundred μA until a stationary high voltage glow discharge with constant current is achieved. At this point the light emitting zone becomes stationary at a distance of a few mm in front of the cathode. During the predischarge, a high reduced electrical field strength E/n of over 10^{-14} V cm^2 is produced, resulting in generation of high-energy runaway electrons. This explains the electron emission.through the anode hole during the predischarge. At the same time positive ions drift to the cathode accumulating a positive space charge.

When the positive space charge on axis reaches a critical value at the cathode hole, the hollow cathode discharge is ignited and the main discharge takes place. Ionization waves moving into the hollow cathode at velocities of approximately 100 cm/μs are observed. The light intensity in the gap between the anode and cathode rises and an intense electron beam is ejected at the anode. When the voltage drops, within ~10 ns, current rise rates of up to 8×10^{11} A/s and current densities exceeding 100 kA/cm^2 are observed.[4] These extremely high current densities in a glow discharge are inconsistent with a cold cathode emission process, and are attributed to field enhanced emission from the melted electrode surface.[5]

It is possible to trigger the main discharge in the hollow cathode region with sub-nanosecond jitter, without the long predischarge, when a sufficient amount of charge carriers is provided in the hollow cathode region. This can be achieved either by initiating a surface flash over[6], by providing a pulsed glow discharge[7], or by illumination with UV-light.[8] First numerical simulation results of the pre- and early main discharge phases were reported recently.[9]

As was introduced initially, the pseudospark discharge produces well pinched electron beams with current densities up to 10^6 A/cm^2 and power densities up to 10^9 W/cm^2. Such high-power electron beams can be used for material processing, for example drilling holes in metal targets or evaporation of semiconductors and isolators to produce layers of high temperature superconducting materials.[10] With the emission of the intense electron beam, pulsed microwave[11] and X-ray generation are also observed,[2,12] possibly allowing further applications in these fields in the future.

The pseudospark is easily triggered with high precision in the hollow cathode region. Initially, this behavior favored the development of high power pseudospark switches, first began at CERN.[6] Since then, pseudospark switches for various applications have been developed. Current pulses of up to 200 kA with a jitter of ~100 ns were switched at 0.3 Hz for over 500.000 shots without significant electrode deterioration.[13] With a pseudospark switch designed for a laser system, a jitter of 4 ns at 25 kA peak current and 100 Hz repetition rate were measured.[4] Multichannel pseudospark switches[14] have achieved current rise rates of up to 2.4×10^{12} A/s, with a peak current of 15 kA and a jitter of 1 ns.

EXPERIMENTAL STUDIES AT THE UNIVERSITY OF MARYLAND

An easy to change, o-ring sealed, modular, multigap discharge chamber system with brass electrodes and plexiglas discs was constructed. For the experiments reported here a 6 gap pseudospark chamber with a 3.2 mm diam center hole on axis was used. The experimental setup is shown in Fig. 1.
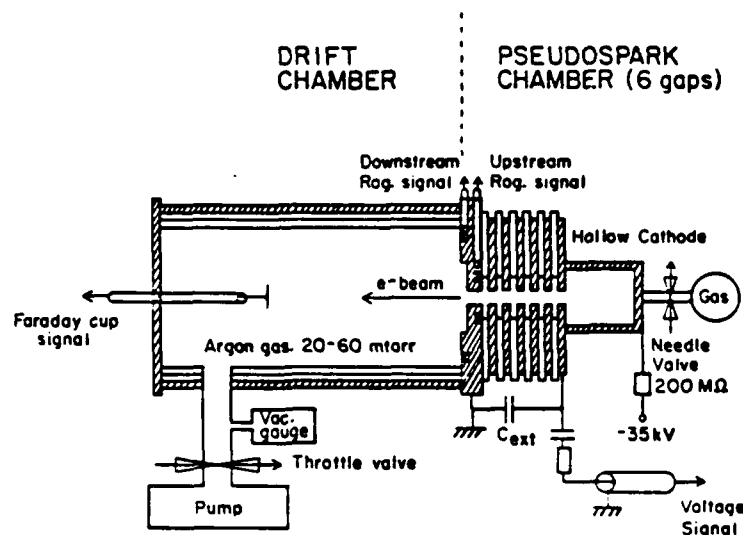
Fig. 1. Experimental set up.

Negative high-voltage up to 35 kV is applied to the hollow-cathode via a 200 MΩ current-limiting resistor. In addition to the self-capacitance of 11 pF of the chamber, the total discharge capacitance was increased by adding external capacitors of 420 pF and 760 pF to investigate the behavior with different stored energies. The chamber was mounted on a plexiglas drift tube of 50 cm length and 6.3 cm diameter. A brass flange which terminated the tube was connected via 6 brass bars equally spaced on a radius of 4.4 cm to the grounded anode, thus providing a current return path.

A two-stage mechanical pump evacuated the assembly to about 1 mTorr. The working gas was usually argon, which was injected through a needle valve from the cathode side into the system. The operating pressure range varied from 20 to 60 mTorr.

Two calibrated miniature Rogowski coils around the center hole were built into the anode flange as can be seen in Fig. 1. The coil facing the cathode side (upstream coil) measured the total current in the discharge channel. The other coil facing the drift chamber (downstream coil) measured the current which passed through the anode hole into the drift chamber. The chamber voltage was measured by a capacitively coupled resistive voltage probe of division ratio 1:20,000 into a 50 Ω load. The risetime of this probe after proper compensation was less than ~400 ps and its RC droop time constant is ~120 ns.

A movable 1 mΩ graphite Faraday cup of 3 cm diam was inserted on axis through the end flange of the drift tube to measure the electron beam current at certain distances downstream of the anode.

A dual beam oscilloscope (Tektronix 7844) allowed for time correlated monitoring of two signals simultaneously.

The emittance of the electron beam was analyzed using a slit-hole type emittance meter.[15] It consisted of an array of seven 200 μm wide and 2mm long slits which were cut into a 0.6 mm thick stainless steel plate. These slits produce sheet beamlets which were detected by a radiachromic film[16] placed 12 mm further downstream. The film material gives linear coloration response up to an absorbed dose of 10^8 rad. By use of an applied magnetic field, it was assured that UV or other light produced in the experiment did not contribute to the film response. The resulting spatial distribution pattern on the film was scanned by a microdensitometer, and the emittance and beam profile were analyzed.[15]

The breakdown characteristic of the discharge chamber was determined by fixing the voltage to a certain value and slowly increasing the pressure until breakdown occurred. In Fig. 2 the breakdown voltage U_B is plotted as a function of pressure.
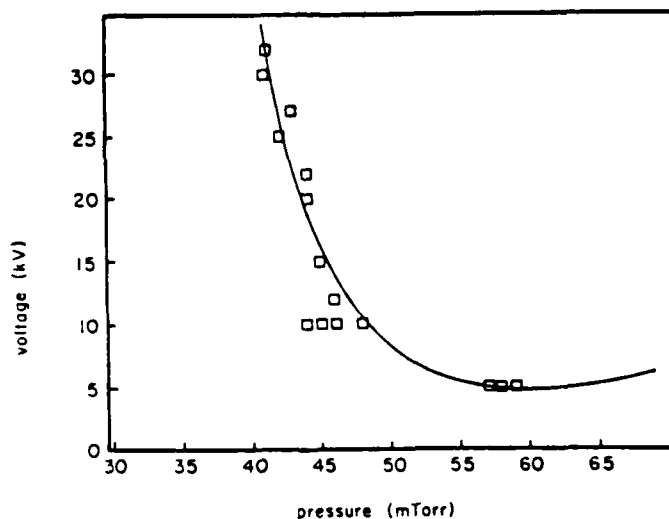
Fig. 2. Measured characteristic breakdown curve.

When the power supply with voltage U_0 is connected via a resistor R, the chamber capacitance C is charged up. At a certain pressure and voltage, U_B, defined by the characteristic breakdown curve (Fig. 2), the voltage breaks down. The charging resistor R virtually decouples the discharge circuit from the power supply. Therefore the low impedance discharge cannot be sustained, and is extinguished. Consequently the chamber capacitance C is changed again until the breakdown voltage U_B is reached and the cycle repeats. Thus a periodic, pulsed discharge is obtained, the time period τ of which is approximately determined by

$$\tau = RC \ell n \frac{U_0}{U_0 - U_B}. \tag{1}$$

By choosing the RC value adequately, periods of typically 0.1 to 1 second can be obtained.

RESULTS

Figure 3 shows a typical set of time correlated electrical signals obtained by Rogowski coils, voltage probe and Faraday cup. The discharge current is measured by the upstream coil and shows a damped oscillating waveform. The voltage drops within 20 ns from 90% to 10% of its maximum. The maximum current corresponds to almost zero voltage indicating an inductance dominated discharge. The downstream coil, as well as the Faraday cup, register only one negative peak at the time of the discharge current maximum.
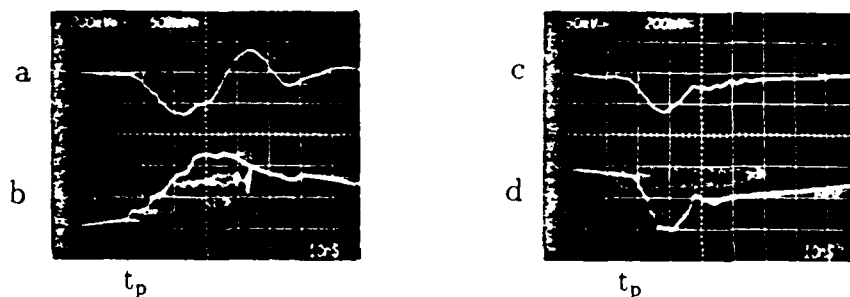
Fig. 3. Typical electrical signals of discharge: time scale 10 ns/div. a) discharge current (upstream coil) 360 A/div; b) voltage signal 10 kV/div; c) injected electron beam current (down-stream coil) 84 A/div; d) Faraday cup signal (15 cm behind anode) 20 A/div.

All signals show that the discharge process occurs in two stages. Up to time t_p the voltage drops slowly, and currents measured by upstream and downstream coils start smoothly. At time t_p the main breakdown occurs. This two-step breakdown is also observed in the waveform of the downstream Faraday cup signal. Of 100 A electron current leaving the anode, as registered by the downstream Rogowski coil, 40 A are measured by the Faraday cup, 15 cm downstream of the anode.

The measured discharge currents with two different external capacitors were fitted to an expression

$$I(t) = I(0)\exp\left(-\frac{R(t - t_0)}{2L}\right)\sin[\omega(t - t_0)], \qquad (2)$$

where $\omega = \left[\frac{1}{LC} - \left(\frac{R}{2L}\right)^2\right]^{1/2}$.

Thus, the least-squares fitted time averaged values for the discharge inductance L and the resistance R were determined, as summarized in Table I.

Table I. The least-squares fitted values of
inductance L and resistance R for different
discharge conditions.

C(pF)	20 kV		25 kV		30 kV	
	R(Ω)	L(nH)	R(Ω)	L(nH)	R(Ω)	L(nH)
420	2.2	56.2	2.1	57.5	1.7	55.3
760	1.7	40.9	1.9	40.2	1.8	44.4

The dependence of discharge current and beam current measured by the upstream and downstream coil as a function of charging voltage for three capacitance values is illustrated in Fig. 4. The current signals show an increase in amplitude with increasing voltage U_B and capacitance. The beam profile and emittance were measured with an external capacitance of 390 pF operated at a breakdown voltage of 24 kV. These results were obtained by averaging more than 20 shots.
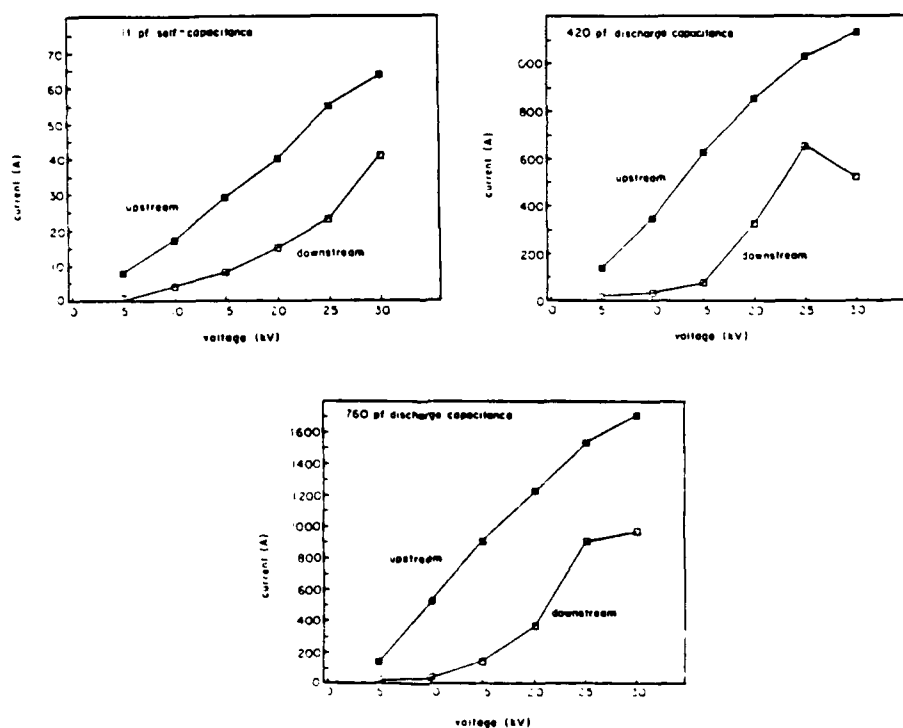
Fig. 4. Upstream and downstream coil current as a function
of charging voltage for discharge capacitance values.

To find the beam profile at different axial distances, the experimental data was fitted to a Gaussian distribution. The values for the root-mean-square (rms) radius b

are shown in Fig. 5. The beam expands from an rms radius of 1.5 mm to 2.5 mm measured at 3 cm and 18 cm, respectively, as it propagates through the low pressure gas.
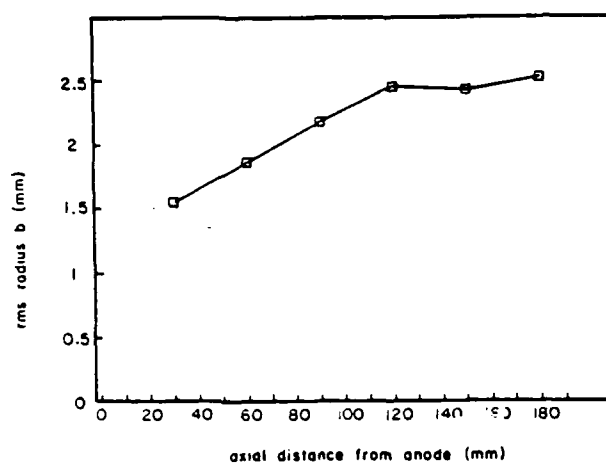

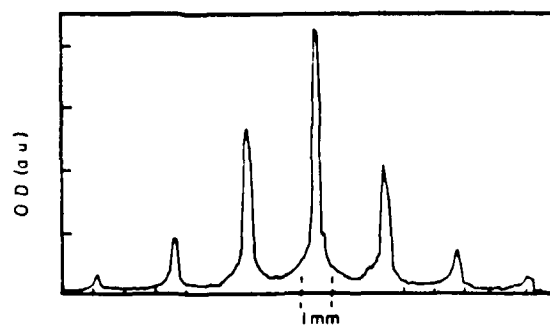Fig. 5. RMS radius b as function of distance from anode.

Fig. 6. Density distribution (optical density O.D.) found behind a 7 slit system at a 9 cm distance from anode.

Figure 6 shows the profile of the scanned beamlet distribution measured at 9 cm downstream of the anode. The rms emittance, ϵ_{rms}, is defined as [17]

$$\epsilon_{rms} = 4\left(<x^2><x'^2> - <xx'>^2\right)^{1/2}.$$

where x' or y' denote the gradients of the particle trajectories, given by $x' = dx/dz$ and $y' = dy/dz$. The brackets $(<>)$ indicate averaged values using the four-dimensional density distribution $\rho_4(x,x',y,y')$ in the four-dimensional "trace space". As the quantities of interest in brackets $(<>)$ are second moments of $x - x'$ coordinates only, the more convenient projected density ρ_2 on two-dimensional trace space can be used, where $\rho_2(x,x') = \rho_4(x,x',y,y')dydy'$.[15] Assuming a Maxwellian transverse velocity distribution, a Gaussian density profile, and an axisymmetric, nonrotational beam, the rms emittance for the electron beam is calculated by numerical integration[15] and found to be

$$\epsilon = 55 \text{ mm} - \text{mrad}$$
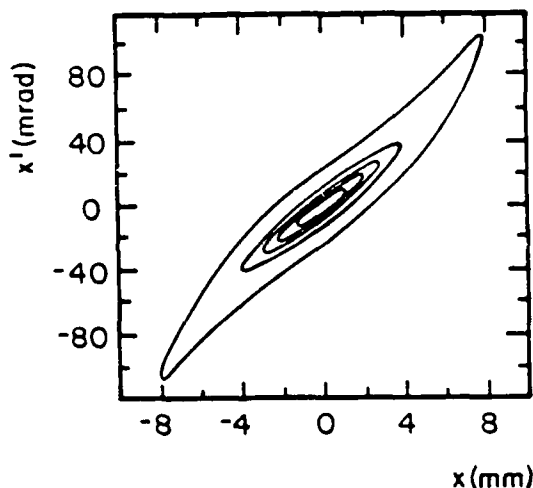
Fig. 7. Two-dimensional emittance contour plot of trace space density $\rho_2(x,x')$. The lines represent projected, constant emittance values, from outside to inside: 99%, 80%, 60%, 40%, 20%.

For an estimated mean beam energy of 20 keV, this leads to a normalized rms emittance ϵ_n of about 15 mm-mrad. The two-dimensional emittance plot is obtained as shown in Fig. 7. Assuming a Maxwellian velocity distribution with an rms velocity $v_{rms} = (kT/m_o)^{1/2}$ in the transverse direction, the normalized emittance at the source can be written as

$$\epsilon_n = 2r_s(kT/m_oc^2)^{1/2} \qquad (1)$$

where r_s is the source radius and T is the temperature. Assuming the same value of ϵ_n = 15 mm-mrad at the source, and the center hole radius 1.6 mm as the source radius, an approximate temperature of 11 eV is obtained.

CONCLUSIONS

The electrical discharge characteristics and the emittance of the ejected electron beam of a pseudospark discharge have been investigated.

The pseudospark breakdown occurs rather reproducibly at the pressure and voltage defined by the characteristic breakdown curve. The discharge takes place in two stages, both of which are accompanied by electron beam emission. The electron energy distribution has still to be determined. After the electron emission occurs, the discharge drops into a low impedance mode whose waveform was modeled, assuming a simple LRC circuit analysis. The electron beam is self-focused as it propagates through low pressure gas. The time integrated emittance was measured at an axial distance of 9 cm. An rms value of about 55 mm-mrad was found. Together with the measured beam current I of 50 A at that distance and the normalized rms emittance $\epsilon_n = 15$ mm-mrad, the normalized brightness B_n is obtained as

$$B_n = \frac{I}{(\epsilon_n)^2} \approx 2 \times 10^{11} \frac{A}{m^2 \cdot rad^2}$$

Thus the pseudospark discharge appears to represent a high brightness electron beam source.

ACKNOWLEDGMENTS

REFERENCES

1. J. Christiansen, Ch. Schultheiss, Z. Phys. A290, 35 (1979).

2. K. Frank, J. Christiansen, Proceedings 13th International Symposium on Discharges and Electrical Insulation in Vacuum, Vol. 2, Paris, June 27-30, 1988 (edited by J.M. Buzzi and A. Septier).

3. R. Reichle, "Untersuchung der räumlichen und zeitlichen Entwicklung des Pseudofunkens mit Methoden optischer Spektroskopie," Dissertation, Universität Erlangen (1987).

4. O. Almen, K. Frank, A. Görtler, C. Kozlik, A. Tinschmann, Proceedings 13th International Symposium on Discharges and Electrical Insulation in Vacuum, Vol. 2, p. 381, Paris, June 27-30, 1988 (edited by J.M. Buzzi and A. Septier).

5. W. Hartmann and M.A. Gundersen, Phys. Rev. Lett. 60, 2371 (1988).

6. D. Bloess, I. Kamber, H. Riege, G. Bittner, V. Brückner, J. Christiansen, K. Frank, W. Hartmann, N. Lieser, Ch. Schultheiss, R. Seeböck, and W. Steudtner, Nucl. Instrum. Methods 205, 173 (1983).

7. G. Mechtersheimer, R. Kohler, F. Lasser, and R. Meyer, J. Phys. E: Sci. Instrum. 19, 466 (1986).

8. G. Kirkman and M.A. Gundersen. Appl. Phys. Lett. 49, 494 (1986).

9. K. Mittag. Proceedings 7th International Conference on High-Power Beams. Vol. 2. p. 1228. Karlsruhe (W. Germany). July 4-8. 1988 (edited by W. Bauer and W. Schmidt).

10. W. Benker. J. Christiansen. K. Frank. H. Gundel. W. Hartmann. A. Niederiohner. T. Redel. M. Stetter. Proceedings 13th International Symposium on Discharges and Electrical Insulation in Vacuum. Vol. 2. Paris. June 27-30. 1988 (edited by J.M. Buzzi and A. Septier).

11. J. Gundlach. "Anregung von Mikrowellen durch den Elektronenstrahl einer Pseudofunkenentladung," master thesis. Physikalisches Institut der Universität Düsseldorf (1986).

12. F. Hoffmann. G. Jung. A. Rogner. C. Schultheiss. A. Kitamura. A. Citron. Proceedings 7th International Conference on High-Power Beams. Vol. 2. p. 1216. Karlsruhe (W.Germany). July 4-8. 1988 (edited by W. Bauer and W. Schmidt).

13. E. Boggasch. V. Brückner. and H. Riege. Proceedings 5th IEEE Pulsed Power Conference. Arlington. VA. 820 (1985).

14. G. Mechtersheimer and R. Kohler. J. Phys.. E20. 270 (1987).

15. M.J. Rhee and R.F. Schneider. Part. Accel. 20, 133 (1986).

16. W.L. McLaughlin. R.M. Uribe. and A. Miller. Radiat. Phys. Chem. 22, 333 (1983).

17. P.M. Lapostolle. IEEE Trans. Nucl. Sci. NS-18, 1101 (1971).

High-brightness pseudospark-produced electron beam

E. Boggasch[a] and M. J. Rhee

Laboratory for Plasma Research, University of Maryland, College Park, Maryland 20742

The first time-integrated root mean square (rms) emittance measurement of a pseudospark-produced electron beam is presented. From a six-gap pseudospark chamber with argon working gas, ~10 Hz repetitive pulsed electron beams of average energy ~20 keV, peak current ~50 A, and pulse duration ~10 ns are extracted into a drift tube. A typical value of measured rms emittance is found to be $\epsilon \approx 55$ mm mrad, yielding a normalized rms emittance of $\epsilon_n \approx 15$ mm mrad. The normalized brightness of the beam is then estimated to be $B_n \approx 4 \times 10^{10}$ A/(m^2 rad^2).

Interest in high-quality, high-current electron beams has been stimulated by stringent source requirements[1] for advanced accelerators such as e^+e^- linear colliders[2] and for high-power free-electron lasers.[3] The pseudospark discharge phenomenon with an interesting charged particle emission characteristic was reported by Christiansen and Schultheiss.[4] The pseudospark discharge may be characterized as a gas discharge between a planar anode and a hollow cathode in the lower-pressure side of the characteristic breakdown curve, which is very similar to the Paschen curve for parallel electrodes. During the breakdown phase, emission of highly pinched electron beams with current densities of up to 10^6 A/cm^2 were observed.[4] These observations suggested to us to investigate the quality and brightness of the beam produced in the pseudospark. In this letter, for the first time, the measurement of time-integrated, root mean square (rms) emittance of the electron beam produced by a pseudospark discharge is described. The normalized beam brightness is evaluated from the measured rms emittance and the average beam energy which is inferred from the voltage waveform.

The experimental setup is schematically shown in Fig. 1. A six-gap pseudospark chamber, which is characteristically similar to the devices reported by other laboratories,[4-8] is used in this work. An easy to change, o-ring sealed, modular device consists of a hollow cathode, five modules of intermediate electrodes, and Plexiglas insulating disks, and an anode. All the electrodes are made of brass and have an outer diameter of 6.35 cm and a center hole of 3.2 mm diameter which provide a channel for the discharge and also for the electron beam passage. The 3.2-mm-thick Plexiglas insulator disks have outer and inner diameters of 7 and 2.54 cm, respectively. An external capacitor of 390 pF is added to the system which provides an adequate amount of stored energy for the electron beam production. A 6.3-cm-diam, 50-cm-long drift chamber is attached to the anode side of the discharge chamber to accommodate diagnostics such as the Faraday cup and the emittance meter. A capacitance-manometer-type vacuum gauge is used to measure the gas fill pressure which is almost statically balanced by a needle valve and a throttle vacuum valve. Two miniature Rogowski

coils of rise time ~0.5 ns are molded into axisymmetric grooves milled into both sides of the anode flange so that the azimuthal component of the magnetic field, which arises from the axisymmetric current, is predominantly supported and other components (noises) are suppressed. A movable Faraday cup consisting of a 100 mΩ current viewing resistor, and a 3-cm-diam graphite charge collector (which is not shown in Fig. 1) connected to the end of a rigid coaxial cable is placed on axis of the downstream drift chamber to measure the electron beam current at various axial positions. This system is also conveniently utilized to support a simple emittance meter which is attached to the end of the cable (see Fig. 1) in lieu of the graphite charge collector; this allows not only emittance measurements at various axial positions, but also simultaneous measurement of the beam current. The discharge chamber voltage is measured by a homemade high-impedance resistive voltage probe of division ratio 1:20 000. The rise time is found to be <0.5 ns, and the RC droop time constant due to the blocking capacitor is ~120 ns. The rms emittance of the electron beam is measured by using a simple slit-hole emittance-meter system.[9] It consists of an array of seven parallel slits of 200 μm width and 2 mm spacing, constructed from a 0.6-mm-thick stainless-steel plate, and a 50-μm thick- (2 mil) radiachromic film,[10] as a beam detector, placed 12 mm downstream of the slit plane. The slits sample the beam at given slit locations producing flat beamlets. The beamlets are then allowed to disperse with their transverse velocity after passing through the slits. The spatial current density profiles of dispersed beamlets at the detector plane are recorded on the radiachromic film, from which the transverse velocity distribution of the beam can be analyzed.

The system is operated typically at 30 kV, with an argon gas fill pressure of 40 mTorr. With a 200 MΩ charging resistor, slow repetition frequencies (1–10 Hz) of the electron beam pulses are easily attained; such frequencies allowed us easier control of the number of beam pulse exposures to the emittance meter. The radiachromic film of the emittance meter, placed 9 cm downstream of the anode plane, is exposed to approximately five consecutive beam pulses to produce an adequate density profile, with the peak value of the optical density well below 0.5. This ensures that the measured optical density distribution is linear to the beam intensity.[10] The beam current measured at this location is 50 A. The beam current density profiles of all beamlets recorded

---

[a] Present address: Max-Planck-Institut für Quantenoptik, D-8046 Garching; and GSI-Darmstadt, D-6100 Darmstadt, Federal Republic of Germany.
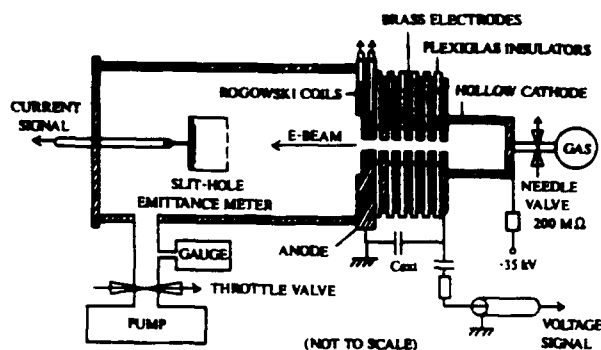
1746   Appl. Phys. Lett. **56** (18), 30 April 1990   0003-6951/90/181746-03$02.00   © 1990 American Institute of Physics   1746

FIG. 1. Schematic representation of the experimental setup.

FIG. 3. Emittance plot in x-x' space. The isodensity contours correspond to 0.1, 20, 40, 60, and 80% of the peak value.

on a radiachromic film are scanned with an optical micro-densitometer; a typical scan is shown in Fig. 2.

The rms emittance[11] or effective emittance[1,12] which has been widely used as a measure of beam quality is defined as

$$\epsilon = 4(\langle x^2 \rangle \langle x'^2 \rangle - \langle xx' \rangle^2)^{1/2}, \qquad (1)$$

where x' is the gradient of the particle trajectory given by $x' = dx/dz = p_x/p_z$, and the angular brackets denote average values over the two-dimensional trace space as $\langle \varphi \rangle = I^{-1} \int \rho \delta(x,x') dx\, dx'$, where ρ is the projected current density in two-dimensional trace space, and the total current is given by $I = \int \rho\, dx\, dx'$.

It is very reasonable to assume that, as in Ref. 9, the beam produced in this experiment is axisymmetric and of Maxwellian transverse velocity distribution. Such an assumption allows us to use the simple slit-hole-type emittance meter mentioned above, whose results can be easily analyzed.[9] We find empirical functions $\alpha(r)$, $\beta(r)$, and $\sigma(r)$ as functions of radial position r from the density profile shown in Fig. 2, where $\alpha(r)$ is the mean diverging angle, $\beta(r)$ represents the peak values, and $\sigma(r)$ is the rms width of the individual distributions. Numerical integrations are then performed using the empirical functions α, β, and σ to find $\rho(x,x')$ and the moments $\langle x^2 \rangle$, $\langle x'^2 \rangle$, and $\langle xx' \rangle$ (see Ref. 9 for details). Several isodensity contours of the resultant $\rho(x,x')$ are constructed in x-x' space (known as an emittance plot) as shown in Fig. 3. The measured rms emittance, given by Eq. (1) with the obtained moments, is found to be $\epsilon \approx 55$ mm mrad. The error analysis on the emittance is
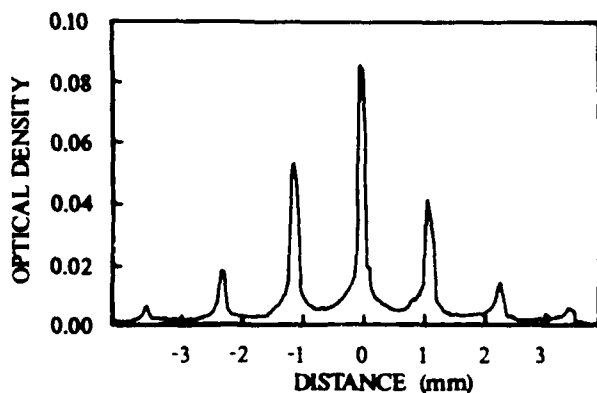

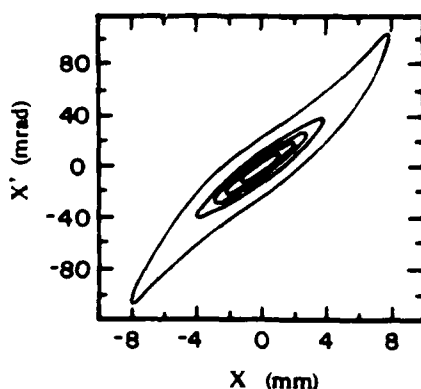FIG. 2. Typical optical density profile of radiachromic film produced by electron beamlets in the emittance meter.

somewhat difficult; nevertheless, a rough estimate is made and found to be $\pm 15\%$. It is interesting to note that the emittance plot in Fig. 3 shows a slightly inverse S-shaped contour; this is indicative of the existence of nonlinear focusing (defocusing) in the beam possibly due to the space-charge field of substantial strength. The normalized rms emittance defined as $\epsilon_n = \beta\gamma\epsilon$, where $\beta = v/c$ and $\gamma = (1 - \beta^2)^{-1/2}$, is invariant[13,14] in the presence of axial acceleration, and is conveniently used for comparing beam qualities at different energies. With an average beam energy of 20 keV inferred from the voltage probe signal, the normalized emittance is estimated to be $\epsilon_n \approx 15$ mm mrad. Another useful invariant of the beam associated with the emittance is the brightness,[15] for which unfortunately, no universally agreed exact definition exists. We use here a typical expression[13] of *normalized rms brightness* $B_n = 2I/(\pi^2\epsilon_n^2)$. With a measured current of 50 A, we have obtained the brightness $B_n \approx 4 \times 10^{10}$ A/(m^2 rad^2), which is substantially higher than that of other high brightness sources.[3,16] It should be noted here that the electron beam pulses are very reproducible, and the results in this work are all time integrated over a few shots of 10 ns pulses.

In conclusion, we have measured, for the first time, the emittance of a pseudospark-produced electron beam. A six-gap pseudospark chamber with argon gas is operated at 30 kV and produced a repetitive pulse train of electron beams. Typically, a beam of average energy 20 keV, peak current ~ 50 A, and pulse duration ~ 10 ns full width at half maximum is extracted from the chamber. The rms emittance is evaluated by using the slit-hole method. The typical value of the rms emittance is found to be $\epsilon \approx 55$ mm mrad, yielding a normalized emittance of $\epsilon_n \sim 15$ mm mrad. These values are time integrated over a few shots of entire pulses and represent the upper limit. The normalized rms brightness of the beam is then estimated as $B_n = 2I/(\pi^2\epsilon_n^2) \approx 4 \times 10^{10}$ A/(m^2 rad^2), which is substantially higher than that of existing high-brightness electron beam sources.

[1]M. Reiser, in *Proceedings of the 1989 Workshop on Advanced Accelerator Concepts*, AIP Conference Proceedings 193, edited by C. Joshi (AIP, New York, 1989), p. 311.

[2]R. Stiening, in *Proceedings of the 1987 IEEE Particle Accelerator Conference*, edited by E. R. Lindstrom and L. S. Taylor (IEEE, Piscataway, NJ, 1987), p. 1.

[3]C. W. Roberson and P. Sprangle, Phys. Fluids B 1, 3 (1989).

[4]J. Christiansen and C. Schultheiss, Z. Phys. A 290, 35 (1979).

[5]D. Bloess, I. Kamber, H. Riege, G. Bittner, V. Brückner, J. Christiansen, K. Frank, W. Hartmann, and N. Lieser, Ch. Schultheiss, R. Seeböck, and W. Steudtner, Nucl. Instrum. Methods 205, 173 (1983).

[6]P. Choi, H. H. Chuaqui, M. Favre, and E. S. Wyndham, IEEE Trans. Plasma Sci. PS-15, 428 (1987).

[7]C. Schultheiss, Nucl. Instrum. Methods A 254, 398 (1987).

[8]H. Gundel, H. Riege, J. Handerek, and K. Zioutas, Appl. Phys. Lett. 54, 2071 (1989).

[9]M. J. Rhee and R. F. Schneider, Particle Accelerators 20, 133 (1986).

[10]W. L. McLaughlin, R. M. Uribe, and A. Miller, Radiat. Phys. Chem. 22, 333 (1983).

[11]P. M. Lapostolle, IEEE Trans. Nucl. Sci. NS-18, 1101 (1971).

[12]J. D. Lawson, *The Physics of Charged-Particle Beams*, 2nd ed. (Clarendon, Oxford, 1988), p. 192.

[13]J. D. Lawson, *The Physics of Charged-Particle Beams*, 2nd ed. (Clarendon, Oxford, 1988), p. 158.

[14]M. J. Rhee, Phys. Fluids 29, 3495 (1986).

[15]A. van Steenbergen, IEEE Trans. Nucl. Sci. NS-12, 746 (1965).

[16]D. A. Kirkpatrick, R. E. Shefer, and G. Bekefi, J. Appl. Phys. 57, 5011 (1985), and references therein.

Appl. Phys. Lett., Vol. 56, No. 18, 30 April 1990

E. Boggasch and M. J. Rhee   1748

Anode foil changer for high-current relativistic electron beam diode systems

T. A. Fine and M. J. Rhee

Electrical Engineering Department and Laboratory for Plasma Research. University of Maryland. College Park. Maryland 20742

An anode foil changer for pulsed, high-current, relativistic electron beam diode systems is described. This device allows multiple shots to be taken with a foil-anode diode system while maintaining a continuous vacuum. Shot-to-shot reproducibility is greatly improved, while at the same time a significant time savings is realized. Also, various diagnostics and options are added to the basic design which further increase its utility and flexibility.

Diode systems used in pulsed intense relativistic electron beam experiments have many uses in current research,[1] and their design may be considered to be centered on two basic experimental configurations[2]: those using foil anodes,[3] and foilless diodes.[4,5] These systems have various design needs which must be addressed. Foil anodes in present use make for a small anode-cathode gap, providing the low impedance necessary for the production of high-current beams. When the beam is being injected into a gas-filled chamber, some type of barrier must be used to separate the vacuum diode area from the gas-filled area. Diagnostics are often included to measure various beam and diode characteristics, such as diode current or injected beam current. All such factors must be considered, while at the same time designing the general experimental setup to be easy and efficient to use.

Unfortunately, there are a great many problems that generally go along with such foil diode systems. Diode systems using a foil anode require that the diode be taken apart—and the vacuum broken—after each shot to replace the anode foil. Not only is this a time-consuming process, but shot-to-shot reproducibility is reduced as the experimental setup is tampered with after each firing; vacuum and maintenance problems may also be aggravated in this process.

A device has been built which satisfies all these requirements, while at the same time eliminating many of the problems. This device—which we call a foil changer—greatly enhances experimental reproducibility, efficiency, and flexibility. Figure 1 shows the experimental diode setup with the foil changer in place. This foil changer allows multiple shots to be taken with a foil-anode diode system while maintaining a continuous vacuum and without disturbing experimental conditions; with our present version, over 20 shots can be taken before foil replacement is necessary, which is usually enough to complete one experimental series. This gives the obvious benefit of speeding up research and data aquisition. Just as important, the integrity of the experimental setup is assured for the entire series of shots, and reproducibility from shot to shot is improved.

Figure 2 shows a diagram of the foil changer device. This particular version was designed to be compatible with a 15-cm vacuum system and drift chamber. The outer diameter is 16.8 cm. Vacuum flanges compatible with Dependex vacuum equipment are built in on both sides of the foil changer. A 4.4-cm diam hole is bored through the center of the device over which the anode foil will be placed; the beam will be injected through the foil and center hole into the drift region beyond. Two 7-cm × 2.2-cm × 1.75-cm windows are milled into the body of the foil changer on either side of the beam hole. In these cavities a strip of anode foil material is rolled up and placed inside; the strip of foil is wrapped around rods which extend to knobs outside the device via
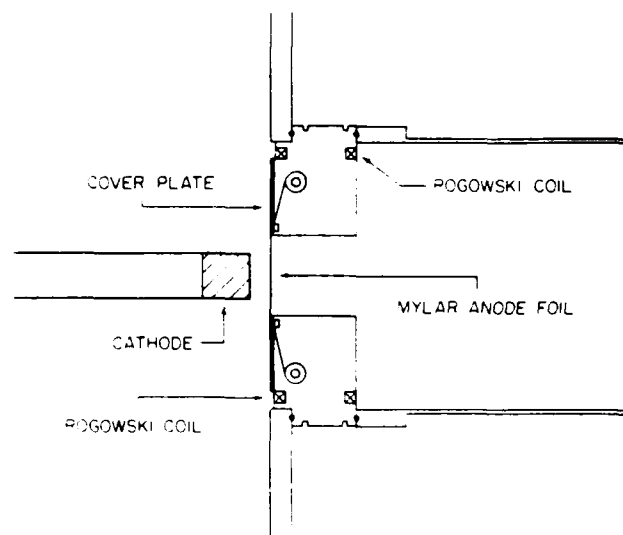

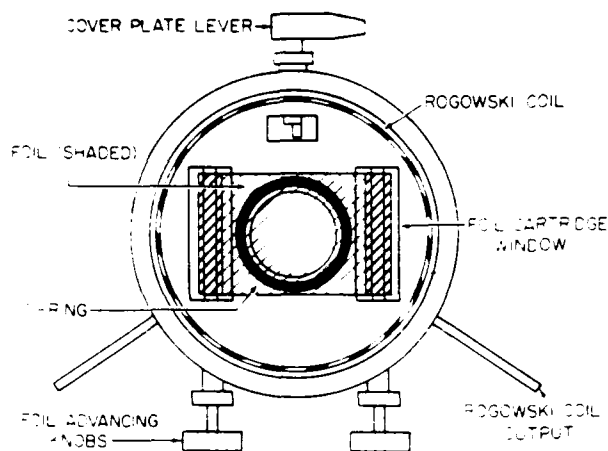FIG. 1. Schematic of diode system with foil changer in place.

FIG. 2. Diagram of foil changer.

vacuum feedthroughs. This foil strip can then be advanced across the anode plane from one window to the other after each shot, maintaining vacuum conditions at all times. Figure 3 shows a photograph of the foil changer, along with a sample strip of anode foil showing the series of holes created by the beam during an experimental series.

The anode foil itself is used as a barrier between the diode and drift regions. Such a barrier is needed in experiments in which the drift region is filled with a gas, while the diode area remains evacuated, for example beam injection into a neutral gas. To achieve this barrier, an O ring is placed in a groove underneath the foil strip and around the center hole. A cover plate with a central window of the same diameter as that of the center hole is then placed over the foil on the diode side. This cover plate may be opened and closed by means of a cam, which extends to a lever outside the body of the foil changer via a vacuum feedthrough. When the cover plate is "closed," the foil is firmly pressed against the O ring,

creating a hermetic barrier between the diode and drift regions. When "opened" after firing a shot, the pressure against the foil is released, and the foil strip can be advanced for the next shot. This can all be done while maintaining a continuous vacuum. It should be mentioned that this cover plate serves another useful purpose: it protects the body of the foil changer from beam damage. While the cover plate is a separate unit and is easily replaced, the foil changer itself is not.

The basic concept of this foil changer has been given added utility and flexibility by the addition of various design options. For diagnostics, two Rogowski coils have been built in to the device. The coil on the upstream (diode) side measures the diode current, while the coil on the downstream (drift region) side measures net injected beam current. These coils were designed using a toroidal core of plexiglas wrapped with 19 turns of 3.2-mm wide copper tape; the core diameter is 13.6 cm and the cross-sectional area is 2 mm × 2 mm. These coils were permanently set into a groove cut just inside the vacuum flanges by means of transparent epoxy. The leads of the Rogowski coils were coupled to semirigid coaxial cables outside the device through small holes bored into the rim of the foil changer. The diode and injected current signals can then be monitored by oscilloscopes. These Rogowski coils are of low inductance, with a rise time of $L/R < 1$ ns.

An added feature built into our foil changer is the addition of a puff-valve feedthrough entrance leading to just downstream of the anode foil plane. This allows the foil changer and its associated diagnostics to be used for foilless diode configurations also, using a puff valve in place of a foil anode. When needed, the puff valve is simply fit into the vacuum feedthrough entrance and the foil strip is removed; when not in use, the entrance is simply blocked off.

Taken together, the capabilities of this device make for much more reliable and efficient experimental work. Because an entire experimental series can be performed in vacuum, without taking the diode apart after each shot, reproducibility is greatly enhanced. The monolithic and compact size make for easy experimental assembly, while consequently minimizing mechanical problems. The many built-in features make it simple to change experimental conditions, i.e., foil anode, puff-gas system, etc. Finally, because it is no longer necessary to take apart the diode after each shot to replace the foil, a significant amount of time is saved; instead of taking perhaps one series of ten shots in a day, one can take several series of twenty shots or more.

FIG. 3. Photograph of foil changer and sample strip of anode foil after an experimental series of beam shots (the cover plate is not shown).

A. C. Kolb, IEEE Trans. Nucl. Sci. NS-22, 956 (1975).
R. B. Miller, An Introduction to the Physics of intense Charged Particle Beams (Plenum, New York, 1982), pp. 31-76.
C. B. Wheeler, J. Phys. D 7, 267 (1974).
M. Friedman and M. Ury, Rev. Sci. Instrum. 41, 1334 (1970).
J. A. Nation and M. Read, Appl. Phys. Lett. 23, 426 (1973).

Invariance properties of the root-mean-square emittance in a linear system

M. J. Rhee

Electrical Engineering Department and Laboratory for Plasma and Fusion Energy Studies.
University of Maryland, College Park, Maryland 20742

It is shown that for a beam of arbitrary distribution function, the root-mean-square emittance is invariant under any linear transformation if the determinant of transfer matrix is unity. The in...riance condition is generalized by defining a normalized root-mean-square emittance to include the case with a nonunity determinant which is associated with an axial acceleration.

Since the root-mean-square (rms) emittance was introduced by Lapostolle[1] and Sacherer,[2] it has been widely used as a figure of merit for beam quality. Lawson et al.[3] have established theoretical grounds for use of the rms emittance in which the entropy of the beam is closely connected with its rms emittance. The nonlinear effect in the system increases the entropy and thus the rms emittance. In addition, a number of authors have shown[4-6] that the rms emittance is an invariant of the motion if the focusing effect is linear. The need, for reference purposes, for a general description of invariance properties became apparent.

In this Brief Communication, we present a general treatment of invariance properties of the rms emittance in any linear system. In the linear system, the evolution of the distribution function is governed by a linear transformation of the individual particle point. We show that only if the determinant of the transfer matrix of the linear transformation is unity, the rms emittance is invariant regardless of the form of the distribution function. This invariance condition is extended by defining a normalized rms emittance to include the nonunity determinant case, which is associated with an axial acceleration.

The x-plane rms emittance is defined[1,2] as

$$\bar{\epsilon}_x = k(\langle x^2 \rangle \langle x'^2 \rangle - \langle xx' \rangle^2)^{1/2}, \tag{1}$$

where x' is the gradient of particle trajectory given by $x' = dx/dz = p_x/p_z$, and the angular brackets ($\langle\ \rangle$) denote an average value over the two-dimensional trace space[6] as $\langle g \rangle = \int g\rho(x,x')dx\, dx'$. The validity of the emittance calculation with $\rho(x,x')$ in two-dimensional trace space is not simple in general and is discussed in Refs. 4 and 5. For the purpose of the present work, we assume a simple beam with a single degree of freedom, such as a strip beam or equivalent, in which the x and y motions are decoupled so that the beam can be represented by density distribution in two-dimensional x-p_x phase space. Furthermore, we assume that the instantaneous axial velocity at a given point z is constant over the beam cross section. The $\rho(x,x')$ may be considered as the instantaneous density distribution function of particle tracks left on the x-x' trace plane, at a given value of z, by a short slice of beam as it passes by. The scale factor k, commonly taken as 4, will be omitted throughout. It should be pointed out that the rms emittance is not a mathematical rms value of emittance as opposed to what the term as well as the symbols commonly used seem to imply.

We consider a linear transformation[7] in two-dimensional trace space,

$$\begin{bmatrix} x \\ x' \end{bmatrix} = \begin{bmatrix} a & b \\ c & d \end{bmatrix} \begin{bmatrix} x_1 \\ x'_1 \end{bmatrix}, \tag{2}$$

by which values of x and x' at point z are related to those at z_1. The elements of the transfer matrices $a, b, c,$ and d may be functions of z but independent of $x_1, x'_1, x,$ and x'. This linear transformation has properties that straight lines transform into straight lines and ellipses transform into ellipses. Particle tracks within a square-shaped differential area $dx_1\, dx'_1$ at z_1 transform into a parallelogram $dx\, dx'$ at z as depicted in Fig. 1. Since the particles are conserved in this linear transformation, the same number of tracks must be found within $dx_1\, dx'_1$ and $dx\, dx'$. This is expressed by the relation

$$\rho_1(x_1,x'_1)dx_1\, dx'_1 = \rho(x,x')dx\, dx'$$
$$= \rho(ax_1 + bx'_1, cx_1 + dx'_1)|J|dx_1\, dx'_1, \tag{3}$$

where $J = \partial(x,x')/\partial(x_1,x'_1) = ad - bc$, a Jacobian, which in this case is equal to the determinant of transfer matrix $|A|$.

Now we consider a transformation of the rms emittance value from z_1 to z. Each term in Eq. (1) is calculated in terms of variables x_1 and x'_1 with the aid of an integral theorem
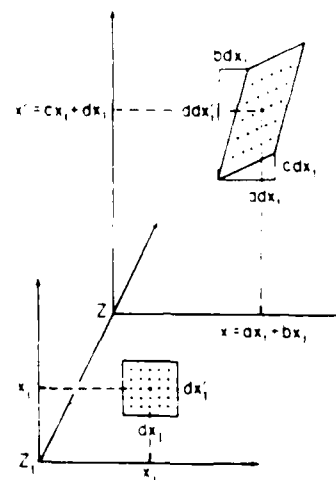
$$\int F(x,y)dx\, dy = \int F[x(u,v),y(u,v)]|J|du\, dv,$$

FIG. 1. The linear transformation is schematically illustrated. The transfer matrix elements used in this example are $a = 1, b = 0.5, c = 0.5,$ and $d = 2$ and the corresponding determinant and Jacobian are $|A| = J = 1.75$.

as

$$\langle x^2 \rangle = \int x^2 \rho(x,x')dx\,dx'$$

$$= \int (ax_1 + bx_1')^2$$

$$\times \rho(ax_1 + bx_1', cx_1 + dx_1')|J|dx_1\,dx_1' . \quad (4)$$

From the particle conservation, Eq. (3), ρ in Eq. (4) is replaced by $\rho_1(x_1,x_1')$, yielding

$$\langle x^2 \rangle = \int (ax_1 + bx_1')^2 \rho_1(x_1,x_1')dx_1\,dx_1'$$

$$= a^2\langle x_1^2 \rangle + 2ab\langle x_1 x_1' \rangle + b^2\langle x'^2 \rangle . \quad (5)$$

Similarly,

$$\langle x'^2 \rangle = c^2\langle x_1^2 \rangle + 2cd\langle x_1 x_1' \rangle + d^2\langle x'^2 \rangle , \quad (6)$$

and

$$\langle xx' \rangle = ac\langle x_1^2 \rangle + (ad + bc)\langle x_1 x_1' \rangle + bd\langle x'^2 \rangle . \quad (7)$$

Combining Eqs. (5)–(7), we find the following simple expression for the transformation of rms emittance:

$$\langle x^2 \rangle\langle x'^2 \rangle - \langle xx' \rangle^2$$

$$= (ad - bc)^2(\langle x_1^2 \rangle\langle x_1'^2 \rangle - \langle x_1 x_1' \rangle^2) , \quad (8)$$

$$\bar{\epsilon}_x = A\,\bar{\epsilon}_x .$$

Equation (8) clearly shows that the rms emittance is invariant under any linear transformation if and only if the transfer matrix determinant is unity. Typical examples of such a transformation are force-free drift and thin lens systems. It is noted that this result, Eq. (8), is a consequence of the linear transformation imposed but with an arbitrary distribution function $\rho(x,x')$. It should not be construed that Liouville's theorem is not applicable to this case. The trace-space area is $(m_0\beta\gamma c)^{-1}$ times that in phase space, since $x' = p_x/(m_0\beta\gamma c)$. Therefore, the transformed area in $x - x'$ space is subject to change if the factor $\beta\gamma$ changes in the transformation.

It is of interest that the determinant A can be related to the paraxial ray equation.[4] The paraxial equation may be reduced into a general form

$$x'' + g(z)x' + h(z)x = 0 . \quad (9)$$

Since Eq. (9) is linear and second order, it therefore has a general solution which is any combination of two independent solutions. Supposing that Eq. (9) governs the motion of particles in a linear system described by the transformation [Eq. (2)], the transformation $x = ax_1 + bx_1'$ may be considered to be a general solution to Eq. (9) where x_1 and x_1' are initial conditions at z_1. The terms $a(z)$ and $b(z)$, being independent solutions, must satisfy Eq. (9) separately,

$$a'' + ga' + ha = 0 , \quad b'' + gb' + hb = 0 . \quad (10)$$

These simultaneous equations are solved for $g(z)$, yielding

$$g(z) = -W'/W = -A'/A , \quad (11)$$

where W is the Wronskian, and the prime denotes the derivative with respect to z. If x and x' in Eq. (2) are continuous, then $a' = c$ and $b' = d$, and thus the Wronskian is equal to

the determinant of the transfer matrix: $W = |A|$. Hence, one finds the determinant in terms of $g(z)$ as

$$A = \exp\left(\int_{z_1}^{z} g(z)dz\right) . \quad (12)$$

In the absence of a magnetic field, the term $g(z)$, the coefficient of x' of paraxial equations, is reduced[4] to

$$g(z) = \gamma'/(\beta^2\gamma) , \quad (13)$$

which is associated with an axial acceleration. Equation (13) is then substituted into Eq. (12), and one finds that

$$A = \beta_1\gamma_1/(\beta\gamma) . \quad (14)$$

It is evident that after substitution of Eq. (14) into Eq. (8), a new emittance defined as

$$\bar{\epsilon}_{xn} = \beta\gamma\bar{\epsilon}_x = \beta_1\gamma_1\bar{\epsilon}_x . \quad (15)$$

is invariant. This may be referred to as *normalized rms emittance* resemblant to the normalized emittance. It is clear from Eq. (14) that since the Jacobian is equal to $|A|$, the transformed rms emittance, which has a dimension of area, is inversely proportional to $\beta\gamma$. This is caused by the fact that,[4,5] as in the case with normalized emittance, if an area in x-p_x phase space is invariant by Liouville's theorem and p_x is changed by the presence of axial acceleration during the transformation, the area in x-x' trace space is reduced by the factor $(\beta\gamma)^{-1}$. For the same reason as the normalized emittance,[4] use of the normalized rms emittance may be convenient when considering beams in which there is acceleration, and also when comparing beams at different energies and with different particles.

In conclusion, it is shown that the rms emittance is, in general, an invariant quantity under any linear transformation if the determinant of transfer matrix is unity. By defining normalized rms emittance, the invariance condition is generalized to include the case with a nonunity transfer matrix determinant when axial acceleration exists.

[1] P. M. Lapostolle, IEEE Trans. Nucl. Sci. NS-18, 1101 (1971).
[2] F. J. Sacherer, IEEE Trans. Nucl. Sci. NS-18, 1105 (1971).
[3] J. D. Lawson, P. M. Lapostolle, and R. L. Gluckstern, Part. Accel. 5, 61 (1973).
[4] J. D. Lawson, The Physics of Charged Particle Beams (Clarendon, Oxford, 1977).
[5] C. Lejeune and J. Aubert, in Applied Charged Particle Optics, Part A, edited by A. Septier (Academic, New York, 1980), pp. 159–259.
[6] M. J. Rhee and R. F. Schneider, Part. Accel. 20, 133 (1986).
[7] A. J. Lichtenberg, Phase-Space Dynamics of Particles (Wiley, New York, 1969).

BRIEF COMMUNICATIONS

Root-mean-square emittance increase in a nonlinear lens

M. J. Rhee

Department of Electrical Engineering and Laboratory for Plasma Research, University of Maryland, College Park, Maryland 20742

An exact derivation of the root-mean-square emittance increase when a beam of arbitrary distribution passes through a nonlinear lens system is presented. It is found that the emittance increase depends on the spherical aberration coefficient of the lens and characteristics of the beam distribution.

The root-mean-square (rms) emittance growth associated with the nonlinearity of a focusing lens system has been an important issue,[1] as the spherical aberration is inherently associated with the focusing lenses used in accelerating and transport channels. It is well known that the nonlinearity of an array of lenses gives rise to the filamentation of emittance, resulting in an increase of the rms emittance while the phase-space area occupied by the beam remains unchanged. Given the nonlinear nature of the phenomenon, the studies on this subject have often been undertaken by heuristic computational simulations.[2] We would like to present here a general treatment of rms emittance increase when a beam of arbitrary distribution passes through an ideal thin lens with spherical aberration.

The rms emittance is defined[3,4] as

$$\epsilon = k(\langle x^2\rangle\langle x'^2\rangle - \langle xx'\rangle^2)^{1/2}, \tag{1}$$

where k (the scale factor commonly taken as 4) will be omitted throughout, x' is the gradient of the particle trajectory given by $x' = dx/dz = p_x/p_z$, and the angular bracket denotes an average value over the two-dimensional trace space as

$$\langle g(x,x')\rangle = N^{-1}\int_{-\infty}^{\infty} g(x,x')\rho(x,x')dx\,dx', \tag{2}$$

where $\rho(x,x') = \int_{-\infty}^{\infty}\rho_4(x,y,x',y')dy\,dy'$ is the projection of the four-dimensional distribution $\rho_4(x,y,x',y')$ onto two-dimensional trace space and $N = \int_{-\infty}^{\infty}\rho\,dx\,dx'$.

We consider a beam of arbitrary distribution $\rho_1(x_1,x_1')$, which is passed through a one-dimensional thin lens with spherical aberration. Then, the beam is transformed as

$$x = x_1, \tag{3}$$

$$x' = x_1' + ax_1 + bx_1^3, \tag{4}$$

where coefficients a and b may be expressed in terms of the focal length f and the spherical aberration coefficient C_s of the lens: $a = 1/f$ and $b = C_s/f^4$. It should be noted[5] here that there is a coupling between x and y motion in the axisymmetric lens with the spherical aberration; thus the transforma-

tion in such a lens cannot be described by Eq. (4).

As shown in Ref. 6, if the Jacobian of the transformation is unity, the averaged value given by Eq. (2) in the transformed space coordinates can be conveniently found in terms of the x_1-x_1' coordinates and distribution $\rho_1(x_1,x_1')$ as

$$\langle g(x,x')\rangle = N^{-1}\int_{-\infty}^{\infty} g(x,x')\rho(x,x')dx\,dx'$$

$$= N^{-1}\int_{-\infty}^{\infty} g(x_1,x_1' + ax_1 + bx_1^3)$$

$$\times\rho_1(x_1,x_1')J\,dx_1\,dx_1', \tag{5}$$

where $J = \partial(x,x')/\partial(x_1,x_1') = 1$ for the transformation given by Eq. (2). Thus Eq. (5) can be reduced to a simpler form as

$$\langle g(x,x')\rangle = \langle g(x_1, x_1' + ax_1 + bx_1^3)\rangle_1, \tag{6}$$

where the subscript 1 after the angular bracket [which denotes integration over the x_1-x_1' space with distribution $\rho_1(x_1,x_1')$] will be omitted throughout. Thus the moments necessary for the present analysis can be readily found in an algebraic form as

$$\langle x^m x'^n\rangle = \langle x_1^m(x_1' + ax_1 + bx_1^3)^n\rangle. \tag{7}$$

Now we evaluate the moments in Eq. (1) in terms of x_1-x_1' coordinates with the aid of Eq. (7) as

$$\langle x^2\rangle = \langle x_1^2\rangle, \tag{8}$$

$$\langle x'^2\rangle = \langle(x_1' + ax_1 + bx_1^3)^2\rangle$$

$$= \langle x_1'^2\rangle + a^2\langle x_1^2\rangle + b^2\langle x_1^6\rangle + 2a\langle x_1x_1'\rangle$$

$$+ 2b\langle x_1^3x_1'\rangle + 2ab\langle x_1^4\rangle, \tag{9}$$

$$\langle xx'\rangle = \langle x_1(x_1' + ax_1 + bx_1^3)\rangle$$

$$= \langle x_1x_1'\rangle + a\langle x_1^2\rangle + b\langle x_1^4\rangle. \tag{10}$$

Substituting Eqs. (8)–(10) in Eq. (1), we find the transformed rms emittance as

$$\epsilon^2 = \langle x_1^2 \rangle \langle x_1'^2 \rangle - \langle x_1 x_1' \rangle^2$$
$$+ b^2 (\langle x_1^2 \rangle \langle x_1^6 \rangle - \langle x_1^4 \rangle^2)$$
$$+ 2b(\langle x_1^2 \rangle \langle x_1^3 x_1' \rangle - \langle x_1 x_1' \rangle \langle x_1^4 \rangle)$$
$$\equiv \epsilon_1^2 + b^2 \alpha_1 + 2b\beta_1. \tag{11}$$

Equation (11) shows that the square of emittance is increased by $b^2 \alpha_1 + 2b\beta_1$, where α_1 and β_1 are measures of some characteristic quantities of beam distribution before the transformation. It is noted that the emittance increase in Eq. (11) is dependent on the nonlinear coefficient b in Eq. (2), but independent of the linear focusing coefficient a as expected, since the rms emittance is invariant[6] under any linear transformation.

It is very interesting to show how the quantities α and β transform as the beam passes through the nonlinear lens. Again using Eq. (3), the moments and product moments composing the quantities α and β are readily found, yielding

$$\alpha = \langle x^2 \rangle \langle x^6 \rangle - \langle x^4 \rangle^2$$
$$= \langle x_1^2 \rangle \langle x_1^6 \rangle - \langle x_1^4 \rangle^2$$
$$= \alpha_1 \tag{12}$$

and

$$\beta = \langle x^2 \rangle \langle x^3 x' \rangle - \langle xx' \rangle \langle x^4 \rangle$$
$$= \langle x_1^2 \rangle \langle x_1^3 x_1' \rangle - \langle x_1 x_1' \rangle \langle x_1^4 \rangle$$
$$+ b(\langle x_1^2 \rangle \langle x_1^6 \rangle - \langle x_1^4 \rangle^2)$$
$$= \beta_1 + b\alpha_1. \tag{13}$$

Note that the quantity α remains unchanged, but the change in β is simply the nonlinear coefficient b times α_1. This simple transformation of α and β through the nonlinear lens may be very useful in the evaluation of rms emittance growth in successive transformations such as in periodic focusing channels.

As an example, a beam of distribution

$$\rho(x,x') = \exp[-x^2/(2\delta^2) - x'^2/(2\sigma^2)] \tag{14}$$

is passed through a thin nonlinear lens that transforms the beam distribution according to Eqs. (3) and (4). It is then straightforward to find the rms emittance ϵ and the quantities α and β before the transformation by direct integration [Eq. (2)]:

$$\epsilon_1^2 = \Sigma^2 \sigma^2,$$
$$\alpha_1 = 6\delta^8, \tag{15}$$
$$\beta_1 = 0.$$

After the transformation the same quantities are found by using Eq. (6) as

$$\epsilon^2 = \epsilon_1^2 + b^2 \alpha_1 + 2b\beta_1 = \delta^2 \sigma^2 + 6b^2 \delta^8,$$
$$\alpha = 6\delta^8, \tag{16}$$
$$\beta = b\alpha_1 = 6b\delta^8.$$

The same results of this particular case may also be obtained by direct integration using Eq. (2), which is lengthy but straightforward. The emittance diagrams in x-x' space of the
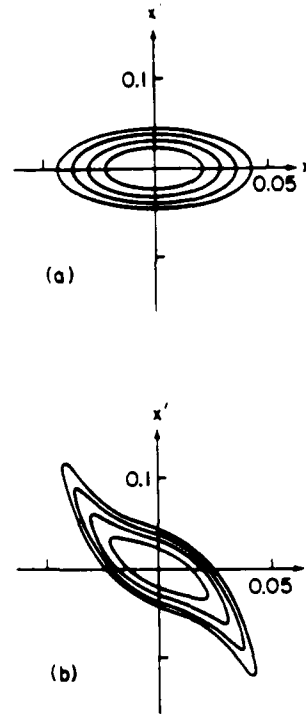

FIG. 1. Emittance diagrams in x-x' trace space for (a) a distribution $\rho(x_1,x_1') = \exp[-x_1^2/(2\delta^2) - x_1'^2/(2\sigma^2)]$, where $\delta = 0.01$ m and $\sigma = 0.01$ rad. (b) The same distribution transformed by $x = x_1$, $x' = x_1' + ax_1 + bx_1^3$, where $a = -$. rad/m and $b = -1000$ rad/m^3.

beam before and after the transformation in this example are illustrated in Fig. 1.

In conclusion, we have presented an exact derivation of the rms emittance increase of an arbitrary beam in a one-dimensional nonlinear lens system. The quantities α and β associated with the beam distribution transform linearly through the nonlinear lens system. This fact may be useful in determining the emittance growth in a transport or accelerating system in which successive focusing lenses are employed. The results may be useful for a variety of one-dimensional electrostatic and magnetic lens systems. It may also be possible to extend the use of these results in order to estimate the emittance increase in other types of systems such as those using quadrupole and axisymmetric lenses.

[1] J. D. Lawson, *The Physics of Charged Particle Beams* (Clarendon, Oxford, 1989), 2nd ed., pp. 186-195.
[2] P. W. Hawkes, *Applied Charged Particle Optics*, edited by A. Septier (Academic, New York, 1980), pp. 45-157.
[3] P. M. Lapostolle, IEEE Trans. Nucl. Sci. NS-18, 1101 (1971).
[4] F. J. Sacherer, IEEE Trans. Nucl. Sci. NS-18, 1105 (1971).
[5] J. D. Lawson (private communication); the axisymmetric lens may be described by a transformation $x = x_1$, and $x' = x_1 + ax_1 + b(x_1^3 + x_1 y_1^2)$, in which x' is coupled with y_1.
[6] M. J. Rhee, Phys. Fluids 29, 3495 (1986).